

**ULTRA-WIDEBAND ANTENNAS FOR
MEDICAL IMAGING AND
COMMUNICATION APPLICATIONS**

ULTRA-WIDEBAND ANTENNAS FOR MEDICAL IMAGING AND COMMUNICATION APPLICATIONS

By

Hamed Mazhab Jafari

Bachelor of Applied Science

McMaster University

Hamilton, Ontario, Canada

April 2004

A THESIS

SUBMITTED TO THE SCHOOL OF GRADUATE

STUDIES IN PARTIAL FULFILLMENT OF THE

REQUIREMENTS FOR THE DEGREE OF

MASTER'S OF APPLIED SCIENCE

McMaster University

Hamilton, Ontario, Canada

© Copyright by Hamed Mazhab Jafari, August 2006

MASTER OF APPLIED SCIENCE (2006)

McMaster University

(Electrical and Computer Engineering)

Hamilton, Ontario

TITLE: ULTRA-WIDEBAND ANTENNAS FOR MEDICAL IMAGING AND
COMMUNICATION APPLICATIONS

AUTHOR: Hamed Mazhab Jafari, B.A.Sc. (McMaster University)

SUPERVISORS: Prof. M. Jamal Deen and Prof. Steve Hranilovic

NUMBER OF PAGES: 155

Abstract

The allocation of 7.5 GHz of bandwidth by the Federal Communication Commission (FCC) for ultra-wideband (UWB) applications has provided an exciting and a challenging opportunity to design short range wireless communication and microwave imaging systems. To fully realize the potential of the UWB, communication and microwave imaging systems are required to operate over the entire UWB frequency band. The combination of the wide bandwidth requirement and the target application of the UWB systems have led to a surge of interest in designing of novel integrated circuits and antennas for the UWB applications. In any wireless communication and microwave imaging system, the antenna has a fundamental effect on the overall performance of the system, and as a result, it has attracted considerable research interest.

This thesis focuses on the design of UWB antennas that are suitable for UWB cancer detection and wireless communication systems. Two planar antennas, one a printed monopole antenna, and the other, a printed slot antenna fed with a coplanar waveguide, are presented in this work. First, the antennas have been designed to operate in air, making them suitable for the UWB wireless short range communication applications. Measurement and simulation results indicate that both antennas achieve input impedance matching in a bandwidth of more than 7.5 GHz. The effect on the input matching of the antennas due to the variation in their geometrical parameters has been studied and both antennas have been fully characterized in air. Next, the two antennas have been redesigned to operate in a coupling medium for medical imaging applications. Both antennas achieve return loss of less than -10 dB over the entire UWB spectrum. Also, the antennas have been fully characterized while operating in the coupling medium and in proximity to a human body model. Finally, a two-element antenna array, based on the printed monopole antenna and the printed slot antenna, in co- and cross-polarized array formation, has been designed. The tumor detection capabilities of all antenna arrays for different scenarios have been studied through electromagnetic simulation and measurements.

Acknowledgements

Before acknowledging and thanking all the people I worked with, I would like to thank God for all the strength he gave me throughout my two years as a Master's student to complete my work successfully.

Next I would like to express my sincere thanks and deep appreciation to my supervisor, Dr. Jamal Deen, for his thoughtful and constant guidance throughout the course of this thesis, and for giving me the opportunities for the academic advancements I have made. His regular encouragement, support and technical insights were invaluable to me throughout the course of this work. Further, it enabled me to perform to the best of my abilities and he provided me with opportunities and exposure that I would otherwise never have had. I am thankful to work with such an outstanding researcher and mentor.

I would also like to express my deep appreciation and sincere thanks to my co-supervisor Dr. Steve Hranilovic for guidance, help and encouragement. All he has ever taught me has proven indispensable and his advice will surely outlive this phase of my life.

I also thank the following members of Professor Deen's Microelectronics Research Laboratory – Wei Liu, Farseem Mohammady, Waleed Shinwari, Moussa Kfourri, Mohammad Abdulaziz Kotb Naser, Fernando Campos, Juan-Carlos Ranuarez, Sasan Naseh, Rizwan Murji, Nabeel Jafferli, Wai Ngan, Ahmed Fakh, Ehab El-Badry, - for their support, comments and assistance during the course of this research. I especially thank Munir M. EL-Desouki, who was always helpful to me. I would also like to thank Dr. Ognian Marinov for his helpful advice and support during my graduate and undergraduate studies. I also sincerely thank Dr. Natalia Nikolova for all her advice and guidance throughout my work.

Finally, I would like to express my deepest acknowledgements and appreciation to my dear family, for being a constant source of support not only during the writing of this thesis but throughout my life.

Table of Contents

Abstract	IV
Acknowledgements.....	V
Table of Contents.....	VI
List of Tables	VIII
List of Figures.....	IX
Chapter 1: INTRODUCTION.....	15
1.1 Ultra-wideband Overview.....	15
1.2 Ultra-wideband Technology for Communication Applications	17
1.3 Ultra-wideband Technology for Imaging Applications.....	22
1.4 Motivation for Antenna Design	24
1.5 Contributions.....	26
1.6 Thesis Organization	26
Chapter 2: ANTENNA BACKGROUND	27
2.1 Fundamental Antenna Parameters	27
2.1.1 Impedance bandwidth	27
2.1.2 Radiation pattern.....	28
2.1.3 Half-power beamwidth	31
2.1.4 Directivity	32
2.1.5 Efficiency	32
2.1.6 Gain.....	33
2.1.7 Polarization	34
2.1.8 Fidelity	35
2.2 UWB Antenna Requirements	36
2.3 Literature Review.....	38
2.3.1 Microstrip-fed “dark eyes” antenna.....	38
2.3.2 Ultra-low reverberation antenna	41
2.3.3 Resistively loaded Wu-King monopole antenna.....	43
2.3.4 Dielectric-filled slotline bowtie antenna.....	44
2.3.5 Ultra-wideband ridged pyramidal horn antenna	46

2.4	Summary	47
Chapter 3:	CHOICE OF COUPLING MEDIUM AND DESIGN OF COPLNAR- WAVEGUIDES.....	48
3.1	Choice of the Coupling Medium.....	48
3.1.1	Study of reflection mechanism	49
3.2	Design of the Coplanar Waveguide (CPW).....	54
3.2.1	Calculation of CPW geometrical parameters.....	54
3.3	Summary	59
Chapter 4:	TAPERED SQUARE PRINTED MONOPOLE ANTENNA	61
4.1	Wideband Planar Monopole Antennas	62
4.2	The Design of the Tapered Square Printed Monopole Antenna	65
4.3	TSPM Antenna Optimization and Measurement Results	67
4.4	TSPM Antenna Radiation Characteristic.....	72
4.5	TSPM Antenna Surface Current Distribution.....	75
4.6	TSPM Antenna For Near Field Imaging.....	80
4.6.1	UWB antenna array for biomedical imaging	92
4.6.1.1	TSPM Antenna in co-polarized formation.....	93
4.6.1.2	TSPM Antenna in cross-polarized formation	100
4.6.1.3	Measured Tumor Detection Capabilities (co-polarized array)	105
4.7	Summary	107
Chapter 5:	WIDEBAND SLOT ANTENNA.....	109
5.1	Wideband Slot Antenna Design and Optimization	110
5.2	CTS Antenna's Radiation Characteristic	115
5.3	CTS Antenna Surface Current Distribution.....	117
5.4	CTS Antenna with a Frequency Notched Characteristic	121
5.5	Wideband Slot Antenna for Biomedical Imaging.....	127
5.5.1	CTS Antenna in Co-polarized and Cross-polarized Formation.....	135
5.6	Summary	144
Chapter 6:	CONCLUSIONS	145
6.1	Summary	145
6.2	Future Work.....	147
References	150

List of Tables

Table 1.1 Narrowband Communication System	18
Table 1.2 Survival Rates of The Different Stages of Breast Cancer.....	23
Table 2.1 UWB Antenna's Requirements.....	38
Table 3.1 Physial Parameters of CPW	58
Table 4.1 Monopole Antenna's Bandwidth	64
Table 4.2 Antenna's Parameters for Figure 4.7	69
Table 4.3 Optimized TSPM Antenna's Parameters	71
Table 4.4 Optimized TSPM Antenna's Parameters for UWB Imaging Application.....	82
Table 4.5 SMA Geometrical Parameters	83
Table 4.6 Debye's Model Parameters	88
Table 4.7 TSPM Antenna's Maximum SAR	88
Table 5.1 CTS Antenna's Parameters	114
Table 5.2 CTS Antenna's Parameters for UWB Imaging	128
Table 5.3 CTS Antenna Maximum SAR	131
Table 6.1 Comparison of Antenna for Breast Cancer Detection.....	148

List of Figures

Figure 1.1. (a) Time domain presentation of a narrow band and a UWB signal, (b) frequency domain representation of a narrowband and UWB signal, and (c) UWB emission level [1].....	17
Figure 1.2. UWB applications in wireless area networking [4].....	19
Figure 1.3. (a) Narrowband transceiver, (b) UWB transceiver [6].....	20
Figure 1.4. (a) Multiple paths due to the multiple reflection of the transmitted signal, (b) delay in the received signal due to the multipath effect [13].....	21
Figure 1.5. Cancer death rates from 1930 to 2001 [7].	22
Figure 1.6. Dielectric properties of malignant and normal breast tissue [41].....	24
Figure 2.1. Three-dimensional radiation pattern of $\lambda/2$ dipole.	30
Figure 2.2. Two-dimensional radiation pattern in (a) elevation plane and (b) azimuth plane, of $\lambda/2$ dipole.	30
Figure 2.3. Half-power beamwidth.....	32
Figure 2.4. (a) Linear polarization, (b) circular polarization, and (c) elliptical polarization.	35
Figure 2.5. Geometry of dark eye antenna [14].....	39
Figure 2.6. Simulated antenna input impedance for different sheet resistances [14].	39
Figure 2.7. Simulated antenna near field (E-plane) [14].	40
Figure 2.8. Simulated antenna near field (H-plane) [14].	40
Figure 2.9. Geometry of co-polarized bowtie antenna. [17].....	41
Figure 2.10. Cross-polarized bowtie antenna [17].....	42
Figure 2.11, Measured input matching of cross-polarized bowtie antenna [18].	43
Figure 2.12, Photograph of Wu-King monopole antenna [19].	43
Figure 2.13. Measured VSWR [19].	44
Figure 2.14. (a) Slot line bowtie antenna, and (b) dielectric slot line bowtie antenna [19].	44
Figure 2.15. Measured and simulated return loss of dielectric field bowtie antenna [19].	45
Figure 2.16. Photograph of the ridged pyramidal horn antenna [20].....	46
Figure 2.17. Geometry of the ridged pyramidal horn antenna [20].	47

Figure 2.18. Simulated and measured VSWR of the antenna [20].	47
Figure 3.1. Reflection mechanism through a three-layer body model.	50
Figure 3.2. Real and imaginary permittivity of human fat and pork fat [61-65].	53
Figure 3.3. (a) Magnitude of the total E-field in the coupling medium (human fat) and breast, and (b) magnitude of the total E-field in the coupling medium (pork fat) and breast.	53
Figure 3.4. Schematic diagram of a coplanar waveguide.	54
Figure 3.5. Multilayer structure used to calculate the characteristic impedance of the CPW in the coupling medium.	55
Figure 3.6. Configuration used to calculate (a) C0, (b) C1, (c) C2 and (d) C3.	56
Figure 3.7. (a) Real part of the characteristic impedance, (b) imaginary part of characteristic impedance and (c) losses in the CPW.	59
Figure 4.1. (a) Conventional patch antenna (b) monopole antenna with vertical ground plane and (c) planar monopole antenna [14].	62
Figure 4.2. (a) Square planar monopole antenna (SPMA), (b) disc planar monopole antenna (DPMA), (c) triangular planar monopole antenna (TPMA) and (d) hexagonal planar monopole antenna (HPMA).	64
Figure 4.3. Schematic of the tapered square printed monopole (TSPM) antenna.	65
Figure 4.4. Simulated return loss for different feed gap size G, ($W_1 = 50$ mm, $W_2 = 25$ mm, $L_1 = 50$ mm, $L_2 = 25$ mm).	67
Figure 4.5. Simulated return loss for different antenna width, ($W_1 = 50$ mm, $L_1 = 50$ mm, $L_2 = 25$ mm, $G = 0.6$ mm).	68
Figure 4.6 Simulated returns loss for different antenna lengths ($W_1 = 50$ mm, $W_2 = 29$ mm, $L_1 = 50$ mm and $G = 0.6$ mm).	69
Figure 4.7. Antenna schematic, with the feed point shifted from the center.	70
Figure 4.8. Reflection coefficient of the antenna for different feed locations.	70
Figure 4.9. Measured and simulated reflection coefficient of the antenna.	71
Figure 4.10. Measured antenna gain at the boresight.	72
Figure 4.11. Radiation efficiency versus frequency.	73
Figure 4.12 Radiation pattern of the antenna at (a) 2 GHz, (b) 3 GHz, (c) 4 GHz, and (d) 5 GHz.	73

Figure 4.13. Radiation pattern of the antenna at (a) 6 GHz, (b) 7 GHz (c) 8 GHz, (d) 9 GHz, and (e) 10 GHz.....	74
Figure 4.14. Surface current distribution at (a) 2 GHz, (b) 3 GHz, and (c) 4 GHz.	76
Figure 4.15. Surface current distribution at (a) 5 GHz, (b) 6 GHz, and (c) 7 GHz.	77
Figure 4.16. Surface current distribution at (a) 8 GHz, (b) 9 GHz, and (c) 10 GHz.	78
Figure 4.17. (a) Geometry of the antenna with removed metallization, and (b) simulated reflection coefficient of the antenna with full metallization (TSPM) and partial metallization (TSPM-Cut).	79
Figure 4.18. Simulated S21 of the CPW in pork fat and Hi-K cement.....	81
Figure 4.19. Geometry of the SMA connector feeding the antenna: (a) SMA cross section in the z-axis, (b) SMA cross section in the y-axis	82
Figure 4.20. (a) Schematic of antenna measurement setup, and (b) the measurement environment.	84
Figure 4.21. Measured and simulated return loss of the antenna in the coupling medium.	85
Figure 4.22. Coupling (S21) between the antennas in the coupling medium.	85
Figure 4.23. Antenna's reflection coefficient as function of distance to the skin interface.	86
Figure 4.24. (a) Fidelity simulation setup, (b) Fidelity versus distance.	87
Figure 4.25. SAR distribution (a) 3.5 GHz @ skin interface, (b) 3.5 GHz @ breast interface, (c) 5.5 GHz @ skin interface, (d) 5.5 GHz @ breast interface, (e) 8.5 GHz @ skin interface, and (f) 8.5 GHz @ breast interface.	89
Figure 4.26. Antenna's near E-field in proximity of a multilayer body model on the x-axis at (a) $z = 2$ cm, (b) $z = 3$ cm, (c) $z = 4$ cm, and on the y-axis at (d) $z = 2$ cm, (e) $z = 3$ cm, and (f) $z = 4$ cm (refer to Figure 4.3 for the coordinate system).	91
Figure 4.27. Geometry of co-polarized array element.....	93
Figure 4.28. Measured reflection coefficient of the co-polarized array element.....	95
Figure 4.29. Measured coupling between two antennas of the co-polarized array element.	95
Figure 4.30. Measured phase of the co-polarized array element.	96

Figure 4.31. Measured group delay between two antennas of the co-polarized array element.....	96
Figure 4.32. Schematic of the XFDTD simulation environment.....	98
Figure 4.33, (a) Input signal to the transmitted antenna. (b) Received pulse at the receiver antenna, for one layer simulation scenario. (c) Tumor response from one layer simulation scenario. (d) Received pulse at the receiver antenna, for two layer simulation scenario. (e) received signal due to the mussel layer. (f) Tumor response from one layer simulation scenario.....	99
Figure 4.34. Geometry of co-polarized array element.....	100
Figure 4.35. Measured reflection coefficient of the cross-polarized array element.	101
Figure 4.36. Measured coupling between the cross-polarized array elements.	101
Figure 4.37. Measured phase of the cross-polarized array element.....	102
Figure 4.38. Measured group delay between two antennas of the cross-polarized array element.....	102
Figure 4.39. (a) Input signal to the transmitted antenna. (b) Received pulse at the receiver antenna, for one layer simulation scenario. (c) Tumor response from one layer simulation scenario. (d) Received pulse at the receiver antenna, for two layer simulation scenario. (e) received signal due to the mussel layer. (f) Tumor response from one layer simulation scenario.....	104
Figure 4.40. Voltage waveform used to excite the transmitter antenna.....	106
Figure 4.41. Measurement setup.....	106
Figure 4.42. (a) received pulse from tumor at depth of 0, 1 and 2 cm, (b) received pulse from tumor at depth of 3, 4 cm (c) received pulse from tumor at depth of 5, 6 cm, (d) normalized received energy from tumor at different depth.....	107
Figure 5.1. Schematic of the CPW-fed tapered slot (CTS) antenna.	110
Figure 5.2. Simulated return loss for different radius of the tuning stub.....	112
Figure 5.3. Simulated return loss for different values of D_x	113
Figure 5.4. Simulated return loss for different values of C_x	113
Figure 5.5. Simulated and measured VSWR of CTS Antenna.	114
Figure 5.6 CTS antenna's radiation pattern at (a) 2.5 GHz, (b) 3 GHz, (c) 4 GHz, and (d) 5GHz.....	115

Figure 5.7 CTS antenna's radiation pattern at (a) 6 GHz, (b) 7 GHz, (c) 8 GHz, (d) 9 GHz, and (d) 10 GHz.....	116
Figure 5.8. Sinusoidal current distribution at the first resonant frequency.....	117
Figure 5.9. Surface current distribution at (a) 2.5 GHz, (b) 3 GHz, and (c) 4 GHz.	118
Figure 5.10. Surface current distribution at (a) 5 GHz, (b) 6 GHz, and (c) 7 GHz.	119
Figure 5.11. Surface current distribution at (a) 8 GHz, (b) 9 GHz, and (c) 10 GHz.	120
Figure 5.12. Geometry of the slot antenna with band notch characteristic.....	122
Figure 5.13. Surface current distribution on the tuning stub (a) antenna with the V-shape slot, and (b) antenna without the V-shape slot.....	123
Figure 5.14. Measured and simulated antenna VSWR.	123
Figure 5.15. Antenna radiation pattern (a) without the V-shaped slot. and (b) with the V-shaped slot.....	124
Figure 5.16. Geometry of the monopole antenna with band notch characteristic.	124
Figure 5.17. Simulated antenna VSWR with and without the V-shaped slot.....	125
Figure 5.18. Antenna's radiation pattern (a) without the V-shaped slot, and (b) with the V-shaped slot.	126
Figure 5.19. Measured and simulated return loss of the antenna in the coupling medium.	129
Figure 5.20. Antenna's reflection coefficient as function of distance to the skin interface.	130
Figure 5.21. Fidelity of the slot antenna vs. distance.....	130
Figure 5.22 SAR distribution(a) 3.5 GHz @ skin interface, (b) 3.5 GHz @ breast interface,(c) 5.5 GHz @ skin interface, (d) 5.5 GHz @ breast interface, (e) 8.5 GHz @ skin interface, and (f) 8.5 GHz @ breast interface.	132
Figure 5.23 Antenna near E-field in proximity of a multilayer body model on the x-axis at (a) $z = 2$ cm, (b) $z = 3$ cm, and (c) $z = 4$ cm; and on the y-axis at (d) $z = 2$ cm, (e) $z = 3$ cm, and (f) $z = 4$ cm (refer to Figure 5.1 for the coordinate system).	134
Figure 5.24. Geometry of the co-polarized CTS antenna array.....	135
Figure 5.25. Geometry of the cross-polarized CTS antenna array.	135
Figure 5.26. Measured antenna return loss and the coupling between the array elements in the co-polarized and cross-polarized formation.....	136

Figure 5.27. Measured phase of the co-polarized array element.	137
Figure 5.28. Measured phase of the cross-polarized array element.....	137
Figure 5.29. (a) Input signal to the transmitter’s antenna, (b) received pulse at the receiver’s antenna, for one layer simulation scenario, (c) tumor response from one layer simulation scenario, (d) received pulse at the receiver antenna, for two layer simulation scenario, (e) received signal due to the muscle layer, and (f) tumor response from one layer simulation scenario.	139
Figure 5.30. (a) Input signal to the transmitter’s antenna, (b) received pulse at the receiver’s antenna, for one layer simulation scenario, (c) tumor response from one layer simulation scenario, (d) received pulse at the receiver antenna, for two layer simulation scenario, (e) received signal due to the muscle layer, and (f) tumor response from one layer simulation scenario.	140
Figure 5.31. (a) Co-polarized tumor response at depth of 0, 1 and 2 cm; (b) co-polarized tumor response at depth of 3 and 4 cm; (c) co-polarized tumor response at depth of 5 and 6 cm; (d) cross-polarized tumor response at depth of 0, 1 and 2 cm; (e) cross-polarized tumor response at depth of 3 and 4 cm, and (f) cross-polarized tumor response at depth of 5 and 6 cm.....	142
Figure 5.32. Received energy by the co-polarized and cross-polarized array elements for different tumor depth.	143
Figure 5.33. (a) Co-polarized tumor and muscle response, and (b) cross-polarized tumor and muscle response.	143

Chapter 1: INTRODUCTION

The continued demand for high speed communication and high resolution imaging systems have stimulated a surge of interest in the design of wideband communication and imaging systems. In the domain of microwave imaging, wide bandwidth provides the opportunity to achieve high resolution and high penetration using the higher and lower frequency components of the transmitted signal. Also, in the area of wireless communication, wideband systems are enabling seamless connection of consumer electronic products, and as a result, wideband systems are becoming predominant and the need for bandwidth is increasing exponentially.

The introduction of ultra-wideband technology has provided an exciting and challenging opportunity to develop and design new wideband wireless communication and microwave imaging systems. Since an antenna has a fundamental effect on the performance of a communication or an imaging system, it has attracted much research interest in recent years. The fact that the antenna design is a fundamental challenge in the wideband system has lead to a surge of interest in the wideband antenna design.

This thesis focuses on the design of antennas to meet the requirements of ultra-wideband imaging and communication systems. Before discussing specifically the scope of this thesis, a brief introduction is presented and the concept of the ultra-wideband system and its application in communication and imaging systems is described.

1.1 Ultra-wideband Overview

The Federal Communications Commission (FCC) has defined an ultra-wideband (UWB) signal as a signal with a -10 dB fractional bandwidth (B_f) greater than 20%, or a signal with at least 500 MHz bandwidth, regardless of the fractional bandwidth. The fractional bandwidth is defined as follows [1]:

$$B_f = 2 \times \frac{(f_h - f_l)}{(f_h + f_l)}, \quad (1-1)$$

where f_h and f_l are the higher and lower -10 dB points in the spectrum.

The FCC has recently allocated 7.5 GHz of bandwidth (3.1-10.6 GHz) for UWB applications. Contrary to the narrowband systems such as IEEE 802.11a, IEEE 802.11b and Bluetooth systems that transmit continuous sinusoidal signals in the time domain, UWB systems transmit and receive pulses with very narrow duration in the time domain, for example 200 ps [4]. Figure 1.1(a) and (b) illustrate the time domain signal that is transmitted by a narrow band system, and the corresponding frequency domain representation. As shown, in the frequency domain, the continuous time signal corresponds to a bandwidth that is concentrated around the carrier frequency. On the other hand, the short time duration pulse transmitted by a UWB system corresponds to a very wide frequency band with low spectral density, as shown in Figure 1.1(b).

Figure 1.1(c) depicts the UWB spectral mask specified by the FCC. There are two main bands that are defined for UWB systems. The first band is from DC to approximately 1 GHz and the second band is from 3.1 GHz to 10.6 GHz. A maximum spectral density of -41.3 dBm/MHz is allowed for the UWB system in both operating bands [2]. The low level spectral density is set to ensure that the UWB systems does not interfere with the narrowband systems such as 802.11.a that are operating within the UWB frequency range.

If the 7.5 GHz bandwidth is completely exploited, it corresponds to only 0.5 mW of total transmitted power, which is a small fraction of the power that is transmitted by a conventional narrow band system such as IEEE 802.11. This low level of transmitted power effectively limits the UWB system to the indoor short range communication applications or short range imaging applications [3].

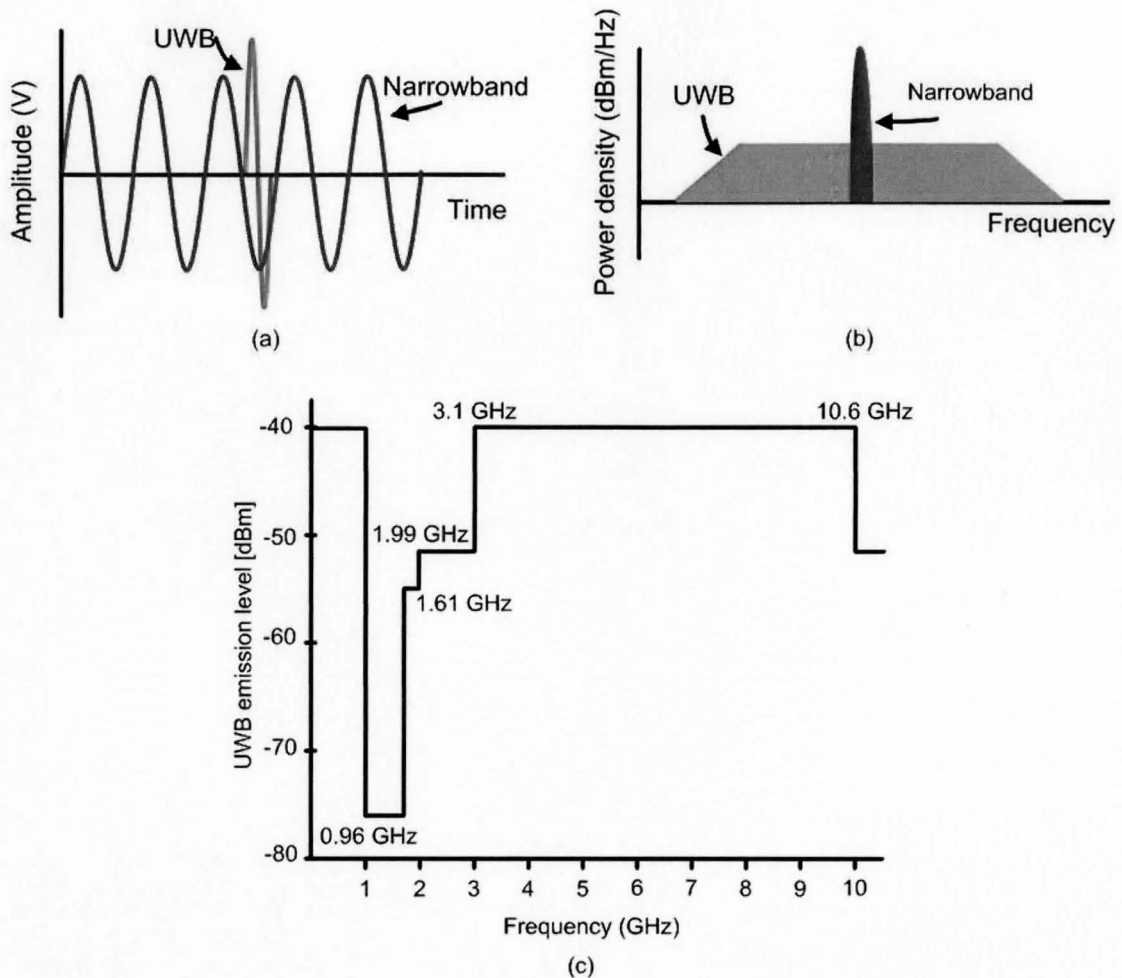


Figure 1.1. (a) Time domain presentation of a narrow band and a UWB signal, (b) frequency domain representation of a narrowband and UWB signal, and (c) UWB emission level [1].

1.2 UWB Technology for Communication Applications

The rapid advances in consumer electronic systems over the past few years demand continued improvement in wireless communication systems which must provide higher data transfer rates, while reducing the overall cost and power consumption level of the wireless systems. To meet the requirements of wireless personal area networking systems such as IEEE 802.15.3a, wireless communication systems are required to achieve data transfer rate in excess of 100 Mbits/second in short range applications (10-20 m). Today, wireless technologies such as IEEE 802.11a, IEEE 802.11g and Bluetooth, are

inherently incapable of achieving such high data rates due to their limited bandwidth as shown in Table 1.1[3].

Table 1.1
NARROWBAND COMMUNICATION SYSTEMS

Technology	Data Rate (Mbits/second)	Range (meters)	Frequency bandwidth (MHz)
IEEE 802.11a	54	50	20
IEEE 802.11b	11	100	25
IEEE 802.11g	54	100	25
Bluetooth	1-2	10	1
Zigbee	0.25	50	80

Due to the short pulses and the wide frequency bandwidth, UWB technology promises to revolutionize wireless personal area networking (WPAN). UWB technology can offer systems with low cost, low complexity and low power consumption, while providing data rates up to 500 Mbits/second for short range wireless applications. The high data transfer rate and low system cost enable UWB systems to create home media networking such as the one shown in Figure 1.2 by taking over tasks such as distributing high definition TV signals from one receiver to multiple TVs, downloading images from a digital camera to a computer, connecting printers to computers and potentially replacing any cable connection between consumer products [4].

Due to the wideband nature of the transmitted pulses, UWB systems have a number of advantages that make them a good candidate for short-range, high-speed communication applications. At the same time, the short duration of UWB pulses and the wide-frequency bandwidth of the UWB system pose some design challenges. The advantages and the challenges facing UWB system design are summarized below.

- **Low complexity and low cost transceiver**

In a conventional narrow band system, it is necessary to up-convert the baseband signal into a higher frequency band that is suitable for wireless transmission and

reception. The up-conversion is done in a mixing stage in which an RF-carrier signal is injected into the base band signal, shown in Figure 1.3(a). This will result into translation of the baseband signal into the higher frequency band (RF), thus enabling the baseband signal to be transmitted and received efficiently using an antenna. Contrary to the narrowband system, UWB pulses, as shown in Figure 1.1(b), occupy frequency ranges which are used by the RF carriers. Therefore, the baseband data is suitable for RF propagation, and communication schemes such as pulse position modulation and on-off keying, and it can be directly sent to the antenna without any frequency up-conversion. The elimination of the up-conversion on the system level corresponds to the replacement of the RF-mixers and the LO-oscillators by a Gaussian pulse generator (PG), as shown in Figure 1.3 (b). The pulse generator is built using digital components, and this in turn simplifies the transceiver design in UWB system. On the other hand, the wideband nature of the UWB pulses poses great challenges to the design of RF integrated circuits and the antennas, where the narrowband circuit and antenna design techniques are not adequate. As a result, new design methodologies are required to meet the bandwidth requirements of the UWB system [5].



Figure 1.2. UWB applications in wireless area networking [4].

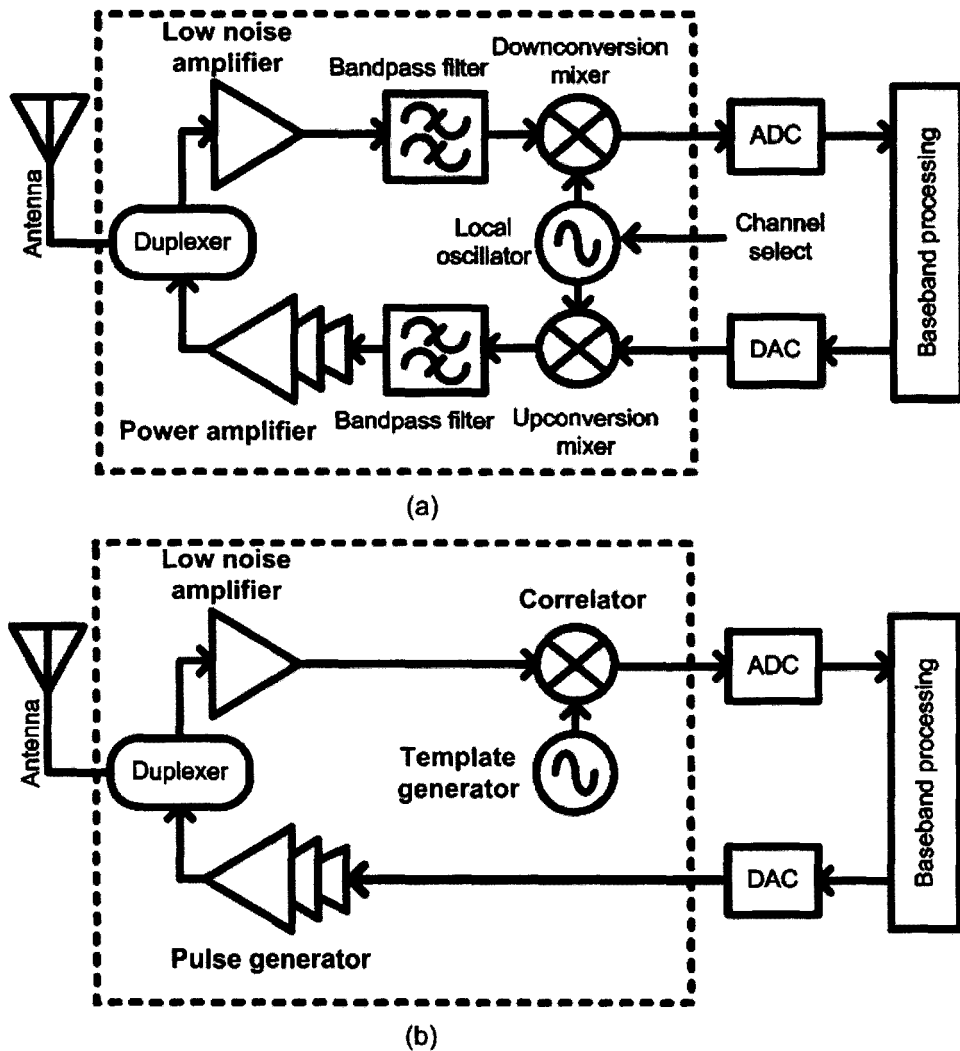


Figure 1.3. (a) Narrowband transceiver, (b) UWB transceiver [6].

- **Low spectral density**

The UWB transmitted signals appear noise-like due to their low power spectrum density and pseudo-random characteristic over the wide bandwidth. Due to these low power spectrum characteristics, UWB systems do not cause significant interference with narrowband systems. Therefore, it is possible to operate the UWB system in proximity of existing narrowband systems or even integrate the UWB systems with the current narrowband systems. The drawback of the noise-like characteristics of the UWB signal is that it limits the UWB communication systems to short-range indoor application. Also, it increases the complexity of the circuit design for UWB communication and imaging

application due to the low level of transmitted and received power and the wide bandwidth requirement.

- **Immune to severe multi-path**

Multi-path interference in communication systems occurs when two coherent signals arrive at the receiver antenna from two different paths, as shown in Figure 1.4. If the two signals are out of phase, then the combination of the two signals will result in a reduction or increase in the amplitude of the overall received signal, which is also known as Rayleigh fading. Also, the multi-path effect can result in inter-symbol interference due to the fact that the same transmitted signal can arrive at the receiver at different times. In UWB systems, because of the short time domain duration of the UWB pulses and discontinuous nature of the pulse transmission, the chances of having two pulses overlapping and completely canceling each other out are very low. Also, the pulses that arrive later on will not cause inter-symbol interference due to the fact that they are outside of the receiving windows, as shown in Figure 1.4. Therefore, a UWB system can achieve very high multi-path resolution which makes it immune to severe multi-path effects.

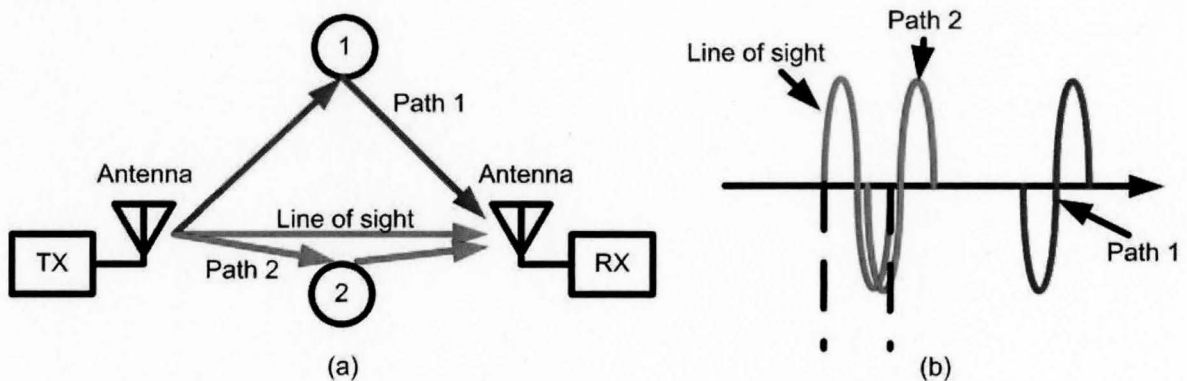


Figure 1.4. (a) Multiple paths due to the multiple reflection of the transmitted signal, (b) delay in the received signal due to the multipath effect [13].

- **Interference with narrowband systems**

As shown in Figure 1.1(c), UWB systems occupy a very wide frequency band from 3.1 to 10.6 GHz. There are a number of narrow band systems such as IEEE 802.11.a,b,g, GPS and UMTS operating in this frequency band. These narrowband systems can potentially interfere with the UWB system given that the power transmitted

from these narrowband systems is an order of magnitude higher than the one being transmitted from the UWB system. As a result, filtering of these frequency bands should be considered in the UWB antenna design, to ensure stable operation of the UWB system in the proximity of narrowband systems.

1.3 UWB Technology for Imaging Applications

Breast cancer is one of the major causes of fatality in women. Figure 1.5 shows the death rate due to different types of cancer in the female population in the United State from 1930 to 2005. In the female population, breast cancer is the second deadliest type of cancer and in 2005, 212,920 new cases of breast cancer were diagnosed and 40,970 women have died from breast cancer [7].

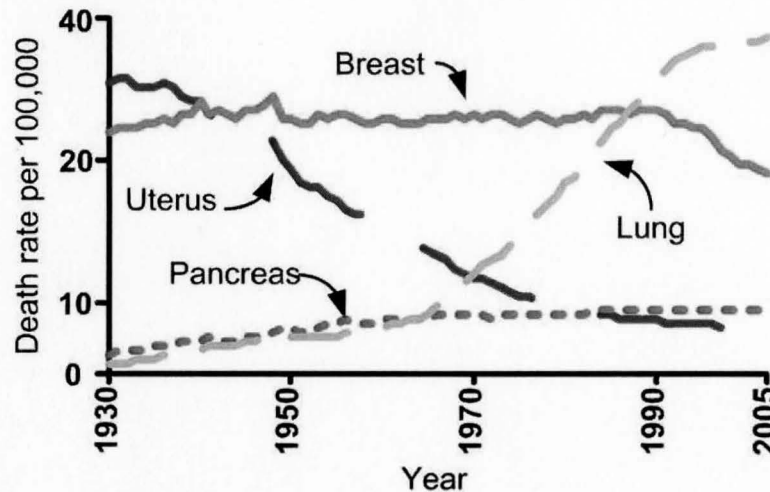


Figure 1.5. Cancer death rates from 1930 to 2001 [7].

Breast cancer, depending on how far the malignant tumor is spread when it is first diagnosed, can be divided into three stages as follows [7]:

- **Local:** invasive malignant tumor, affecting only the organ of origin.
- **Regional:** malignant tumor that is expanded beyond the organ of origin and affects tissues surrounding the organ of origin.
- **Distance:** malignant tumor that has spread into various tissues that are not immediately surrounding the organ of origin.

Relative survival rates of women diagnosed with breast cancer in the first five years after being diagnosed are shown in Table 1.2 [7].

Table 1.2
SURVIVAL RATES OF THE DIFFERENT STAGES OF BREAST CANCER

	All Stages	Local	Regional	Distance
Survival Rate %	88.2	97.9	81.3	26.1

From Table 1.2, the early detection of breast cancer (local stage) is by far the most effective method in increasing the survival rate of the patients. At present, X-ray mammography is the most common and effective screening tool for detection of breast cancer in its early stages.

Although X-ray mammography is the most effective tool in breast cancer screening, it suffers from high false-alarm rate of approximately 10 to 30%, and difficulty in detecting tumors in dense breast tissues. Another shortcoming of X-ray mammography is the discomfort to many patients during the screening procedure caused by the breast compression and the ionization of the breast tissue that is caused by excessive X-ray radiation. Other cancer detection techniques such as magnetic resonant imaging (MRI) or ultrasound are either too expensive or too inaccurate to be used as a general screening tool for early detection of breast cancer [8]. The inherited deficiency in the current breast cancer screening methods raises the need to develop an inexpensive screening tool for routine screening and early detection of breast cancer tumors.

UWB microwave imaging systems have recently shown great potential in detecting breast cancer tumors in early stages and are being considered as a complementary method to the current breast cancer detection modalities [17]. In UWB imaging systems, a wideband pulse is transmitted from an antenna and allowed to impinge on the body. As the pulse propagates through various tissues, reflections occur at interfaces between different tissues. This backscattered signal can be used to map different layers of the body using methods similar to ultrasound imaging.

The reflection from the tissue interfaces is mainly due to the mismatch in their characteristic impedance, which is caused by the difference in the tissues dielectric properties. In the UWB frequency range, the interaction between the UWB signal and biological tissue mainly depends on the tissue's water content. It is reported in the

literature that the malignant breast tissue has a higher water content compared to normal breast tissue [17]. As shown in Figure 1.6, the difference in the water content of the malignant and normal tissue leads to nearly an order of magnitude contrast between their dielectric properties over the UWB frequency range. This contrast is significantly higher than the contrast that can be achieved with X-ray mammography. Further, the high contrast between the dielectric properties of the normal and malignant breast tissue will result in a large reflection from the malignant tumors. Another advantage of using UWB signals in microwave imaging system is that it enables the microwave imaging system to provide both good resolution using the high frequency components and good penetration using the lower frequency components of the UWB operating band. Therefore, it can be concluded that an imaging system employing UWB microwave imaging techniques can potentially detect very small breast cancer tumors in their early stages of development [41].

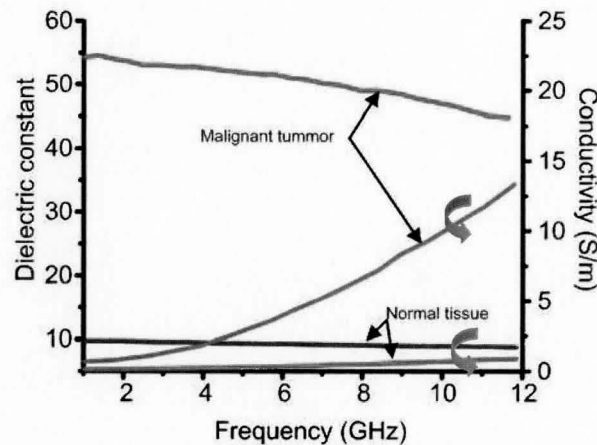


Figure 1.6. Dielectric properties of malignant and normal breast tissue [41].

Also, in the UWB frequency range, the attenuation of microwave signals is less than 4 dB/cm. This low attenuation rate ensures that enough backscattered energy from the tumor deep inside breast tissue can be received [41].

1.4 Motivation for Antenna Design

UWB technology has provided new challenges and opportunities for antenna designers. The design of the antenna has a substantial effect on the performance of UWB communication systems. The main challenge designing antennas for UWB applications is

the requirement to achieve almost 7.5 GHz of input impedance matching while maintaining a stable omni-directional radiation pattern over the UWB operating band. Wideband impedance matching is necessary to ensure efficient transmission and reception of UWB pulses. Also, the omni-directional radiation pattern is required to ensure continuous operating of UWB systems regardless of the receiver and transmitter location in the communication application and to ensure that sufficient amount of energy is received by all the antenna array elements in a UWB microwave imaging system. Aside from the requirements for wideband impedance matching and stable radiation pattern, UWB antennas are required to achieve high fidelity and a constant group delay over the UWB band. The requirement for the high fidelity and linear phase delay is necessary to ensure low distortion in the radiated and received UWB signals. Finally a compact, low profile antenna is preferable given that the target applications of the UWB technology are portable communication system and wireless sensor networks. The UWB antenna requirements and specifications for UWB imaging and communication systems are further described in Section 2.2.

UWB breast cancer detection systems have provided another exciting and challenging opportunity for the design of novel UWB antennas. The UWB antennas have major effects on the performance of breast cancer detection systems. The first challenge facing antenna design for UWB imaging system is the strong reflection from the air-body interface due to the large difference in the dielectric properties of the two media. The reduction of this reflection is necessary to ensure the reception of the tumor response, which may be an order of magnitude smaller than the reflection from the air-body interface. Another major challenge facing antenna design for cancer detection systems is the requirement to achieve input impedance matching over the entire UWB band while maintaining a stable radiation pattern. Wideband matching is required to ensure that the full potential of the UWB pulses is utilized in the detection of breast cancer and the stable radiation pattern is required for simplification of the detection and image reconstruction algorithms. Finally, in order to be practical the antenna must have a small physical size compared to the breast in order to be placed around the breast to form an antenna array.

1.5 Contributions

This thesis presents the design procedure, optimization and measurement results for two wideband antennas for the UWB medical imaging and communication applications. Both antennas are fully characterized in air and in a coupling medium for the UWB imaging and communication applications. Also two antenna arrays based on the UWB antennas have been designed for the UWB imaging applications, and the breast cancer detection capabilities of these arrays have been studied through XFDTD [40], and HFSS [32] simulations and measurements.

The work presented in this thesis has been published in three conferences [26], [59] and [60]. A journal paper was also published [35] and one journal paper based on this work has been submitted [58].

1.6 Thesis Organization

This thesis is organized as follows. Chapter 2 first presents a comprehensive background of the fundamental antenna parameters. Next, the challenges faced in the design of UWB antennas for communication and imaging applications are discussed and the UWB antenna requirements and specifications, in terms of the fundamental parameters, are presented. Finally, Chapter 2 concludes with a literature review of antennas suitable for UWB imaging applications. Chapter 3 presents a solution for reducing the reflection of electromagnetic energy in the air-body interface. The design of the coplanar waveguide used to feed the antennas for the communication and imaging application is presented as well. Chapters 4 and 5 present the design, optimization, simulations and measurement results of the tapered square monopole antenna and a tapered slot antenna for the UWB communication and imaging applications. The antenna characteristics, while operating in free space for communication applications, and operating in a coupling medium, for imaging applications, are studied. Finally, the design of two antenna arrays for UWB imaging application is presented and the tumor detection capabilities of the antenna arrays are investigated. Finally, Chapter 6 concludes with a summary of this work. Future work and areas for improvement are also be given in this chapter.

Chapter 2: ANTENNA BACKGROUND

This chapter presents a detailed description of the fundamentals of antennas. The requirements and specifications of UWB antennas in terms of the antenna fundamental parameters are presented to provide a sound understanding of the challenges posed by UWB antenna design for communication and microwave imaging systems.

In the second part of this chapter, a literature review of UWB antennas for biomedical imaging applications is presented. A detailed description of the design procedure of each antenna is discussed, and their advantages and shortcomings are investigated for UWB medical imaging applications.

2.1 Fundamental Antenna Parameters

An understanding of fundamental antenna parameters is necessary to fully characterize an antenna and to determine whether it is suitable for the target application. In this section, an overview of fundamental antenna parameters such as impedance bandwidth, gain, directivity, polarization and radiation pattern is presented.

2.1.1 Impedance bandwidth

The impedance bandwidth is defined as the frequency range over which the input impedance of the antenna is sufficiently matched to the output impedance of the feed line so that less than 10% of the transmitted voltage is reflected back. The impedance bandwidth is characterized by measuring of the voltage standing wave ratio (VSWR) or the return losses, which depend on the reflection coefficient. The reflection coefficient Γ is defined as [9]

$$\Gamma = \frac{V_{0-}}{V_{0+}} = \frac{Z_{Line} - Z_{Load}}{Z_{Line} + Z_{Load}}, \quad (2-1)$$

where V_{0-} is the reflected wave, V_{0+} is the incident wave; and Z_{line} and Z_{load} are input impedance of the excitation source and the antenna, respectively. Thus, the impedance bandwidth is the frequency range over which $\Gamma < 0.316$.

If the antenna is not matched to the feed line, a portion of the transmitted signal is reflected and it travels back along the transmission line in the opposite direction to that of the incident wave. The combination of transmitted and reflected waveforms creates a standing wave in the transmission line. The VSWR measures the ratio of the amplitudes of the maximum standing wave (V_{\max}) to the minimum standing wave (V_{\min}), and can be calculated [9] by the following equation:

$$VSWR = \frac{V_{\max}}{V_{\min}} = \frac{1+|\Gamma|}{1-|\Gamma|}, \quad (2-2)$$

A VSWR smaller than 1.925 implies a good match between the antenna and the transmission line. It also implies that only 10% of the incident wave has been reflected due to the mismatch between the antenna input impedance and the feed line characteristic impedance. Thus, VSWR can be used to characterize the impedance bandwidth as well.

Another measure for the antenna matching is the return loss, which can be calculated as follows [9]:

$$\text{Return loss} = -10 \text{Log} |S_{11}|^2, \quad (2-3)$$

where S_{11} is a scattering parameter of antenna-under-test. A return loss less than -10 dB indicates that less than 10 % of the incident wave has been reflected due to the mismatch.

2.1.2 Radiation pattern

According to the IEEE Standard Definitions of Terms for Antennas [10], the radiation pattern is defined as:

“a mathematical function or a graphical representation of the radiation properties of the antenna as a function of space coordinates. In most cases, the radiation pattern is determined in the far-field region and is represented as a function of the directional coordinates. Radiation properties include power flux density, radiation intensity, and field strength, directivity, phase or polarization.”

Three-dimensional or two-dimensional radiation patterns are obtained by plotting a spatial distribution of the radiated energy as a function of the observed position along a

path or surface of constant radius [11]. Three-dimensional radiation patterns are normally plotted in the spherical coordinate system. On the spherical coordinate system, the XZ-plane corresponds to the elevation plane ($\theta = 0^{\circ}$ - 360° , $\varphi=0^{\circ}$) which contains the electric field vector (E-plane) and XY plane corresponds to the azimuth plane ($\theta = 90^{\circ}$, $\varphi=0^{\circ}$ - 360°), which contains the magnetic field vector (H-plane). Two dimensional radiation patterns are obtained by plotting a cross-section (plane of constant θ or φ) of the three dimensional radiation patterns in a polar coordinate system.

A three-dimensional radiation pattern of a $\lambda/2$ dipole is plotted in Figure 2.1. The radiation pattern is obtained by plotting the magnitude (dB) of the radiated E-field around a surface of constant radius. It is observed that there is a null in the radiation pattern at $\theta = 0^{\circ}$ and the maximum of the radiation pattern is constant at $\theta = 90^{\circ}$ for any value of φ . Two dimensional radiation patterns of the $\lambda/2$ dipole, in the elevation and azimuth planes, are plotted in Figure 2.2. The two-dimensional plots show that there is null in the radiation pattern at $\theta = 0^{\circ}$ and the maximum in radiation pattern is constant at $\theta = 90^{\circ}$ for any value of φ . This particular radiation pattern can be fully described using a pair of two-dimensional radiation patterns in the elevation and azimuth planes.

In general, antennas can be classified according to their radiation patterns as follows [12].

a) Isotropic antenna

This is an antenna in which the radiation pattern has equal radiation in all directions. This is an ideal concept that is not physically achievable. However, it is used to define other antenna parameters. It is represented simply by a sphere with a center that coincides with the location of the isotropic radiator.

b) Directional antenna

A directional antenna radiates or receives radiation much more efficiently in certain directions than in others. Usually, this term is applied to antennas with a directivity that is much higher than that of a half-wavelength dipole.

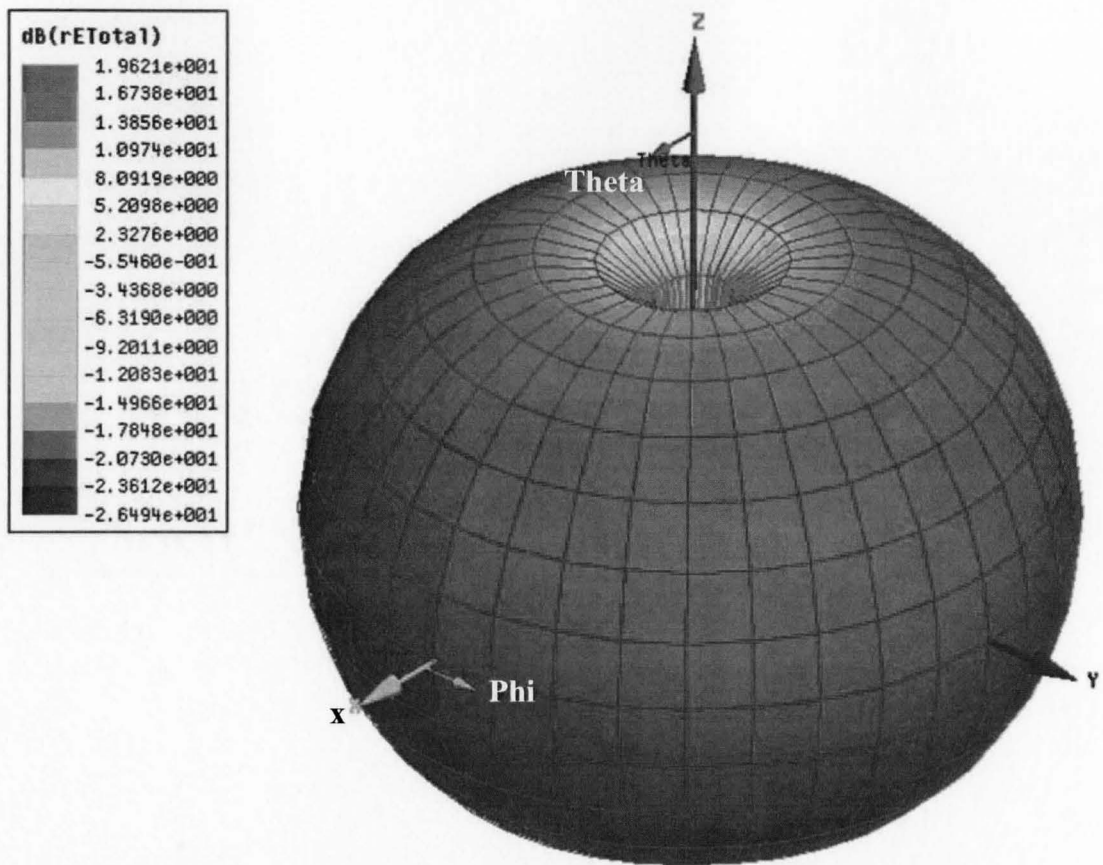


Figure 2.1. Three-dimensional radiation pattern of $\lambda/2$ dipole.

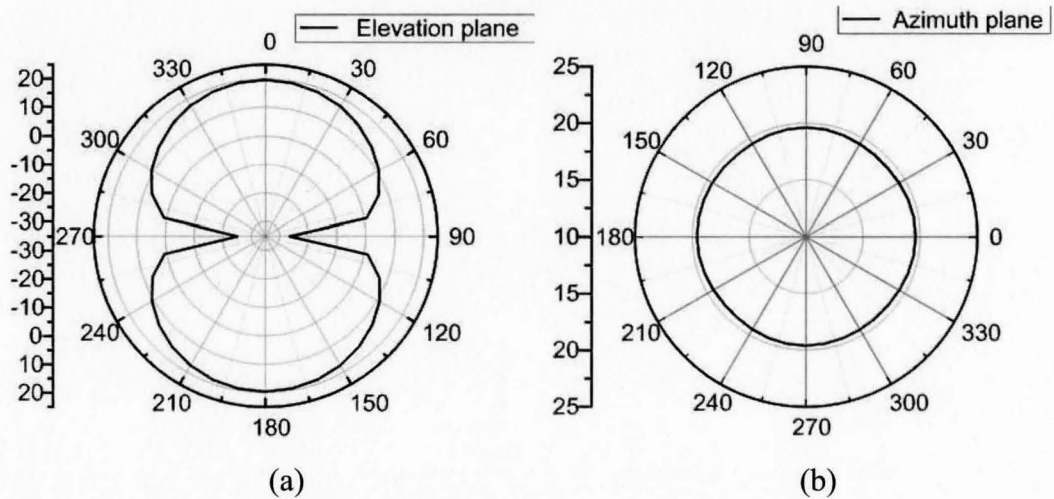


Figure 2.2. Two-dimensional radiation pattern in (a) elevation plane and (b) azimuth plane, of $\lambda/2$ dipole.

c) **Omnidirectional antenna**

An omnidirectional antenna has a non-directional pattern in a given plane, and a directional pattern in any orthogonal plane. The $\lambda/2$ dipole is an example of such an antenna. As shown in Figure 2.1, the antenna has a non-directional pattern in the XY-plane and a directional radiation pattern in the ZX plane.

The far-field radiation pattern of an antenna is measured best in an anechoic chamber. This is done by placing the antenna-under-test at one end of the chamber, and a standard gain antenna at the other end of the anechoic chamber. The azimuth plane measurements are performed by rotating the antenna-under-test in the XY- plane in the φ direction for a constant θ . The elevation plane measurements are done by rotating the antenna-under-test in the ZX plane in the θ direction for a constant φ . The measurement results are plotted on a polar plot, with 0° indicating the direct line of sight.

2.1.3 Half-power beamwidth

Half-power beamwidth is defined as [11]:

“In a plane containing the direction of the maximum of a beam, the angle between the two directions in which the radiation intensity is one-half the maximum value of the beam”

In other words, the half-power beamwidth describes the angular distance from the center of the main beamwidth to the point at which the radiated power is -3 dB below the peak radiated power. An example of a half power beamwidth measurement for a directional antenna is shown in Figure 2.3.

Half-power beam width measurements describe the antenna radiation pattern and indicate how directional the antenna is. It can also describe the antenna resolution capabilities in detecting adjacent radiating sources or radar targets.

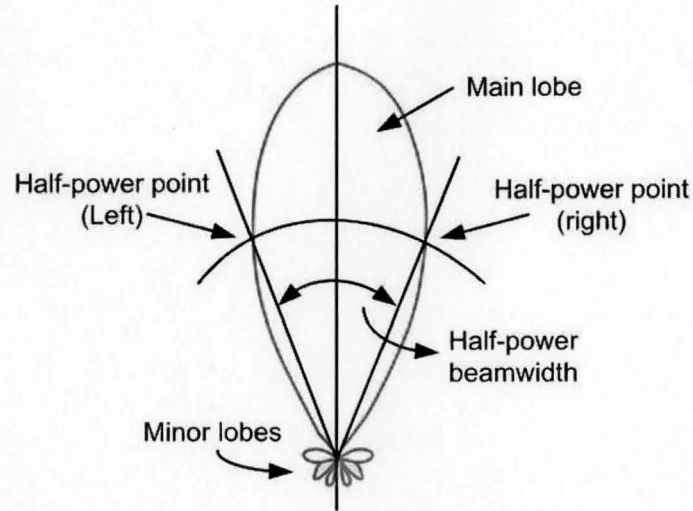


Figure 2.3. Half-power beamwidth.

2.1.4 Directivity

According to the IEEE standard [10], the directivity of an antenna is defined as:

“The ratio of the radiation intensity in a given direction from the antenna to the radiation intensity averaged over all directions”

where the average radiation intensity of an antenna can be calculated by dividing the total power radiated by the antenna by 4π . In other words, the directivity of an antenna is equal to the ratio of its radiation intensity in a given direction over that of an isotropic source.

The directivity of an antenna can be computed as follows [11]:

$$D = \frac{U}{U_0} = \frac{4\pi U}{P_{rad}}, \quad (2-4)$$

where U is the radiation intensity of the antenna, U_0 is the radiation intensity of an isotropic source and P_{rad} is the total radiated power by the antenna. Directivity is a dimensionless quantity with a maximum of unity.

2.1.5 Efficiency

The antenna efficiency estimates the total energy losses in an antenna. In general, antenna losses are caused by ohmic losses in the conductors, losses in the dielectric materials

surrounding the antenna and reflective losses at the input of the antenna. The total antenna's efficiency can be calculated as follows [11]:

$$e_t = e_r \times e_c \times e_d, \quad (2-5)$$

where e_r is the reflection efficiency, e_c is the conduction efficiency and e_d is the dielectric efficiency. It is very difficult to compute e_c and e_d separately, and even in measurement, it is difficult to separate them. Therefore, it would be more convenient to combine e_c and e_d and write the total antenna efficiency as follows [11]:

$$e_t = e_r \times e_{cd}, \quad (2-6)$$

where $e_{cd} = e_c \times e_d$ is the antenna's radiation efficiency.

Reflection efficiency, which is due to the impedance mismatch at the input terminal of the antenna, is directly related to the reflection coefficient Γ . The reflection efficiency is defined as follows [11]:

$$e_r = 1 - |\Gamma|^2. \quad (2-7)$$

To measure the radiation efficiency, we should take into account both the conduction efficiency and the dielectric efficiency. The radiation efficiency is determined by the ratio of the radiated power, P_{rad} , to the input power at the terminals of the antenna, P_{in} [11]:

$$e_{cd} = \frac{P_{rad}}{P_{in}}. \quad (2-8)$$

2.1.6 Gain

The antenna gain is linearly related to its directivity through its efficiency. According to the IEEE standard [10], the absolute gain of antenna is defined as:

“the ratio of the radiation intensity U in a given direction to the radiation intensity that would be obtained, if the power fed to the antenna were radiated isotropically”.

Mathematically, the antenna's gain can be expressed as follows [11]:

$$G = e_{rad}D = 4\pi \frac{U(\theta, \phi)}{P_{in}}, \quad (2-9)$$

where $U(\theta, \phi)$ is the antenna radiation intensity in a given direction. If the direction of the gain measurement is not mentioned, then the direction of maximum gain is assumed.

The antenna gain provides a concise measure of its performance due to the fact that it considers the losses in the antenna structure. However, it should be noted that a higher antenna gain does not necessarily imply a better antenna performance. Given that the antenna gain is linearly related to the directivity, higher gain implies a more directional radiation pattern, and lower gain implies a more omnidirectional radiation pattern, assuming good radiation efficiency.

2.1.7 Polarization

The antenna polarization is defined as the polarization of the wave transmitted or received by the antenna, and it is usually defined in the direction of maximum gain. In general, the antenna's polarization varies with operating frequency and direction from the center of the antenna. According to [11], the polarization of a radiated wave is defined as the properties of electromagnetic waves describing the time varying direction and relative magnitude of the electric-field vector. Specifically, it is the curve traced as a function of time by the extremity of the vector at a fixed location in space, and the sense in which it is traced, as observed against the direction of propagation. In other words, polarization is the curve traced by the end point of an arrow representing the instantaneous electric field

The antenna's polarization can be classified into three categories: linear polarization, circular polarization and elliptical polarization depending on the shape of the curve traced, as shown in Figure 2.4. A wave is linearly polarized if the variation in the vector describing the field vs. time is always directed along a straight line. Elliptical polarization occurs when the field vector describing the E-field traces an ellipse as a function of time; and in the same manner, circular polarization occurs when the field vector describing the E-field traces a circle as a function time.

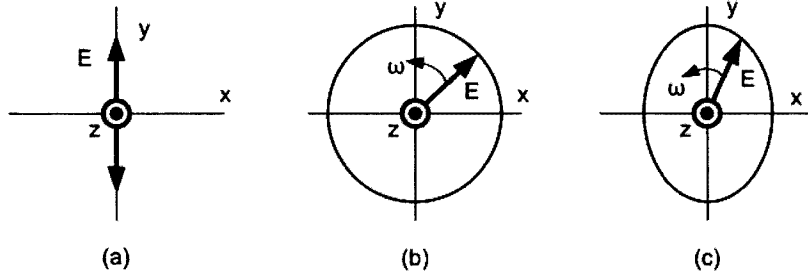


Figure 2.4. (a) Linear polarization, (b) circular polarization, and (c) elliptical polarization.

In the case of linear polarization, the field is horizontally polarized if the variation in the E-field is directed along the x-axis, and it is vertically polarized if the variation in the E-field is directed along the y-axis. In the case of circular or elliptical polarization, if the rotation of the vector describing E-field as a function of time is clockwise, then the field is right-hand circularly or elliptically polarized. If the rotation is counter-clockwise, then the field is left-hand circularly or elliptically polarized.

In general, the polarization of the incoming wave is not similar to the polarization of the receiver antenna. Due to this polarization mismatch, the receiver antenna does not receive the maximum available power from the incoming wave. This effect is known as polarization loss factor (PLF) and it can be computed as follows [11]:

$$\text{PLF} = \left| \hat{p}_w \times \hat{p}_a \right| = |\cos \psi_p| \quad (2-10)$$

where \hat{p}_w is the polarization vector of the incoming wave, \hat{p}_a is the polarization vector of the receiver antenna, and ψ_p is the angle between the two unit vectors. If the receiver antenna polarization is the same as the incoming wave polarization, then PLF is equal to one, which implies that maximum power is extracted from the incoming wave.

2.1.8 Fidelity

In the time domain, the performance of the antenna is evaluated by its *fidelity*. Mathematically, the fidelity is defined as follows:

$$F = \max_{\tau} \int_{-\infty}^{\infty} \hat{r}(t + \tau) \hat{f}(t) \partial t, \quad (2-11)$$

where

$$\hat{r}(t) = \frac{r(t)}{\int_{-\infty}^{\infty} r^2(t) dt}, \quad (2-12)$$

$$\hat{f}(t) = \frac{f(t)}{\int_{-\infty}^{\infty} f^2(t) dt} \quad (2-13)$$

where $r(t)$ is the observed E -field and $f(t)$ is the time derivative of the input signal to the antenna. From equation (2-11), the *fidelity* is a measure of how accurately the voltage available at the antenna terminals represents the field received by the antenna, or in the transmitting case, the *fidelity* shows how accurately the radiated field represents the ideal output of the antenna [38], [39]. Numerically, fidelity is defined to be $0 < F < 1$, where $F = 1$ would be an exact match of the received signal to the expected signal. In other words, fidelity is the maximum of the cross-correlation of two signals that are normalized to their energy levels.

2.2 UWB Antenna Requirements

The fundamental parameters of an antenna, described in section 2.1, should be carefully considered when designing antennas for UWB applications. In addition, UWB system requirements impose additional constraints on the antenna design. The first and the most important constraint is that the antenna should be able to operate throughout the entire UWB frequency band from 3.1 to 10.6 GHz, which implies that the antenna should achieve more than an octave of impedance bandwidth. Another parameter that is not considered in narrow band antenna designs, but has significant effects on the UWB antenna's performance, is group delay. Group delay is a measure of the delay that is

experienced by each frequency component in the operating band. Group delay is calculated by taking the first derivative of the s-parameters phase. If the phase is linear over the operating frequency band, then the group delay is constant for the given band. A constant group delay implies that the delay experienced by each frequency component over the UWB operating band is the same, thus ensuring low distortion of the received pulse.

Antenna ringing is another parameter that should be taken into account when designing UWB antennas. Antenna ringing occurs when a short time-domain pulse (for example, a 200 ps Gaussian shape) is used to excite the antenna. Due to the ringing effect, the transmitted pulse is spread in time-domain and the shape of the pulse is distorted. The antenna ringing can be avoided by designing UWB antennas with a low Q -factor. The low Q -factor causes the unwanted signals to die more quickly, thereby leaving the shape of the transmitted pulse much closer to desired shape [13]. The Q -factor of an antenna is defined by:

$$Q - factor = \frac{f_0}{f_H - f_L}, \quad (2-14)$$

where f_0 is the center frequency of the antenna and f_H and f_L are its upper and lower 3 dB frequencies. The expression given in equation (2-14) is valid for narrow-band antennas. The mathematical presentation of the Q -factor for the UWB antennas is currently a research topic and it is not well defined [66].

The radiation pattern of the antenna is also an important characteristic that must be taken into account when designing UWB antennas. In UWB imaging and communication systems, a nearly omnidirectional radiation pattern is desirable over the entire UWB operating band. This relaxes the constraint on the design of UWB antenna arrays for near-field imaging systems and the location of transmitter and receiver antenna in a UWB communication system. In this research, the primary application of UWB antennas is in UWB biomedical imaging systems and portable communication systems. For this application, compact planar antennas with the following requirements are desirable:

Table 2.1

UWB ANTENNA'S REQUIREMENTS

Impedance bandwidth	3.1-10.0 GHz
Radiation pattern	Omnidirectional
Radiation efficiency	High (>70%)
Gain	Low
Directivity	Low
Half-power beamwidth	> 70°
Phase	Linear
Fidelity	High
Radiation Efficiency	High

2.3 Literature Review

This section provides an overview of several antennas that have been designed for UWB cancer detection systems. The design of each antenna is discussed along with its performance characteristics in a UWB imaging system.

2.3.1 Microstrip-fed “dark eyes” antenna

The dark eye antenna is based on printed diamond dipole antennas [14]. The dark eye antenna is differentially fed with a printed microstrip-to-slotline transformer [15], [16]. The geometry of the antenna and the balanced feed line are shown in Figure 2.5. The radiating elements are symmetric around the feed point and each section of the radiating element is divided into two sections. The first section is a metallic bowtie connected to the apex of the antenna. The second section is a resistively loaded triangle with a constant sheet resistance R_s . The resistively loaded section of the radiating element improves the impedance bandwidth of the antenna by reducing the *Q-factor* and by attenuating the reflected current from the sharp edges of the radiating elements. To reduce unwanted radiation from the feed of the antenna, a resistive parasitic layer is placed over the top dielectric layer covering the microstrip-to-slotline transformer.

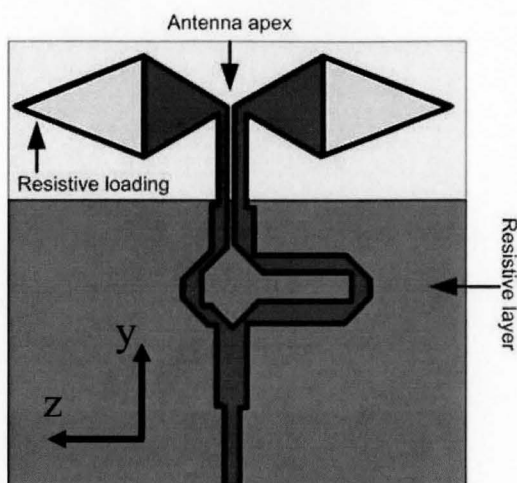


Figure 2.5. Geometry of dark eye antenna [14].

For the purpose of breast cancer detection, the antenna is immersed in a lossless coupling medium with $\epsilon_r = 10.2$. Simulated input matching of the antennas in the dielectric medium for different sheet resistances is plotted in Figure 2.5. The simulated input matching of the antenna is better than -10 dB across the entire UWB operating band. The near-field radiation pattern of the antenna is studied at a single frequency and it is found that the near-field radiation pattern in the E-plane consists of two local maxima directed in the $\varphi = -60^\circ$ and $\varphi = 60^\circ$ with a local minimum at $\varphi = 0^\circ$, as shown in Figure 2.7. In the H-plane, the maximum radiation is directed at $\theta = 60^\circ$, as shown in Figure 2.8, where the asymmetry in the radiation pattern results from the presence of the asymmetric feeding structure in the vicinity of the radiating element.

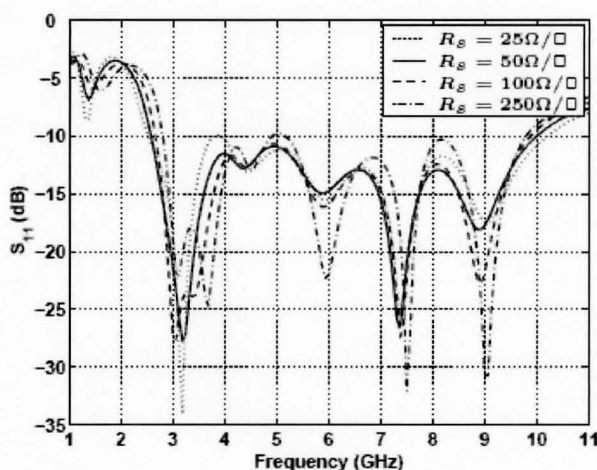


Figure 2.6. Simulated antenna input impedance for different sheet resistances [14].

The dark eye antenna is an inherently inefficient radiator due to the resistive loading of the radiation element. Resistive loading significantly increases the cost and complexity of the antenna fabrication. As a result, the dark eye antenna has not been fabricated and measurement results are not available to confirm the validity of the simulation results.

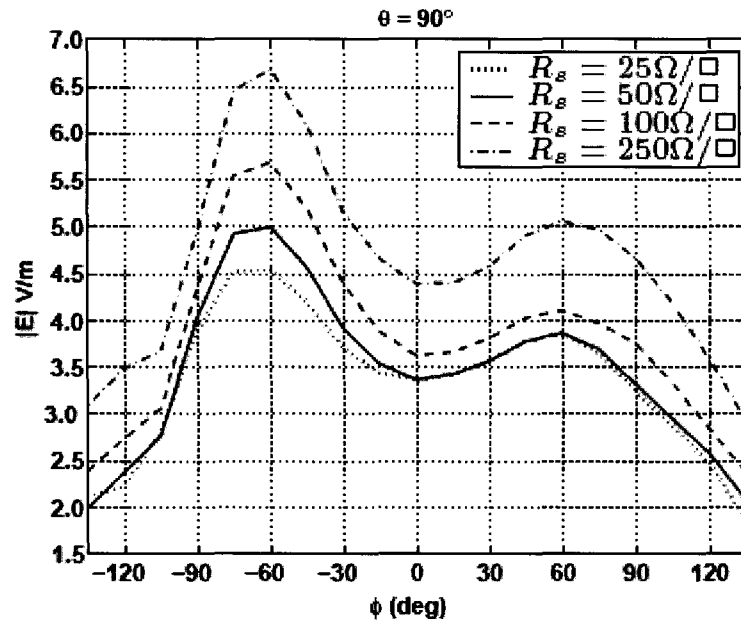


Figure 2.7. Simulated antenna near field (E-plane) [14].

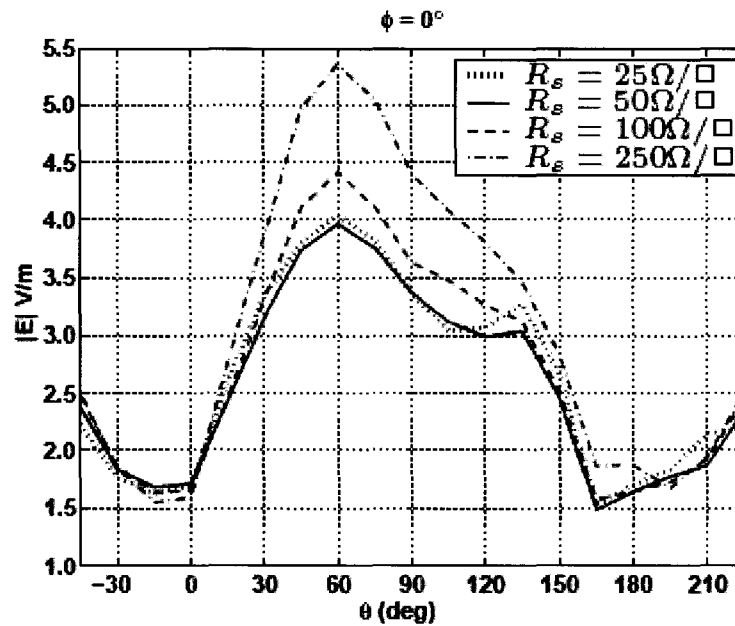


Figure 2.8. Simulated antenna near field (H-plane) [14].

2.3.2 Ultra-low reverberation antenna

The ultra-low reverberation antenna is a differentially fed, 2D printed bowtie antenna shown in Figure 2.9. Each section of the bowtie is made of a material with the following conductivity profile [17]:

$$\sigma(z) = \sigma_0 \times \frac{1 - z/h}{1 + \left(\frac{\sigma_0}{\sigma_{1/2}} - 2 \right) \times \left(\frac{z}{h} \right)}, \quad (2-15)$$

where z/h is the normalized axial distance along the bowtie, σ_0 is the conductivity of the metal used at the feed of the antenna, and $\sigma_{1/2}$ is chosen to set the desired suppression level of the reflected signal from the edges of the antenna. It is reported [21] that by setting $\sigma_{1/2}$ to 1.0 S/m, that the reflection from the edges of the antenna can be attenuated by more than -125 dB relative to the excited pulse, compared to -63 dB attenuation in the case of the all-metal bowtie antenna.

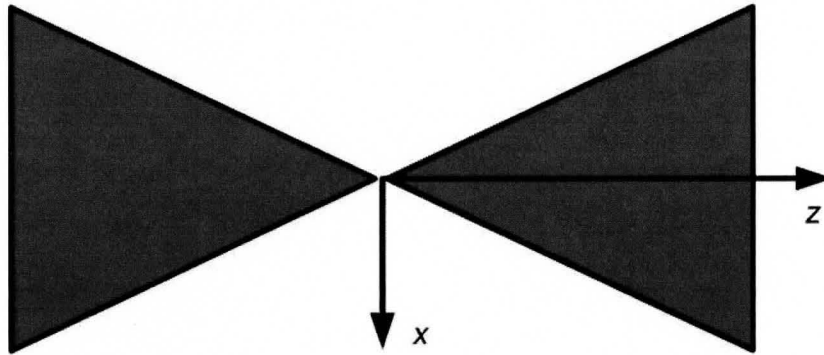


Figure 2.9. Geometry of co-polarized bowtie antenna. [17]

The authors in [17] did not provide simulation or measurement results for the reflection coefficient of the antenna. Therefore, it is not possible to judge the performance characteristics of this antenna for near-field imaging applications.

The main drawback of the ultra-low reverberation antenna is the resistive profile of the radiating elements. The resistive loading of the antenna significantly reduces its radiation efficiency. Additionally, this antenna is extremely complicated to fabricate due

to its complicated resistive profile. Another drawback of this antenna is the requirement for the balanced feed, which is very difficult to design throughout the UWB frequency range.

A variation of the bowtie antenna has been designed [18] to measure the cross-polarized reflections from tumors close to a planar chest wall. To obtain the cross-polarized response, two resistively loaded bowtie antennas in a Maltese cross formation have been used. The geometry of the proposed antenna is shown in Figure 2.10. In this design, one bowtie antenna is excited and the cross polarized response is observed on the second antenna. In [17], it was found through FDTD simulation that by observing the cross-polarized response of tumors close to a planar chest wall, the response due to the chest wall can be completely rejected. Since the response from the chest wall arrives at approximately the same time as the tumor response, this antenna significantly improves the performance of the UWB imaging system.

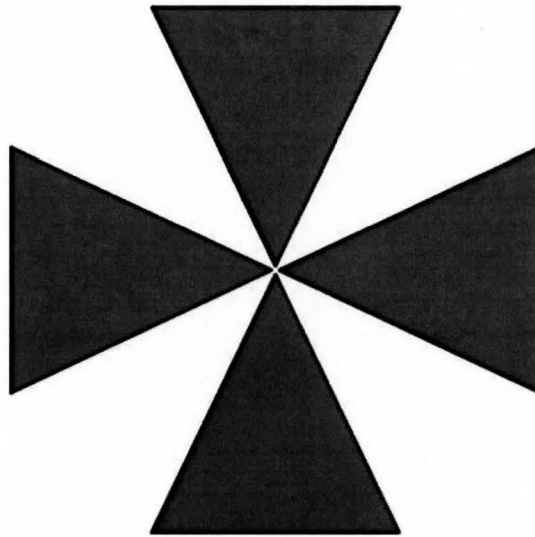


Figure 2.10. Cross-polarized bowtie antenna [17].

In [18], measurement results of all-metal, cross-polarized bowtie antennas were provided. But there was no conclusion on whether these types of antennas are actually capable of improving the overall performance of imaging systems for tumors close to a planar chest wall. The antenna in [18] required a balanced wideband feed, which is both costly and complicated to fabricate in commercial systems. Also, the array element was not able to utilize the full potential of UWB pulses due to its narrow impedance

bandwidth, as shown in Figure 2.11, where S_{11} and S_{22} are the reflection coefficients of the transmitter and the receiver antennas, respectively.

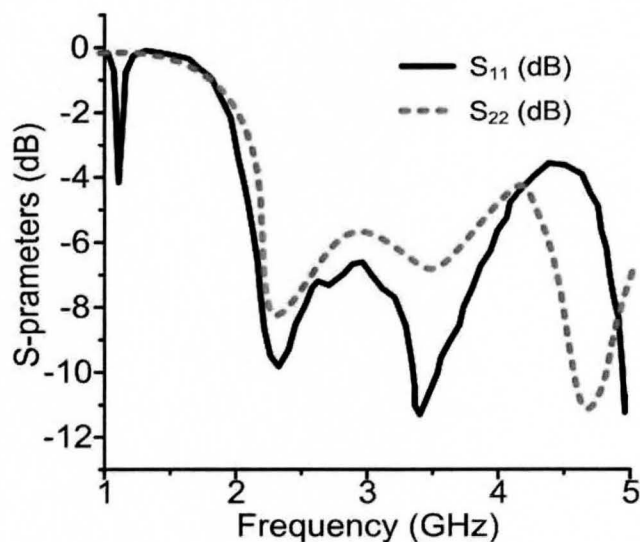


Figure 2.11, Measured input matching of cross-polarized bowtie antenna [18].

2.3.3 Resistively loaded Wu-King monopole antenna

A photograph of the Wu-King monopole antenna is shown in Figure 2.12. The antenna structure consists of sections of microstrip transmission lines that are connected to each other using high-frequency chip resistors (Vishay 0603HF). In this design, the length of the antenna is set to 10.8 mm, and the antenna is immersed in a lossless coupling medium with $\epsilon_r = 3.0$. [19].



Figure 2.12, Photograph of Wu-King monopole antenna [19].

The simulated and measured VSWR of the Wu-King monopole antenna are shown in Figure 2.13. The antenna VSWR is below 2 from 7-10 GHz, which is only a small section of the UWB operating band. The simulated radiation efficiency of the

antenna varies from 1.9% to 15.8% over the 2 to 8 GHz frequency range. The low radiation efficiency of the antenna can be attributed to the resistive loading that is used to achieve a broad impedance bandwidth.

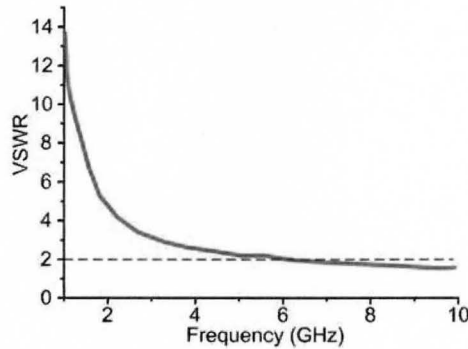


Figure 2.13. Measured VSWR [19].

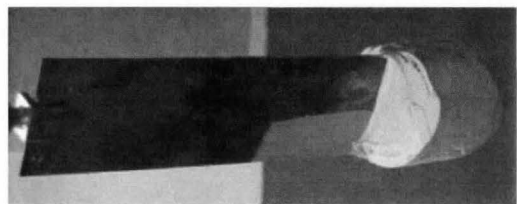
Another shortcoming of this antenna is its 3D structure, which is due to the requirement of a large ground plane at the feed of the antenna. The requirement of a 3D ground plane places a severe constraint on the breast models and the antenna array formation that can be used in cancer detection systems. The combination of poor VSWR and radiation efficiency, plus the need for a large ground plane, makes this antenna unsuitable for a breast cancer imaging system.

2.3.4 Dielectric-filled slotline bowtie antenna

A photograph of the slot line bowtie antenna is shown in Figure 2.14(b). The antenna consists of a shaped slot with Vivaldi, linear and elliptical sections along its tapering profile. The tapering profile of the slot controls the antenna return loss over the entire UWB operating band. Two bowtie plates are connected to the tapered slot, to provide control over the antenna's beamwidth. Also, an integrated UWB microstrip balun has been used to feed the antenna differentially [19].



(a)



(b)

Figure 2.14. (a) Slot line bowtie antenna, and (b) dielectric slot line bowtie antenna [19].

To improve the coupling of the energy into the human body, the antenna plates were immersed in a dielectric epoxy (Eccostock Hi K Cement, Emerson & Cuming Microwave Products, Randolph, MA, USA) with $\epsilon_r=10$. The photograph of the antenna immersed in the coupling medium is shown in Figure 2.14(b).

The measured and simulated return loss of the antenna in the coupling medium is plotted in Figure 2.15. The simulated return loss of the antenna (without the balun) is below -10 dB from 2.5 to 10 GHz. The measured return loss of the antenna, without de-embedding the balun and the microstrip line, is below -10 dB from 2.6 to 8 GHz.

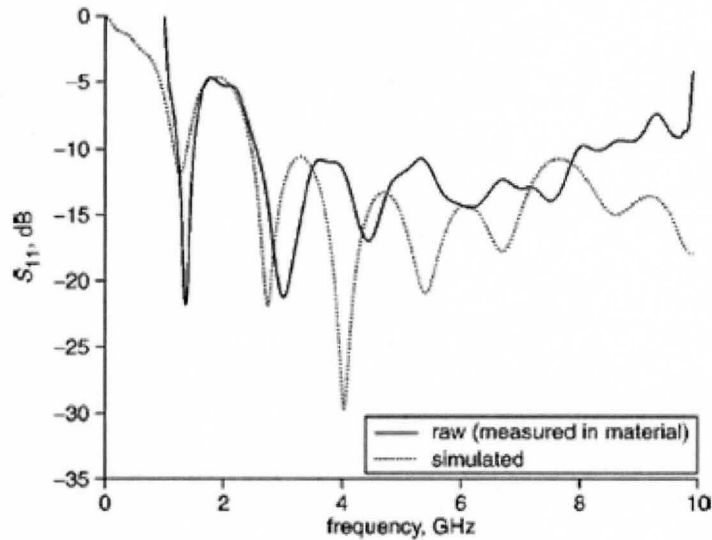


Figure 2.15. Measured and simulated return loss of dielectric field bowtie antenna [19].

Simulation results show that the antenna's beamwidth is 32° . Therefore, this antenna can be classified as a directional antenna.

Although the slotline bowtie antenna achieved an acceptable impedance bandwidth and a good radiation characteristic, it suffers from the fact that it has a 3D structure which significantly increases the manufacturing cost. Also, the antenna is fabricated on an expensive dielectric substrate (Rogers RT = Duroid 6010.2LM, Rogers Corporation, Rogers, CT, USA), which will further increase the cost of fabrication. Finally, the need for the wideband balun further increases the physical dimension and hence the cost of the antenna.

2.3.5 Ultra-wideband ridged pyramidal horn antenna

The geometry of the ultra-wideband, ridged, pyramidal, horn antenna is shown in Figure 2.16. This antenna consists of a pyramidal horn, a ridge, and a curved launching path terminated with a pair of 100 Ω resistors [20].

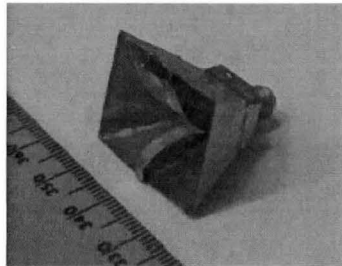


Figure 2.16. Photograph of the ridged pyramidal horn antenna [20].

Although horn antennas typically have narrow impedance bandwidth, in this design, the bandwidth of the horn antenna is increased significantly by adding metallic ridges to the waveguide and flared sections.

A cross section of the antenna is shown in Figure 2.17. The flare section of the horn antenna is connected to the outer conductor of the coaxial line feeding the antenna. In this design, the pyramidal horn antenna acts as a ground plane and provides an appropriate return path for high frequency current, thus eliminating the need for a differential feed. The ground plane also limits the main beam of the antenna, ensuring a compact, directional main beam. The curved launching path of the antenna is connected to the signal line of the coaxial feed. Microwave energy is directed and launched into the surrounding medium from this launching path. To suppress reflections from the end of the launching path and to improve the input impedance matching, pair of 100 Ω terminating resistors is connected from the end of the launching path to the ground plane.

The ridged pyramidal horn antenna achieves excellent input impedance matching over the entire UWB operating band. The measured and simulated VSWR of the antenna is plotted in Figure 2.18. Both measured and simulated VSWR of the antenna is below 1.5 from 1 to 11 GHz. Wideband input impedance matching of the antenna can be attributed to the curved launching path and the termination resistors, which suppresses the reflected signals from the end of the launching path.

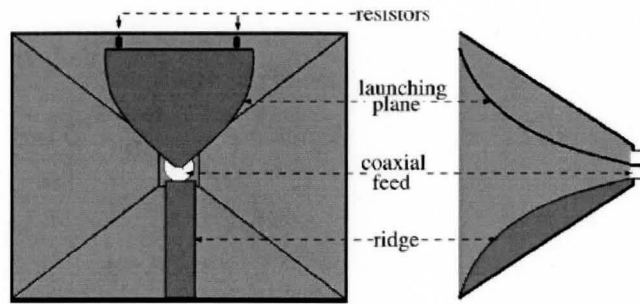


Figure 2.17. Geometry of the ridged pyramidal horn antenna [20].

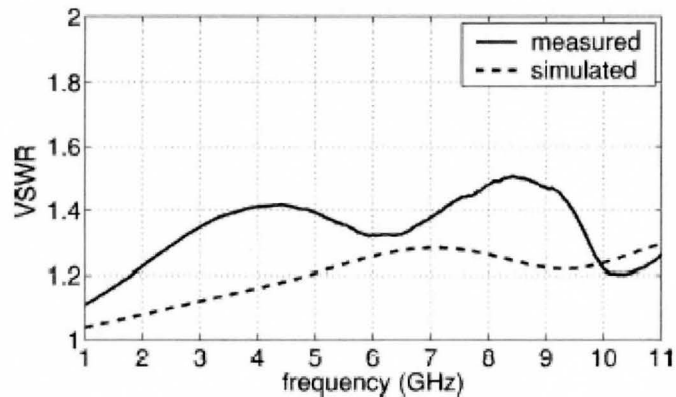


Figure 2.18. Simulated and measured VSWR of the antenna [20].

Overall, the ridged pyramidal horn antenna is a good candidate for breast cancer imaging systems due to its compact size, excellent input impedance matching and compact radiation pattern. The only disadvantage of this antenna is its 3D structure, and the resistive nature of the antenna, which significantly reduce the antenna's overall radiation efficiency.

2.4 Summary

This chapter presented an overview of the fundamental parameters of antennas - gain, polarization, impedance bandwidth and etc. Challenges facing the design of UWB antennas for medical imaging and communication applications were presented, and the general requirements and specifications of the UWB antenna targeting imaging and communication applications were provided. Finally, a selected literature review of UWB antennas for medical imaging applications was presented and the advantages and shortcomings of each antenna for UWB medical imaging applications were discussed.

Chapter 3: CHOICE OF COUPLING MEDIUM AND DESIGN OF COPLANAR WAVEGUIDES

One of the major challenges in designing an antenna for an ultra-wideband (UWB) medical imaging system is maximizing the coupling of energy into the human body. In this chapter, we will investigate different reflection mechanisms that the transmitted electric field experiences as it travels through different layers of tissue. It is found through our study that the coupling of energy into the human body can be maximized by placing the UWB antenna in a coupling medium with dielectric properties close to that of human tissue.

All antennas designed in this work are fed with coplanar waveguides (CPWs). The CPW structure has an important advantage in that the signal and ground lines are on the same side of the printed circuit board (PCB). Because of this, the manufacturing of the antenna is simplified and no vias are required, hence reducing parasitic effects which would degrade the antenna's performance. The characteristic impedance of a CPW greatly affects the performance characteristic of UWB antennas. Therefore, it is necessary to design the CPW with characteristic impedance close to 50Ω to minimize the effect of CPW on the overall antenna's reflection characteristic. In this chapter, the design procedure and calculation of the geometrical parameters for CPWs operating in air and in the coupling medium, are discussed.

3.1 Choice of the Coupling Medium

In an UWB imaging system, the human body is irradiated with a short Gaussian pulse, transmitted from a UWB antenna that is placed in close proximity to the tissue of interest. As the pulse propagates through the human body, it is partially reflected at the various interfaces between tissues due to the differences in their intrinsic impedances. This backscattered signal can be used to map the different layers of human body using methods similar to those used in ultrasound imaging, in which an acoustic pulse is impinged on the body and the reflected pulses from different tissue interfaces are used to

map the internal structure of the human body. A major problem facing the design of UWB imaging systems is the large reflection from the air-skin interface due to the large difference in the dielectric properties of the two media ($\epsilon_{r\text{-skin}} \sim 36$, $\epsilon_{r\text{-Air}} = 1$). This reflected energy is orders of magnitude larger than that backscattered from the tumor, and it can also cause ringing at the input of the receiver antenna [25]. As a result, the reflection from the air-skin interface can potentially cover the tumor response and reduce the overall performance of UWB imaging system. One solution to this problem is to immerse the antenna in a coupling medium with electrical properties close to that of human tissue and to place the antenna and the coupling medium together on the human body. In this method, the reflection from the air-skin interface is largely reduced, resulting in the efficient coupling of the radiated energy into the human body, thus improving the overall performance of the UWB imaging system.

3.1.1 Study of the reflection mechanism

In the case of breast cancer detection, the transmitted pulse first encounters the air-skin interface and then the skin-breast interface. As a result, there are two options for the matching material, either to match to the skin layer or to the breast tissue. To find the best material for the coupling medium, we should first study the reflection characteristics of the transmitted pulse as it propagates through different tissue layers. Consider the common case where the wave is impinging on a three-layer body model shown in Figure 3.1. Assume that layer 1 (air) and layer 3 (breast tissue) are infinite, therefore, no wave will be reflected from the other sides of layers 1 and 3. As shown in Figure 3.1, the waves will be partially reflected at the air-skin interface, and the other part will propagate through the skin and partially be reflected back at skin-fat interface. Hence, there are multiple reflections inside the skin layer. The reflection coefficient Γ at each layer's interface is given by [9]

$$\Gamma = (\eta_2 - \eta_1) / (\eta_2 + \eta_1), \quad (3-1)$$

where η_i is the intrinsic impedance of the material i and it is given by [9]

$$\eta_i = \frac{j\omega\mu_i}{\gamma_i}, \quad (3-2)$$

where ω is the operating frequency, μ_i is the permeability of the medium i and γ_i is the complex propagation constant given by [9]

$$\gamma_i = j\omega\sqrt{\mu_i\epsilon_i}\sqrt{1 - j\frac{\sigma_i}{\omega\epsilon_i}}. \quad (3-3)$$

The wave propagating inside the skin layer will be attenuated due to the lossy nature of the biological tissue. The electric field of a plane wave inside the homogeneous, lossy medium can be written as [9]

$$E = E_0e^{-\gamma z}, \quad (3-4)$$

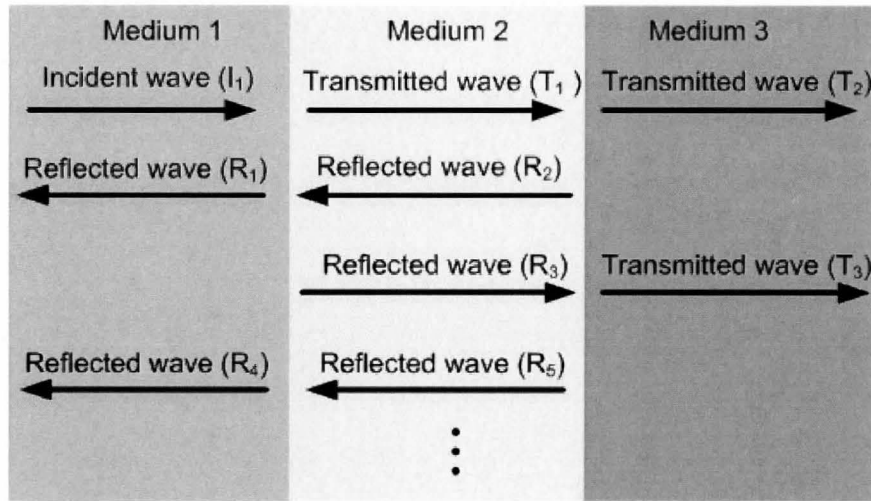


Figure 3.1. Reflection mechanism through a three-layer body model.

where z is the distance in the direction of propagation. Assuming that the incident wave I_1 is unity, then the transmitted and reflected waves can be written as follows [9]:

$$T_1 = (1 + \Gamma_{12}), \quad (3-5)$$

$$T_2 = (1 + \Gamma_{12})(1 + \Gamma_{23})e^{-\gamma z}, \quad (3-6)$$

$$T_3 = \Gamma_{12}\Gamma_{23}(1 + \Gamma_{12})(1 + \Gamma_{23})e^{-3\gamma z} \quad (3-7)$$

$$R_1 = \Gamma_{12}, \quad (3-8)$$

$$R_2 = \Gamma_{23}(1 + \Gamma_{12})e^{-2\gamma z}, \quad (3-9)$$

$$R_3 = -\Gamma_{12}\Gamma_{23}(1 + \Gamma_{12})e^{-3\gamma z}, \quad (3-10)$$

$$\text{and } R_4 = \Gamma_{23}(1 - \Gamma_{12})(1 + \Gamma_{12})e^{-2\gamma z}. \quad (3-11)$$

The total transmitted signal from air to the breast tissue is the sum of the waves propagated through the skin layer, which can be written as [9]

$$T = (1 + \Gamma_{23})(1 + \Gamma_{12})e^{-\gamma z} + \Gamma_{12}\Gamma_{23}(1 + \Gamma_{23})(1 + \Gamma_{12})e^{-3\gamma z} + \dots, \quad (3-12)$$

$$T = (1 + \Gamma_{23})(1 + \Gamma_{12})e^{-\gamma z} (1 + \Gamma_{12}\Gamma_{23})e^{-2\gamma z} + \dots, \quad (3-13)$$

$$T = \frac{(1 + \Gamma_{23})(1 + \Gamma_{12})e^{-\gamma z}}{1 + \Gamma_{12}\Gamma_{23}e^{-2\gamma z}}. \quad (3-14)$$

where T is the transmission coefficient, Γ_{12} is the electric field reflection coefficient at the interface between the first and second media and Γ_{23} is the electric field reflection coefficient at the interface between the second and third media. Now if we assume that air (medium 1) is replaced by material similar to the breast tissue, then the reflection coefficient between the first layer and the second layer will be the same as the reflection coefficient between the second layer and the third layer, which results in $\Gamma_{12} = -\Gamma_{23}$. As a result, equation (3-14) can be simplified to:

$$T = \frac{(1 - \Gamma_{12}^2)e^{-\gamma z}}{(1 - \Gamma_{12}^2)e^{-2\gamma z}}, \quad (3-15)$$

If the thickness of the skin layer is small enough to make $e^{\gamma z}$ close to 1, then the transmission coefficient will be close to unity, which implies that the reflection from this layer is insignificant [9], [26]. As shown in Figure 3.2, the dielectric properties of the

human fat are similar to the dielectric properties of the breast tissue [27], [42]. As a result, human fat can be considered as a good candidate for the coupling medium.

Next, an XFDTD simulation is performed to numerically investigate the effect of the skin interface on the transfer of energy from the coupling medium (human fat) to the breast tissue. In the XFDTD simulation, a UWB slot antenna, shown in Figure 5.1, is placed in a box ($70 \times 60 \times 81.5$) mm³, which contains three compartments. The first compartment with height of 40 mm is filled with human fat. The human fat is modeled using Debye's approximation available in the XFDTD, using the parameters given in Table 4.6 [41], [42]. The simulation environment has been meshed using a base cell size of $0.2 \times 0.2 \times 0.2$ mm³, which corresponds to accurate simulation results up to 60 GHz, and also ensures that the thickness of the skin layer in the simulation environment is represented, by more than three cells. Next, the antenna is placed in the center of the human fat-filled box. Then, a layer of skin with a thickness of 1.0 mm is placed on top of the fat layer. Finally, a layer of breast tissue with a thickness of 40 mm is placed on top of the skin layer. The antenna is excited with a 200ps Gaussian pulse and the near E-field is computed along a line located at the center of the radiating element and perpendicular to the antenna. The magnitude of the near E-field, before and after the skin layer, is shown in Figure 3.3 (a). The energy of the E-field in the breast tissue is attenuated by -1.3 dB compared to the energy of the E-field in the coupling medium. This shows that the reflection from the air-skin interface is significantly reduced by incorporating a coupling medium with electromagnetic properties close to that of human fat.

In this work, pork fat has been used as the coupling medium between the UWB antenna and the human body, given that it is not possible to use human fat as the coupling medium. The complex dielectric properties of pork fat are plotted in Figure 3.2 [27], where it is shown that the electrical properties of pork fat are similar to that of human fat and breast tissue.

The XFDTD simulation was performed to investigate the effect of the pork fat on the efficiency of the energy transfer into the human body. The setup of the XFDTD simulation is similar to the one that was conducted to find the effect of human fat on the energy transfer efficiency, with the expectation of replacing the human fat with the pork fat. The magnitude of the total E-field before and after the skin layer is plotted in Figure

3.3 (b). The energy of the E-field in the breast tissue is attenuated by -2.2 dB compared to the energy of the E-field in the pork fat, which confirms that the pork fat is a good candidate for the coupling medium. Substituting the parameters of fat at 6 GHz into equation (3.15), it is found that 0.2 dB of the transmitted energy is reflected back due to the presence of the skin interface. The reason for the discrepancy between the simulation and the theoretical results is assumption of having plane wave in the theoretical formulas but in the simulation environments the skin layer is in the near field of the antenna. Therefore, equation (3.15) can only be considered as a rough estimate of the losses due to the skin interface.

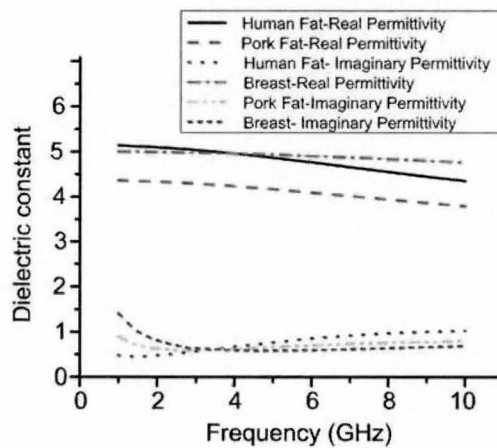


Figure 3.2. Real and imaginary permittivity of human fat and pork fat [61-65].

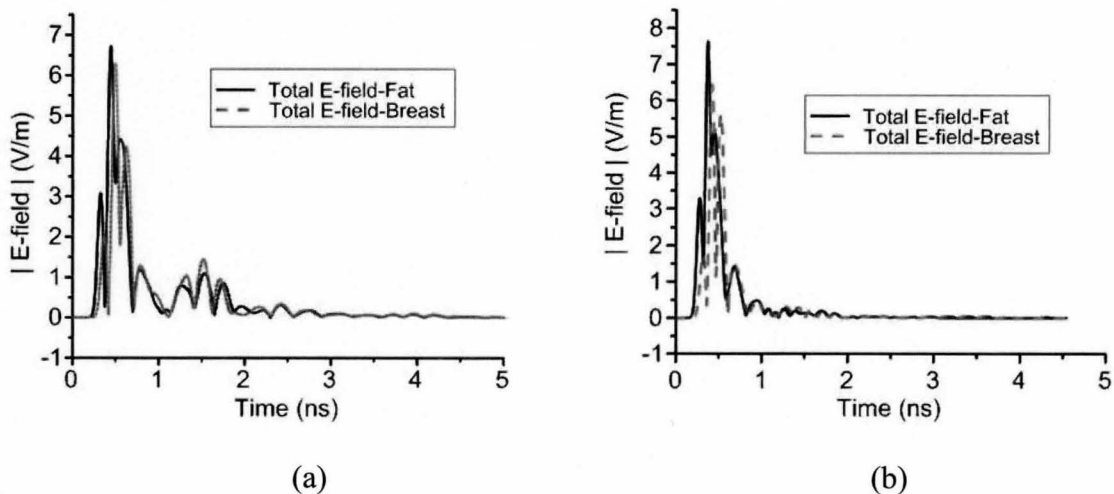


Figure 3.3. (a) Magnitude of the total E-field in the coupling medium (human fat) and breast, and (b) magnitude of the total E-field in the coupling medium (pork fat) and breast.

3.2 Design of the Coplanar Waveguide (CPW)

Coplanar lines are used to describe the group of transmission lines that includes coplanar strips, slot lines, and coplanar waveguides (CPWs). The term ‘coplanar’ implies that all signal and ground lines are on the same side of the dielectric substrate. This fact simplifies the manufacturing of the antenna with no vias required, hence reducing parasitic effects which would degrade the antenna’s performance. The performance of the CPW is comparable to microstrip lines, and it also provides well-controlled impedance levels and a proper return path for all the high-frequency currents. The structure of the CPW, shown in Figure 3.4, consists of a signal line that is sandwiched between two ground planes. The geometrical parameters of the structure, such as the width of the signal line and the gap between the single line and the ground planes, define the characteristic impedance of the CPW [28], [29].

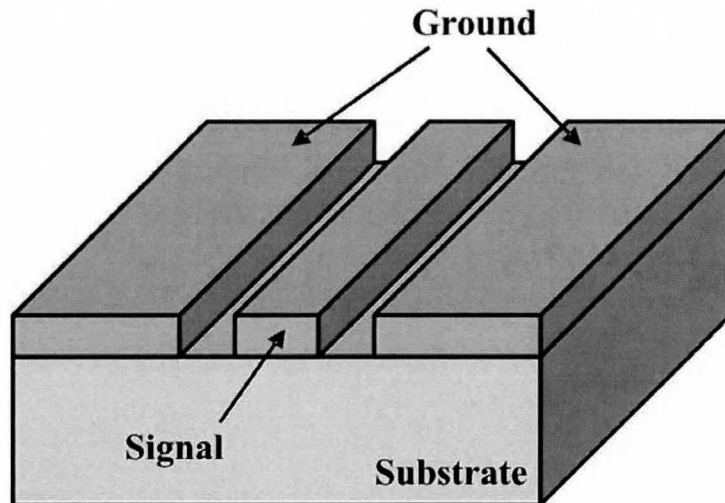


Figure 3.4. Schematic diagram of a coplanar waveguide..

3.2.1 Calculation of CPW geometrical parameters

All antennas designed in this work were fed with CPWs. The characteristic impedance of a CPW greatly affects the performance characteristic of UWB antennas. Therefore, it is necessary to design the CPW with characteristic impedance close to 50Ω to minimize its effect on the overall reflection characteristics of the antenna.

The CPW used to feed the antennas in the air medium has been designed using the LinCal tool available in Agilent ADS momentum [30]. The CPW used to feed the

antenna operating in the biological medium has been designed using a conformal mapping method [31]. The structure of CPW in the coupling medium can be modeled as a multilayer structure consisting of 5 layers of air, fat and PCB substrate (FR-4), shown in Figure 3.5.

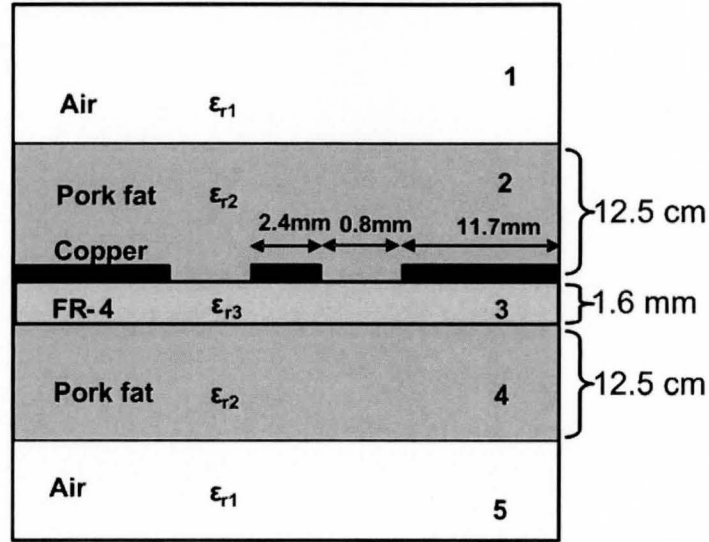


Figure 3.5. Multilayer structure used to calculate the characteristic impedance of the CPW in the coupling medium.

The design procedure for the CPW in the coupling medium is now described. Assuming that the propagation mode is a pure transverse electric and magnetic (TEM) mode, then the effective dielectric constant ϵ_{eff} , phase velocity v_{ph} and the characteristic impedance of the transmission line Z_0 can be approximated as follows [31]:

$$\epsilon_{eff} = \frac{C_{CPW}}{C_0}, \quad (3-16)$$

$$v_p = \frac{c}{\sqrt{\epsilon_{eff}}}, \quad (3-17)$$

$$Z_0 = \frac{1}{C_{CPW} v_{ph}}, \quad (3-18)$$

where C_{CPW} is the line capacitance of the CPW, C_0 is the line capacitance of the CPW when the dielectric substrate is replaced by air, and c is the speed of light which is 3×10^8 m/s in free space. From these equations (3.16-3.18), in order to calculate the characteristic impedance of a CPW, we only need to calculate the line capacitances C and C_0 .

The configurations shown in Figure 3.6 are used to calculate the line capacitances of the CPW for the antenna immersed in the coupling medium. Using the superposition of the capacitance approximation [31], the line capacitance of the CPW, C_{CPW} , can be written as:

$$C_{CPW} = C_0 + C_1 + C_2 + C_3, \quad (3-19)$$

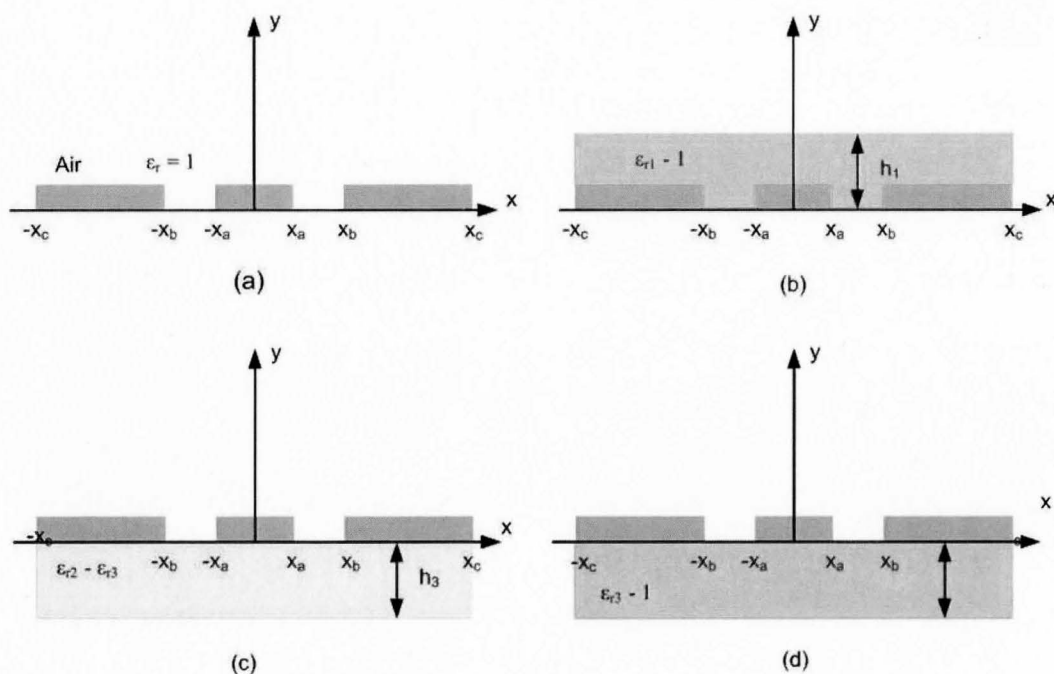


Figure 3.6. Configuration used to calculate (a) C_0 , (b) C_1 , (c) C_2 and (d) C_3 .

where C_0 , C_1 , C_2 and C_3 are the partial capacitance of each dielectric layer, and their configurations are shown in Figure 3.6. The superposition of the capacitances is exact only when all the boundaries of the dielectric are along the electric field line, which is the case for the CPW [31].

The partial capacitances of the CPW structures shown in Figure 3.6 can be calculated as follows.

1. Capacitance C_0 is the line capacitance when all the layers are replaced by air, as shown in Figure 3.6 (a). This capacitance can be found using conformal mapping as follows [31]:

$$C_0 = 4\varepsilon_0 \frac{K(k')}{K(k)}, \quad (3-20)$$

where K is complete elliptical integral of first kind, and k and k' are geometrical parameters given by [31]:

$$k = \frac{x_c}{x_b} \sqrt{\frac{x_b^2 - x_a^2}{x_c^2 - x_a^2}}, \quad (3-21)$$

$$k' = \sqrt{1 - k^2}. \quad (3-22)$$

2. Capacitance C_1 is the line capacitance due to a layer of thickness h_1 and dielectric constant $(\varepsilon_{r1}-1)$ as shown in Figure 3.6 (b). This capacitance can be found using a conformal mapping method as follows [31]:

$$C_1 = 2\varepsilon_0(\varepsilon_{r1} - 1) \frac{K(k'_1)}{K(k_1)}, \quad (3-23)$$

where

$$k_1 = \frac{\sinh\left(\frac{\pi x_c}{2h_1}\right) \sqrt{\sinh^2\left(\frac{\pi x_b}{2h_1}\right) - \sinh^2\left(\frac{\pi x_a}{2h_1}\right)}}{\sinh\left(\frac{\pi x_b}{2h_1}\right) \sqrt{\sinh^2\left(\frac{\pi x_c}{2h_1}\right) - \sinh^2\left(\frac{\pi x_a}{2h_1}\right)}}, \quad (3-24)$$

$$\text{and } k'_1 = \sqrt{1 - k_1^2}. \quad (3-25)$$

3. Capacitances C_2 and C_3 are line capacitances due to layers of thicknesses h_2 and h_3 with dielectric constants of $(\epsilon_{r2} - \epsilon_{r3})$ and $(\epsilon_{r3} - 1)$, respectively, as shown in Figure 3.6 (c) and (d), respectively. These capacitances can be found using the expression [31]:

$$C_2 = 2\epsilon_0(\epsilon_{r2} - \epsilon_{r3}) \frac{K(k'_2)}{K(k_2)}, \quad (3-26)$$

$$\text{and } C_3 = 2\epsilon_0(\epsilon_{r3} - 1) \frac{K(k'_3)}{K(k_3)}, \quad (3-27)$$

where

$$k_i = \frac{\sinh\left(\frac{\pi x_c}{2h_i}\right) \sqrt{\sinh^2\left(\frac{\pi x_b}{2h_i}\right) - \sinh^2\left(\frac{\pi x_a}{2h_i}\right)}}{\sinh\left(\frac{\pi x_b}{2h_i}\right) \sqrt{\sinh^2\left(\frac{\pi x_c}{2h_i}\right) - \sinh^2\left(\frac{\pi x_a}{2h_i}\right)}}, \quad (3-28)$$

$$\text{and } k'_i = \sqrt{1 - k_i^2}. \quad (3-29)$$

The LinCal tool and the conformal mapping method have been used to design a 50Ω CPW for antennas operating in air and the coupling medium. The physical parameters of the CPW for tapered square planar monopole (TSPM) antenna and circular tapered slot (CTS) antenna are given in Table 3.1.

Table 3.1

PHYSICAL PARAMETERS OF CPW

Antennas	x_a (mm)	x_b (mm)	x_c (mm)
TSPM Air	1.8	2.2	25
TSPM -Fat	1.4	2.3	2.8
CTS-Air	1.2	1.6	3.2
CTS-Fat	1.4	2.3	2.8

The CPW design was verified using EM simulations with Ansoft HFSS [32]. The simulated characteristic impedance versus frequency and the losses (S_{21}) between two

ends of the 12 mm long CPW is shown in Figure 3.7. From Figure 3.7 (a) and Figure 3.7 (b), we see that the real part of the characteristic impedance of all CPW is close to 50 Ω and the imaginary part is close to zero. Figure 3.7 (c) shows the losses between two ends of the CPW. The losses for the CPW operating in air are below -0.6 dB, but for the CPW operating in the coupling medium, the losses are significantly higher (-6 dB) due to the lossy nature of the coupling medium.

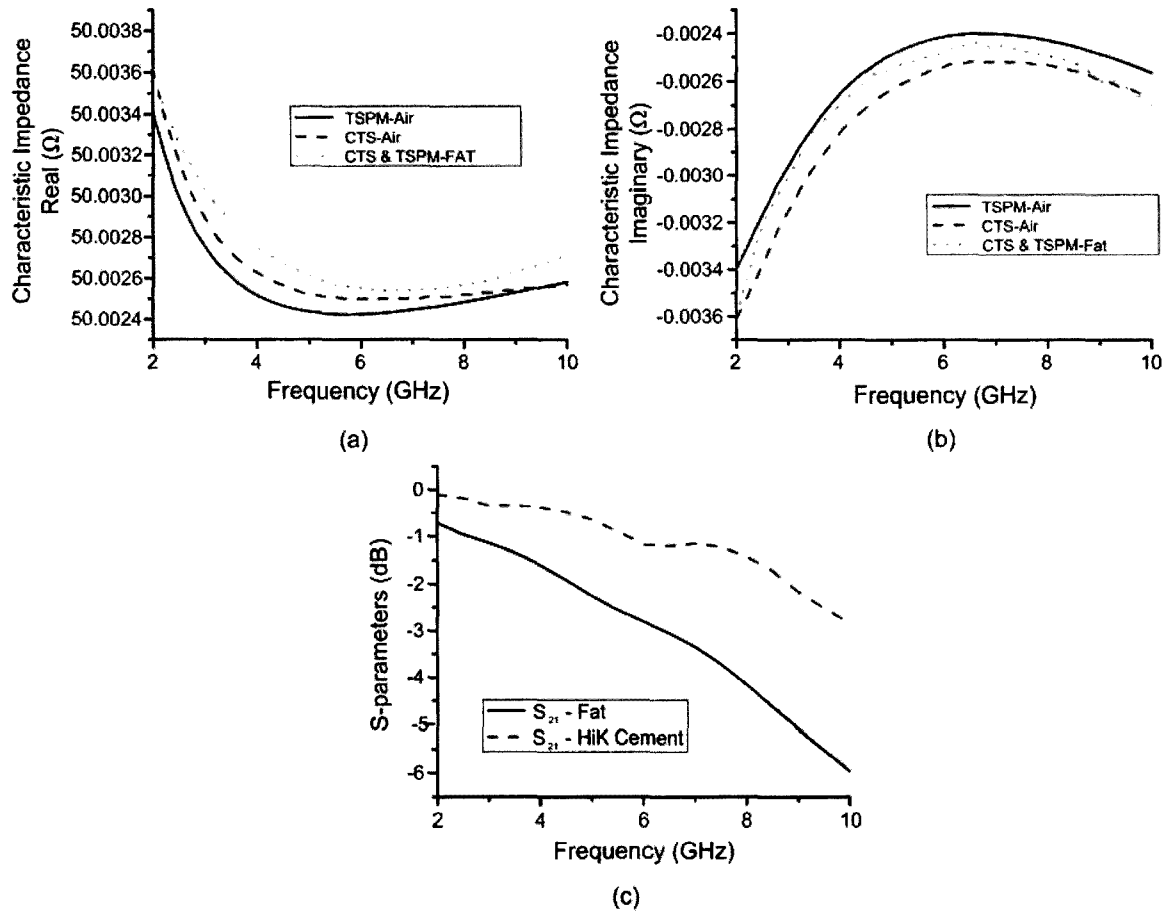


Figure 3.7. (a) Real part of the characteristic impedance, (b) imaginary part of characteristic impedance and (c) losses in the CPW.

3.3 Summary

It is found through a study of the reflection mechanisms in the human body and electromagnetic simulations that by placing the antenna in a coupling medium with electrical properties close to the tissue of interest, we can significantly reduce the amount of electromagnetic energy reflected from the skin interface, thus essentially maximizing the amount of power coupled in to the human body.

The LinCal tool and conformal mapping method have been used to design 50Ω CPW for antennas operating in air and in the coupling medium. Results of electromagnetic simulations conducted using HFSS shows that the CPW characteristic impedance is close to 50Ω , which implies that the effect of CPW on the antenna's reflection coefficient is negligible.

Chapter 4: TAPERED SQUARE PRINTED MONOPOLE ANTENNA

In this chapter we present the design procedure, simulation and measurement results of a tapered square printed monopole (TSPM) antenna for communication and imaging applications. In the design of UWB antennas, several factors must be taken into account including the physical dimensions, radiation efficiency, antenna phase, near-field and far-field radiation patterns and specific absorption rate (SAR). All antennas in this work have been fabricated on a commercially available, low cost PCB (FR-4), to reduce the overall cost of UWB imaging and communication systems.

The TSPM antenna is fed with 50Ω coplanar waveguide, which greatly simplifies the antenna's fabrication procedures and its integration with UWB transceiver systems. It is found through simulation and measurement that the proposed antenna provides an impedance bandwidth in excess of 6.5 GHz while operating in air. The effect of varying the antennas geometrical parameters on the impedance bandwidth is studied using the HFSS optimization tool [32].

The TSPM antenna has been redesigned for use in a UWB cancer detection system. The antenna is placed in a coupling medium with dielectric properties close to that of the human body, thus allowing for a reduction of the reflections from the air-skin interface. The characteristics of the antenna operating in this medium and in the proximity to the human body are investigated. It is shown experimentally that the TSPM antenna can achieve an ultra-wide bandwidth in excess of 7.5 GHz while operating in a lossy biological medium.

Finally, the performance characteristic the TSPM antenna in co-polarized and a cross-polarized arrays formation for the purpose of breast cancer detection is investigated. It is found that the energy of the co-polarized tumor response is in general 7.8 dB higher than the cross-polarized tumor response.

4.1 Wideband Planar Monopole Antennas

It is well known that the impedance bandwidth of a patch antenna, shown in Figure 4.1 (a), increases with increasing the thickness, or reducing the dielectric constant of the substrate [22]. For example, increasing the thickness of the substrate can increase the impedance bandwidth of the patch antenna by up to 10 %. On the other hand, increasing the thickness of the substrate increases the cross polarization level of the antenna and reduces the antenna's radiation efficiency due to losses in the substrate. Another difficulty in increasing the thickness of the substrate is elongation of the probe tip (p) feeding the antenna, which adds an inductive element to the input impedance of the antenna and causes difficulty in achieving a real 50Ω input impedance match at the desired frequency. One method to reduce the effective length of the probe tip is to feed the patch antenna from one side with the addition of a perpendicular ground plane. In this case, the thickness of substrate can be increased indefinitely without adding any inductive element to the input impedance of the antenna. Also, the permittivity of the substrate can be further reduced by replacing it by air, as shown in Figure 4.1 (b). If h in Figure 4.1 (b) becomes very large, then the effect of the bottom ground plane becomes insignificant and it can be removed from the structure, as shown in Figure 4.1 (c) [22]. This structure becomes similar to monopole antennas, and it is known as a planar monopole antenna.

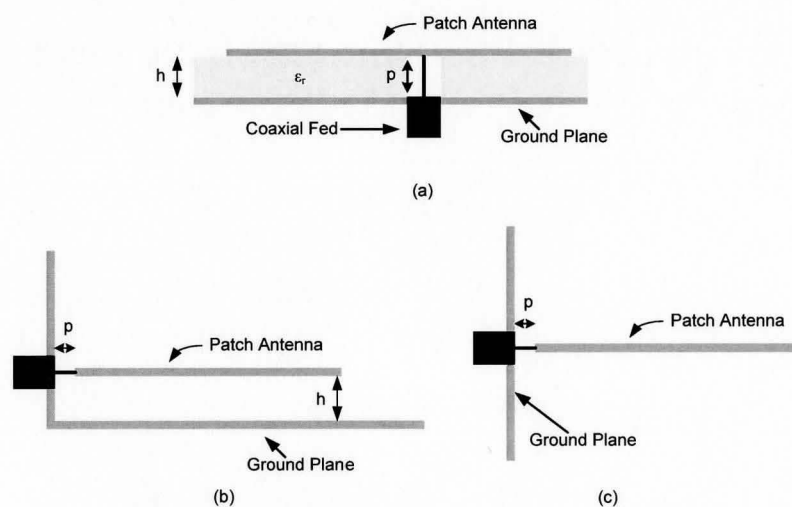


Figure 4.1. (a) Conventional patch antenna (b) monopole antenna with vertical ground plane and (c) planar monopole antenna [14].

There are various types of planar monopole antennas, including square, triangular, hexagonal, circular and elliptical monopole antennas, as shown in Figure 4.2. These antennas generally achieve very wide bandwidth, shown in Table 4.1, due to the following reasons [22].

1. Planar monopole antennas can be modeled as patch antennas on a very thick substrate with $\epsilon_r = 1$. As a result, they are expected to have a very wide bandwidth.
2. In planar monopole antennas, various higher order modes are excited, and since each mode has a wide bandwidth, the variation in the antenna's input impedance is small over a wide frequency range. This, in turn, results in a broad impedance bandwidth.
3. Monopole antennas can be modeled as a thin wire mounted on a large ground plane, with a very high Q -factor, which in turn leads to a narrow impedance bandwidth. The bandwidth of the monopole antennas increases with increasing the diameter of the wire (reducing the Q -factor). The planar monopole antennas can be modeled as a wire monopole antenna with a very large diameter, which results in a lower Q -factor, thus enabling the planar monopole antenna to achieve a very wide impedance bandwidth [23].

From the antennas shown in Figure 4.2, the disc monopole (Figure 4.2(b)) achieves the highest impedance bandwidth. This can be attributed to the fact that for the circular patch antenna, various higher order modes are characterized by roots of the Bessel function, and as a result, these modes are closely spaced in the frequency domain [22]. Given that the disc monopole antenna is in air, each of the higher order modes achieve a wider impedance bandwidth compared to the case of the circular patch antenna. The combination of closely spaced higher-order modes and wide impedance bandwidth results in small changes in the input impedance of the antenna from one resonant mode to another, which in turn implies a very wide overall impedance bandwidth [24].

The wideband monopole antennas shown in Figure 4.2 are known to have stable radiation pattern across the operating frequency band. The radiation pattern is normally monopole-like in the E -plane and nearly omnidirectional in the H -plane over the lower operating frequency band. At higher frequencies, the radiation patterns of these antennas are slightly distorted due to the increase in the electrical length of the antenna. From the

antennas shown in Figure 4.2, the SPMA and DPMA achieve the highest operating bandwidth, as shown in Table 4.1, and the lowest distortion in the radiation pattern across the band of operation [22].

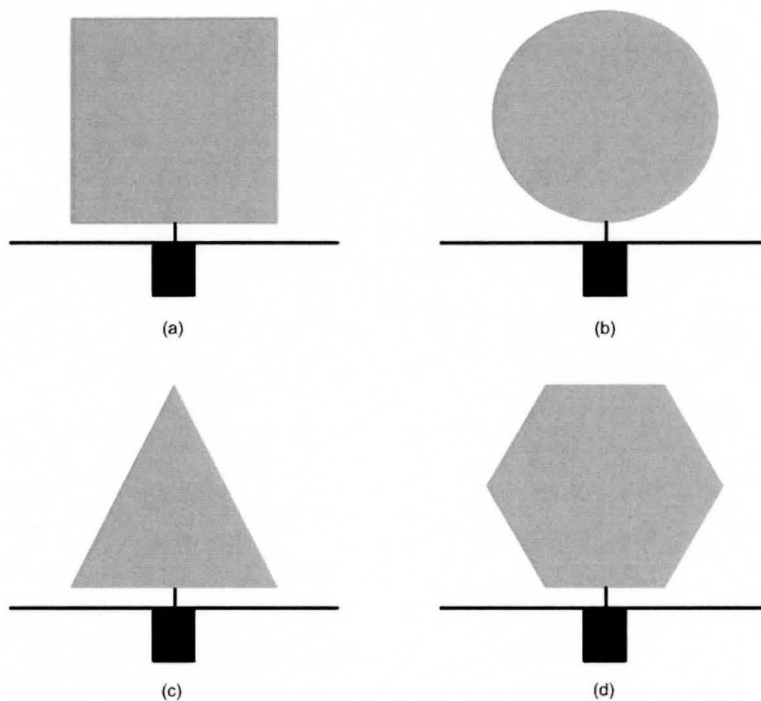


Figure 4.2. (a) Square planar monopole antenna (SPMA), (b) disc planar monopole antenna (DPMA), (c) triangular planar monopole antenna (TPMA) and (d) hexagonal planar monopole antenna (HPMA).

Table 4.1
MONOPOLE ANTENNA'S BANDWIDTH

Symbol	Bandwidth (GHz)
SPMA	2.38-5.2
DPMA	1.2-12.5
TPMA	1.5-2.9
HPMA	1.3-2.63

4.2 The Design of the Tapered Square Printed Monopole Antenna

A. Antenna Design

As mentioned in Section 4.1, planar monopole antennas can achieve a very wide impedance bandwidth while providing an acceptable radiation pattern over the entire UWB band. Although these antennas provide acceptable performances over the entire UWB band, they suffer from the fact that they have a 3D structure, which results in high cost of manufacturing and complicated feed structures. Therefore, they are not suitable for the wireless portable system, which is the major goal of UWB technology.

One solution to this problem is to print the antenna's radiating element on a PCB and place a 2D ground plane below the feed point of the antenna. In this structure, the tapering profile between the antenna's printed radiating element and the printed ground plane is similar to the tapering profile of the planar monopole antenna and its ground plane. As a result, we would expect to achieve similar performance to the planar monopole antennas, but with a 2D printed structure. Also, the antenna can be fed using a CPW or microstrip transmission line, which is easy to design and fabricate.

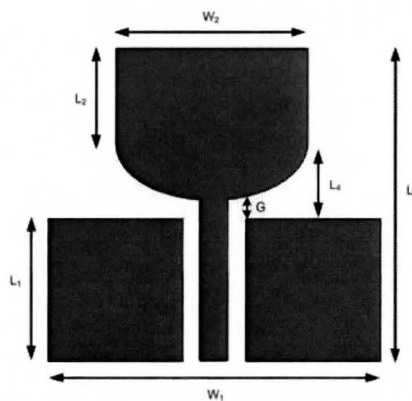


Figure 4.3. Schematic of the tapered square printed monopole (TSPM) antenna.

Keeping in mind that the broad impedance bandwidth of the circular planar monopole antenna is due to the circular tapering of the radiation element, in this work, a tapered square printed monopole (TSPM) antenna, which provides a very wide impedance bandwidth, has been designed and fabricated. Figure 4.3 shows the geometry of the proposed antenna. The antenna's radiating element is a rectangular patch and the

base of the antenna has been tapered into a semi-circle. The circular tapering of the base results in a smooth transition from one resonant mode to another. This smooth transition ensures a good impedance match in a broad frequency range [24].

B. Lowest Cut-off Frequency

To estimate the first resonant frequency of the antenna, which corresponds to the lowest cut-off frequency, the tapered square antenna is modeled as a cylindrical stub monopole antenna on an infinite ground plane. This model is valid since, in both cases, the antenna sees a large ground plane at its feed point and the distance to the ground plane from the radiating element increases as the signal moves from the feed point towards the upper edges of the antenna. The first resonant frequency of a cylindrical stub antenna on an infinite ground plane is given by [33].

$$L_2 = 0.24 \frac{\lambda L_2 / r}{1 + L_2 / r}, \text{ [m]} \quad (4-1)$$

where L_2 is the length of the antenna, r is the radius of the stub and λ is the wavelength at the first resonant frequency. The first resonant frequency of the proposed UWB antenna is approximated using equation (4-1), in which, r is replaced with the equivalent radius of the non-cylindrical structure. For a square metal element, the equivalent radius is given by [34].

$$r = L_2 / 2\pi . \quad (4-2)$$

Replacing r with its equivalent value in equation (4-1) results in:

$$L_2 = 0.207\lambda = 6.21 \times 10^7 / \sqrt{\epsilon_r} \times f_L , \quad (4-3)$$

where ϵ_r is the effective dielectric constant of the medium around the antenna and f_L is the lowest cut-off frequency of the antenna.

In the proposed design, L_2 is set to 25 mm, which corresponds to the lowest operating frequency of 2.5 GHz. The upper cut-off frequency is determined by the height

of the gap, G in Figure 4.3, between the antenna and the ground plane. The optimum value of G is obtained through HFSS parametric simulation and is described in the following section.

4.3 TSPM Antenna Optimization and Measurement Results

A. Antenna Optimization

The geometrical parameters of the antenna have been optimized for the best overall reflection coefficient (S_{11}), using the HFSS parametric optimization tool. Given that the joint optimization of the antenna parameters is computationally intensive and time consuming, in this work, each of the antenna's parameters is optimized for a given selection of other parameters.

The first parameter of the antenna that is investigated is the gap size G between the antenna and the ground plane. The HFSS simulator is used for this purpose and the antenna is simulated for gap sizes of $G = 0.2, 0.4, 0.6$ and 0.8 mm. Variation in the gap size changes the overall performance of the antenna over the operating band. It can be seen from Figure 4.4 that as the gap size increases from 0.2 mm to 0.8 mm, the reflection coefficient decreases in the lower band (3 - 5.5 GHz), but, on the other hand, it increases in the higher band (5.5 - 10 GHz). The widest bandwidth is achieved with the gap size of 0.6 mm.

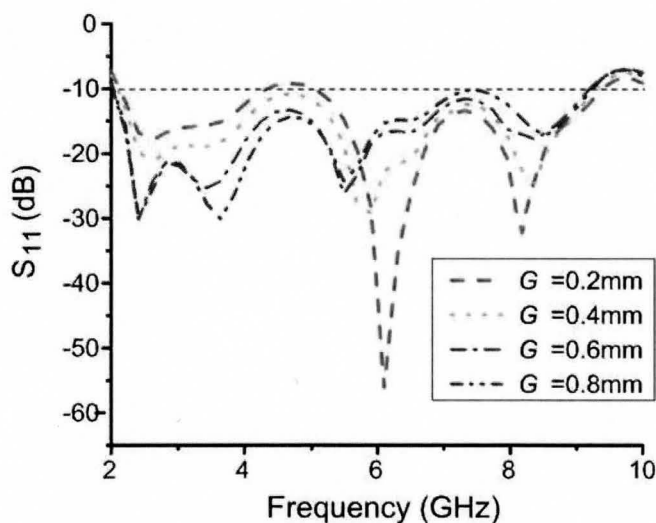


Figure 4.4. Simulated return loss for different feed gap size G , ($W_1 = 50$ mm, $W_2 = 25$ mm, $L_1 = 50$ mm, $L_2 = 25$ mm).

It is known that the bandwidth of a square planar monopole antenna on a large ground plane increases as the width of the antenna becomes smaller than the length of the antenna [35]. To investigate this effect, the width of the antenna is simulated for values of $W_2 = 33, 29, 25, 21$ and 17 mm. The return loss curves for all five cases are plotted in Figure 4.5. It can be seen that the antenna's return loss improves as W_2 changes from 33 mm to 29 mm. As W_2 becomes smaller, the antenna starts to resemble a thin monopole. As a result, the return loss deteriorates as W_2 changes from 25 mm to 17 mm. The optimum width of the antenna was found to be 29 mm.

The lengths of the antenna have been simulated for values of $L_2 = 15, 17, 19$ and 23 . As can be seen from Figure 4.6, the first resonance of the antenna shifts to a lower frequency as L_2 increases from 15 mm to 23 mm, and the highest cut-off frequency of the antenna shifts to a higher frequency, while the S_{11} degrades over the lower UWB operating band. Also, through HFSS simulation, it is found that the extension of the printed circuit board (PCB) above the antenna D , does not alter the reflection coefficient of the antenna.

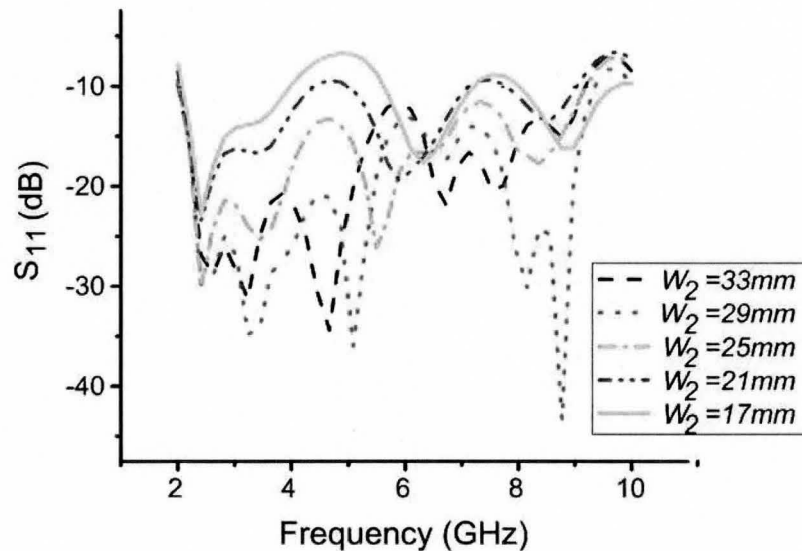


Figure 4.5. Simulated return loss for different antenna width, ($W_1 = 50$ mm, $L_1 = 50$ mm, $L_2 = 25$ mm, $G = 0.6$ mm).

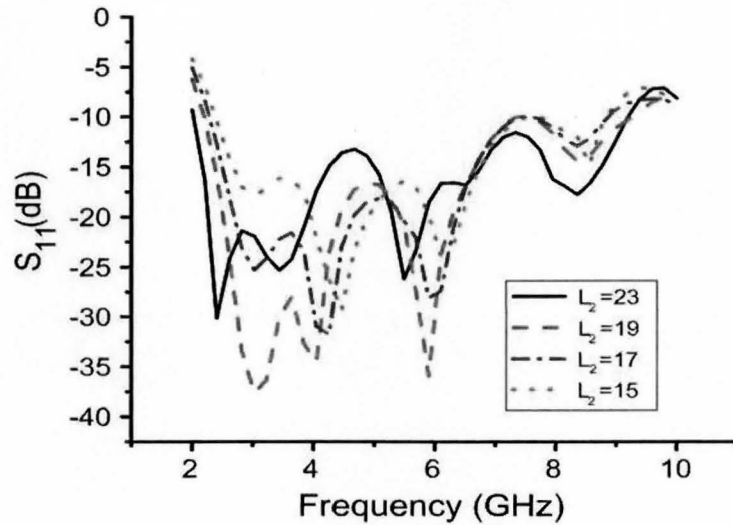


Figure 4.6 Simulated returns loss for different antenna lengths ($W_1=50$ mm, $W_2=29$ mm, $L_1=50$ mm and $G=0.6$ mm).

The final parameter of the antenna that has been optimized is the location of feed point with respect to the radiating element. Antenna geometry for a shifted feed location is shown in Figure 4.7. The antenna has been simulated for the case where the feed point is shifted by 0, 0.5 and 2 mm from the center of the radiating element. The corresponding antenna geometrical parameters are given in Table 4.2. As it can be seen from Figure 4.8, a slight shift in the feed point from the center of the antenna's radiating element improves the return loss of the antenna over the entire band of operation. But further shift in the location of the feed point degrades the return loss over the lower band of operation (3-5 GHz) and improves the return loss over the higher band of operation (6-10 GHz).

The improvement in the antenna's input matching is at the cost of an asymmetric radiation pattern over the lower operating band (3-5 GHz) and high distortion in the radiation pattern at the higher operating band (5-10 GHz). As a result, the feed point of the antenna is located at the center of the radiating element in the final prototype.

Table 4.2

Antenna Parameters for Figure 4.7

Symbol	Y_1	Y_2	X_1	X_2
0.5 mm	30	14	25	9
2 mm	30	14	25	9

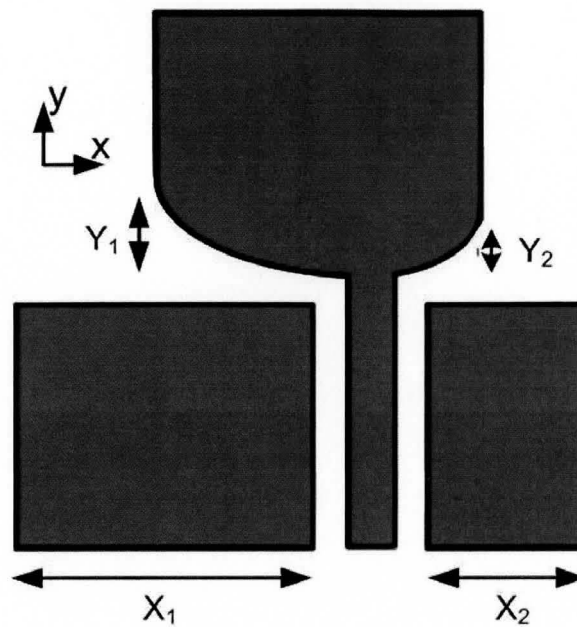


Figure 4.7. Antenna schematic, with the feed point shifted from the center.

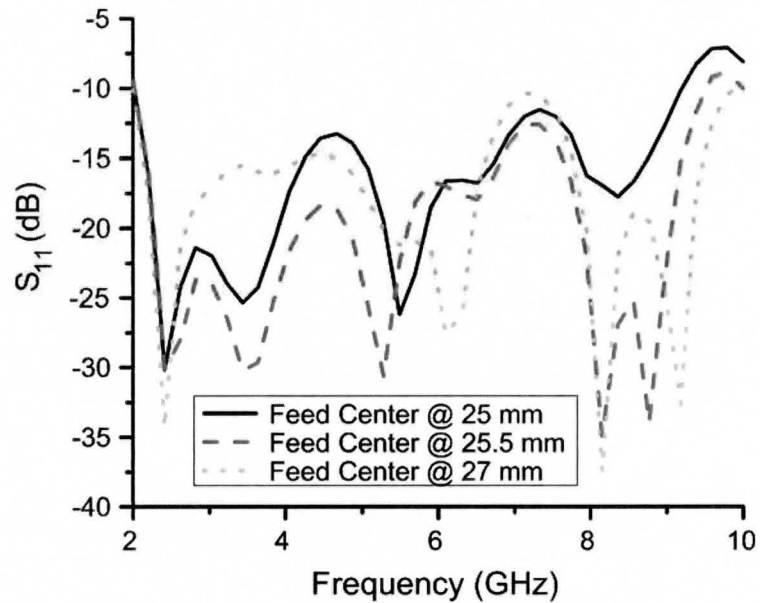


Figure 4.8. Reflection coefficient of the antenna for different feed locations.

B. Measurement Results

A prototype antenna was fabricated on a FR-4 board with $\epsilon_r = 4.4$ and $\tan\delta = 0.016$. The antenna's physical parameters are given in Table 4.3. The optimized antenna return loss is measured using an HP8720ES network analyzer, and the 83050B calibration kit has been used to calibrate the network analyzer up to the feed of the

antenna. The measured and simulated return losses are shown in Figure 4.9. The measured antenna's return loss is below -10 dB from 2.2 to 9.2 GHz and it is in good qualitative agreement with the simulation results.

The antenna's gain has been measured in an anechoic chamber. The anechoic chamber measurements are done by placing the antenna under test at one end of the chamber and measuring the antenna gain using a standard gain horn antenna placed at the other end of the chamber. The measured antenna's gain at boresight is plotted in Figure 4.10. The maximum gain of the antenna is 4.9 dB at 5.4 GHz. The 3 dB variation in the antenna gain over the operating band is acceptable for this type of printed wideband monopole antennas [48],[49],[50],[51] and [52].

Table 4.3
OPTIMIZED TSPM ANTENNA'S PARAMETERS

Symbol	W_1	W_2	L_1	L_2	L_3	L_4	G
Size (mm)	30	29	25	9	10	3	0.6

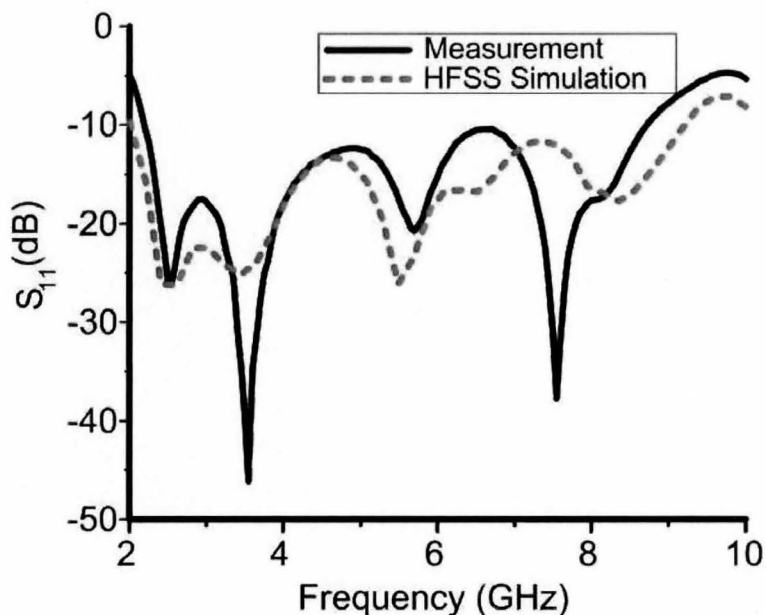


Figure 4.9. Measured and simulated reflection coefficient of the antenna.

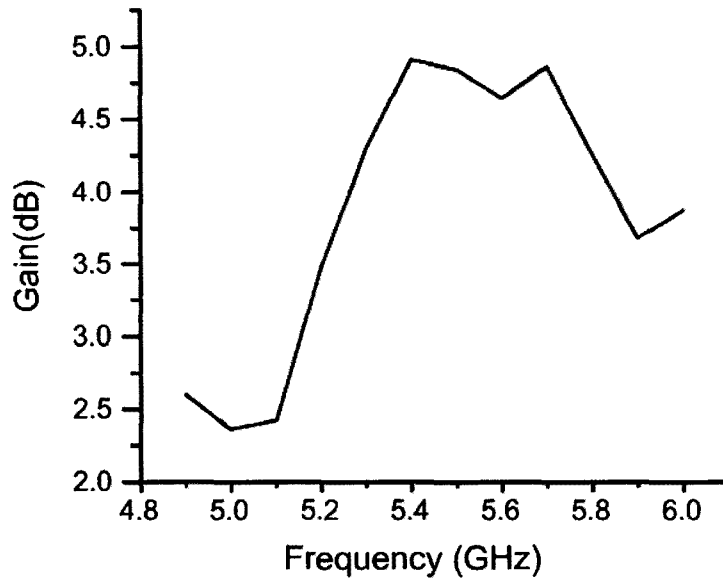


Figure 4.10. Measured antenna gain at the boresight.

4.4 TSPM Antenna Radiation Characteristic

A. Antenna Efficiency

The efficiency of the antenna, as defined in Chapter 2, is simulated in HFSS and the simulation results are plotted in Figure 4.11. The efficiency of the antenna depends mostly on the input impedance matching. Due to the degradation in the return losses and the increase in the dielectric and ohmic losses, the efficiency of the antenna decreases as the frequency increases.

B. Radiation Pattern

The far field radiation pattern of the antenna has been simulated using HFSS. The radiation pattern of the antenna has been studied in three planes XY, ZX and ZY over the entire UWB frequency range, and the results are plotted in Figure 4.12 and Figure 4.13. From 2 to 5 GHz, the radiation pattern is omni-directional in the elevation plane, and there are two major lobes in the XY and ZY planes. At 5 and 6 GHz, the radiation pattern is similar to the lower frequency band, but the magnitude of the radiation pattern decreases in the ZX and ZY planes. From 6 to 7 GHz, the maximum of the radiation pattern in the XY plane tilts towards the +y axis and the magnitude of the radiation pattern decreases in the ZX and ZY planes. At higher frequencies (8-10 GHz), there are multiple lobes in the radiation pattern, and as a result, the radiation pattern of the antenna

is distorted. The distortion in the radiation pattern of the antenna is due to an increase in electrical length of the antenna and the radiation from the CPW at these frequencies.

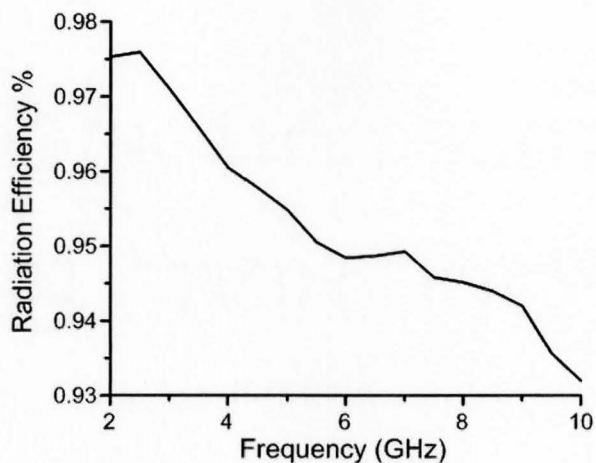


Figure 4.11. Radiation efficiency versus frequency.

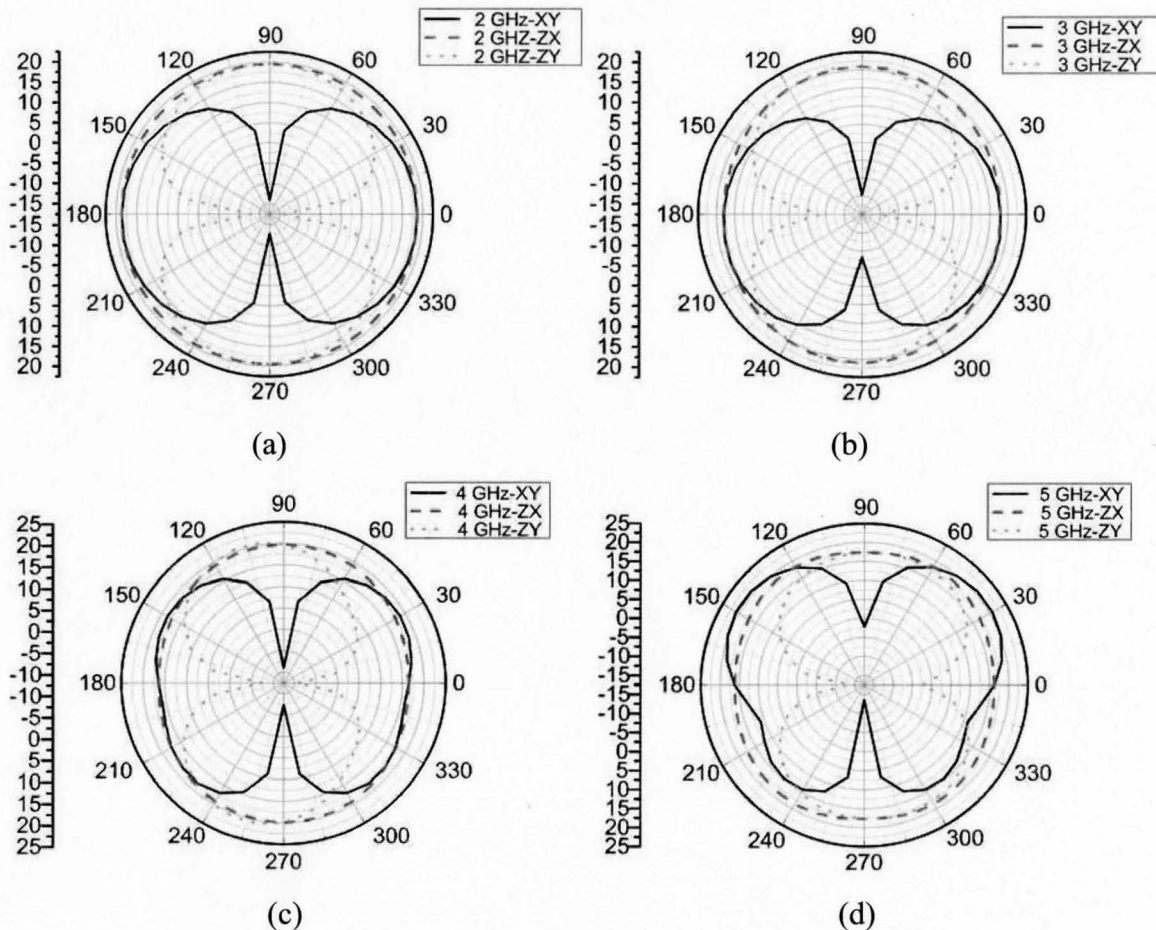


Figure 4.12 Radiation pattern of the antenna at (a) 2 GHz, (b) 3 GHz, (c) 4 GHz, and (d) 5 GHz.

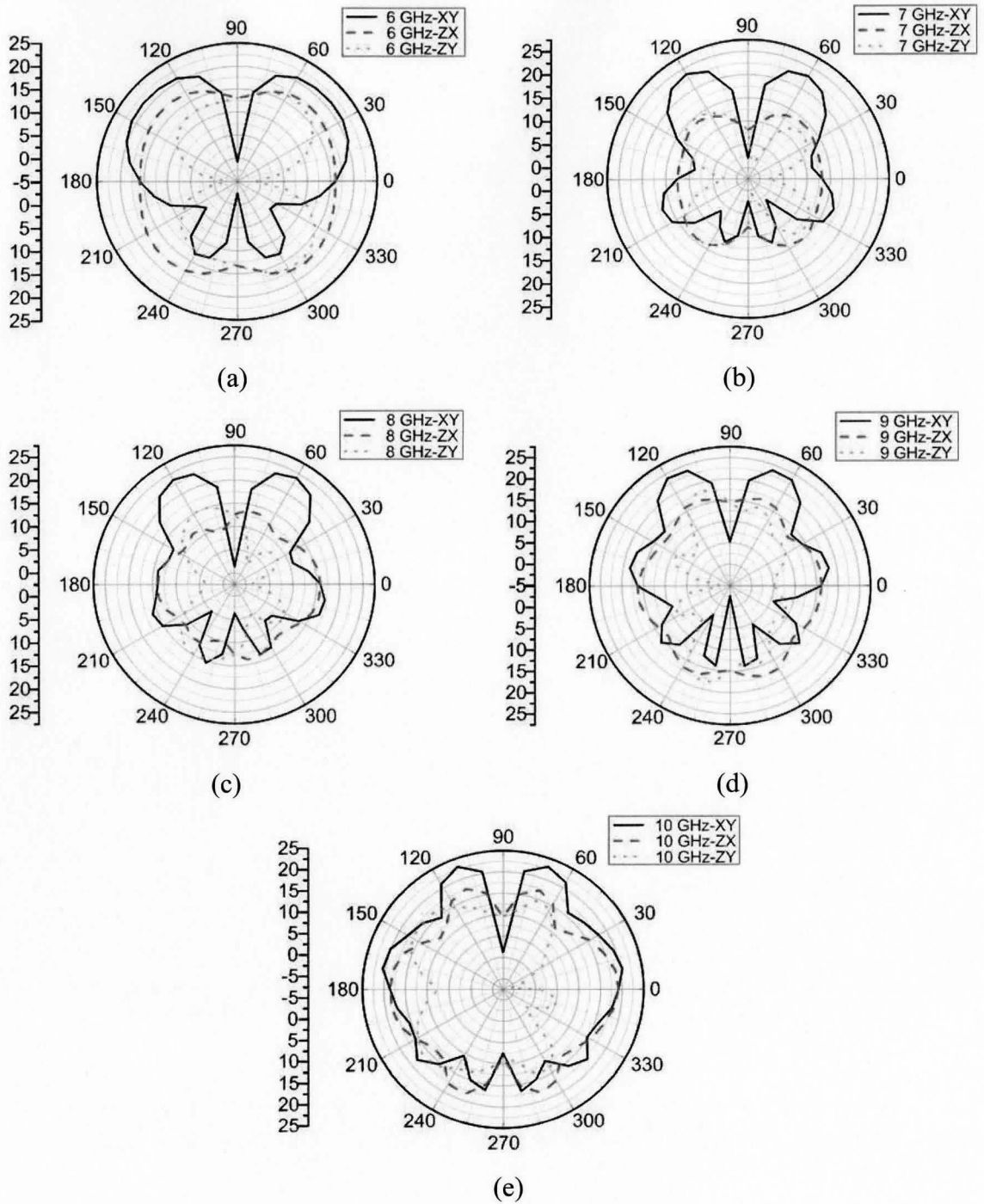
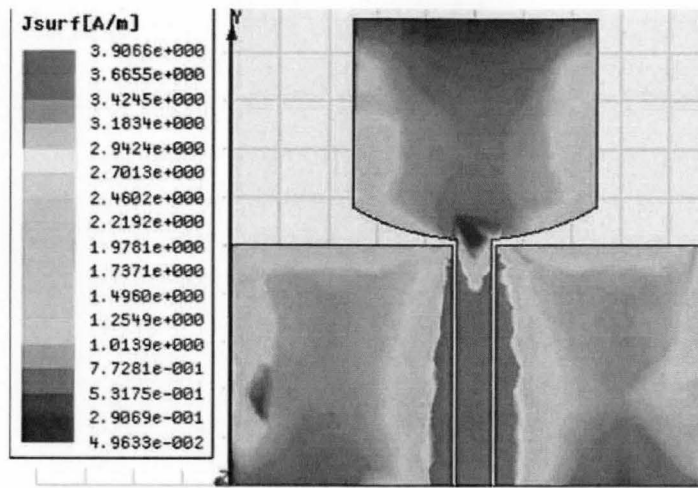


Figure 4.13. Radiation pattern of the antenna at (a) 6 GHz, (b) 7 GHz (c) 8 GHz, (d) 9 GHz, and (e) 10 GHz.

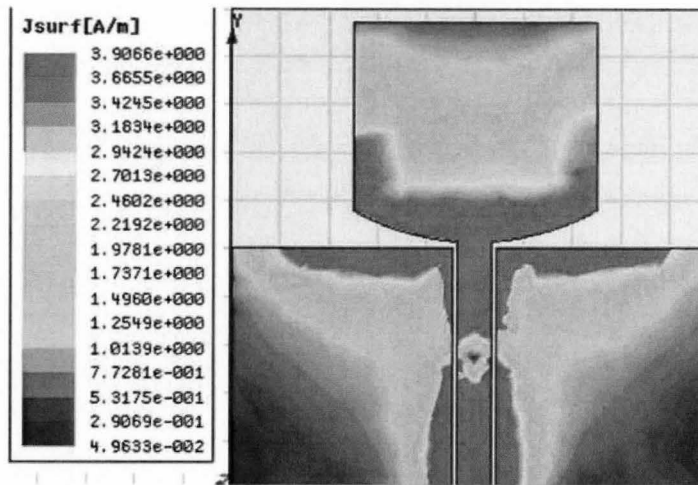
4.5 TSPM Antenna Surface Current Distribution

The magnitude of surface current distribution on the radiating element and the ground plane is plotted in Figure 4.14, Figure 4.15 and Figure 4.16. As it can be seen from the plots, and over the entire UWB operating band (3-10 GHz), the magnitude of the surface current is mostly concentrated around the edges of the ground plane and radiating element. This suggests that we can eliminate the metallization inside the ground plane and the radiating element without significantly affecting the overall performance of the antenna. To investigate this idea, two sections of the ground plane metallization of size $x_1 = 4$ mm and $y_1 = 2$ mm and one section of metallization from the radiating element of size $x_2 = 4$ mm and $y_2 = 2$ mm have been removed. The new antenna, shown in Figure 4.17 (a), is simulated in HFSS. The simulation result is plotted in Figure 4.17 (b). As expected, there is small change in the reflection coefficient and the new antenna still achieves a -10 dB return loss from 2.2 GHz to 9.8 GHz, which is the same bandwidth as the antenna with full metallization. Also, it can be seen that the changes in S_{11} in the lower frequency band (2-5 GHz) are more significant. This can be attributed to the higher surface current density at these frequencies on the sections where the metallization has been removed, compared to the upper frequency band (6-10 GHz), where the level of surface current density on the sections that the metallization has been removed is much smaller.

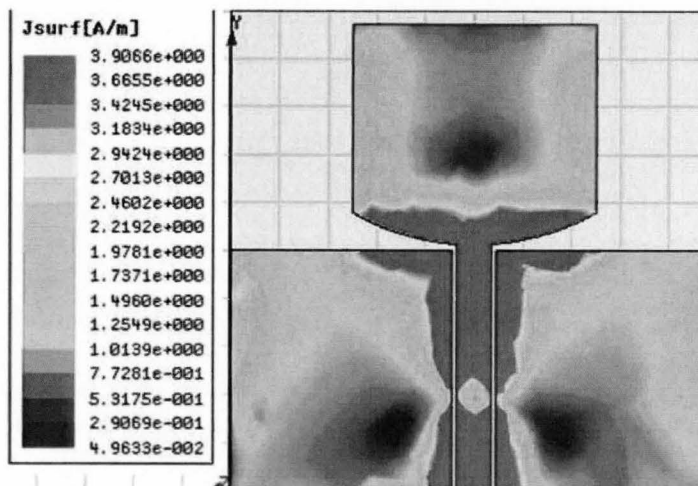
It has been noticed in [36] that a large eccentricity factor in dipoles lead to high Q-factors, which in term results in a sharp resonance with narrow bandwidth, On the other hand, small eccentricity factors lead to low Q-factors and larger bandwidth. Therefore, another explanation for the degradation in reflection coefficient is that removing part of the metallization from the radiating element effectively increases the Q-factor of the antenna, which in turn degrades the antenna's reflection coefficient.



(a)

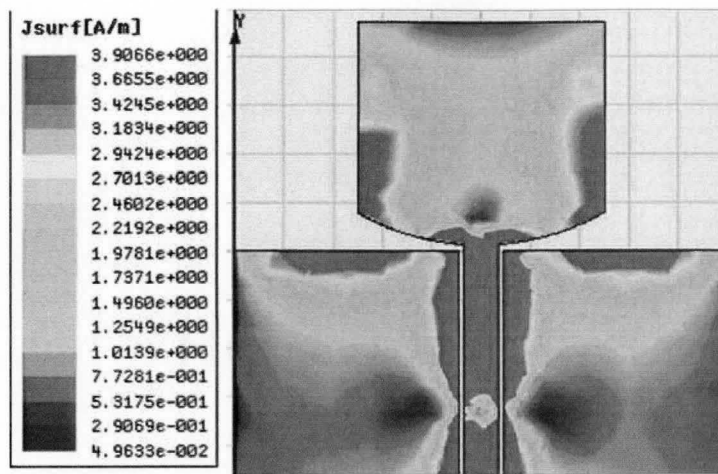


(b)

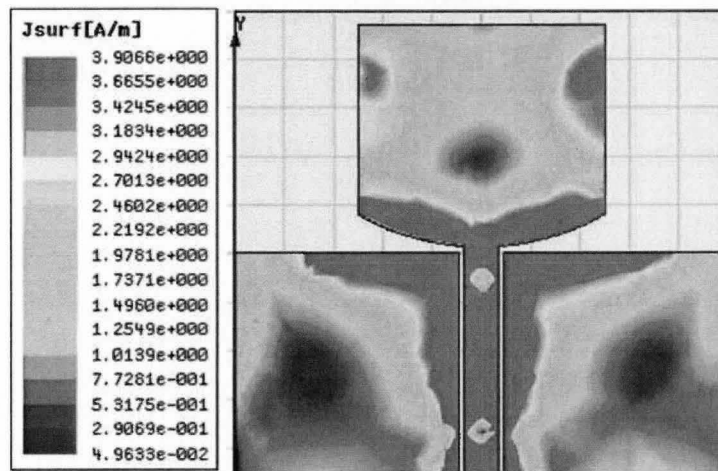


(c)

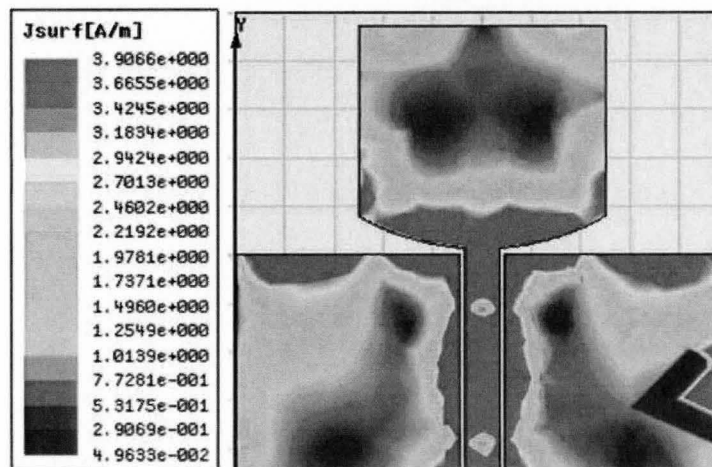
Figure 4.14. Surface current distribution at (a) 2 GHz, (b) 3 GHz, and (c) 4 GHz.



(a)

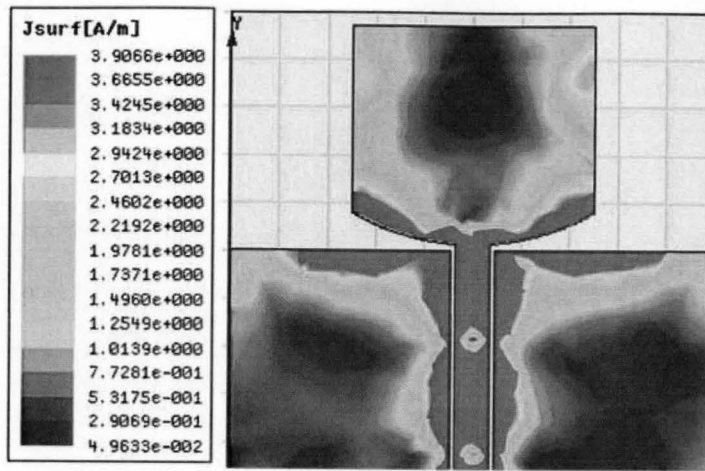


(b)

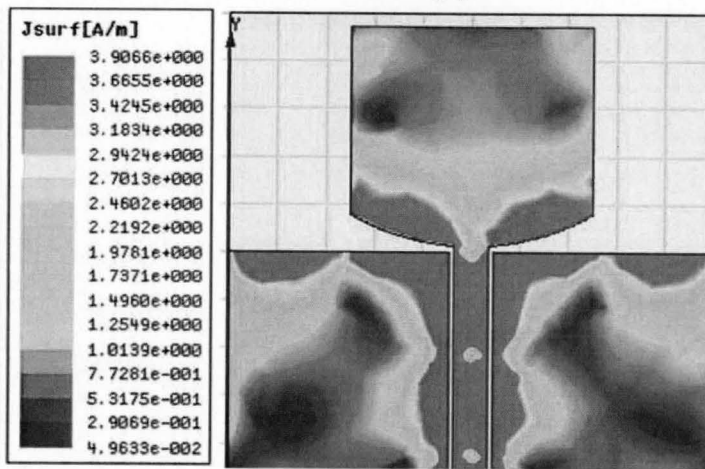


(c)

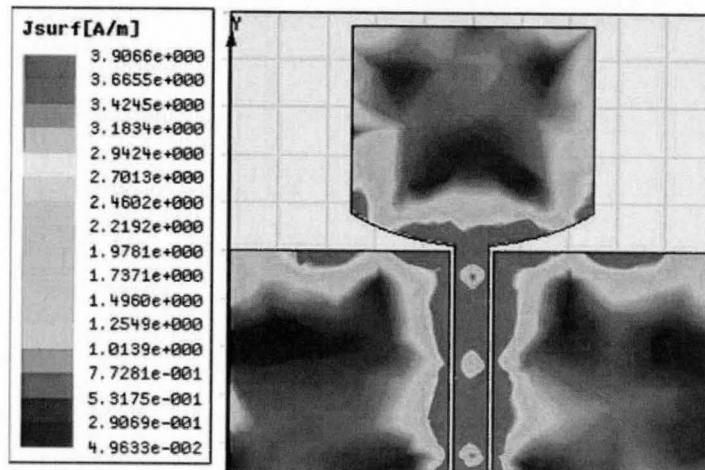
Figure 4.15. Surface current distribution at (a) 5 GHz, (b) 6 GHz, and (c) 7 GHz.



(a)

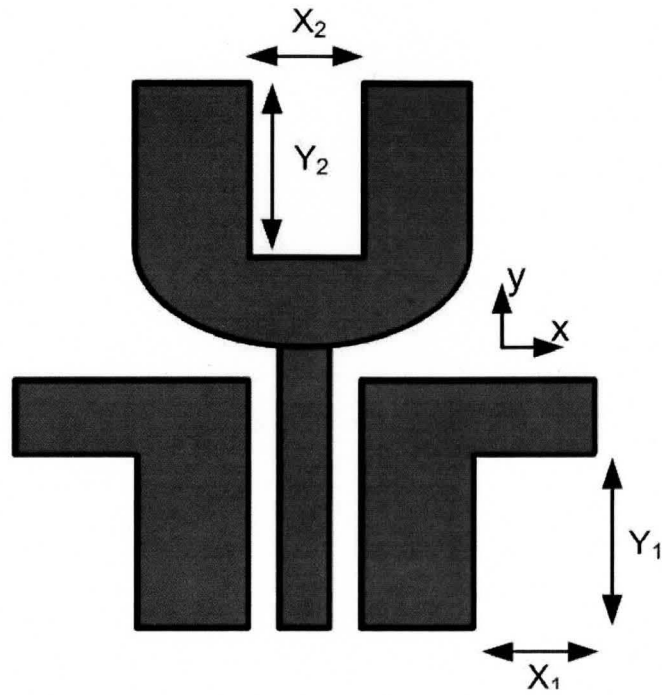


(b)

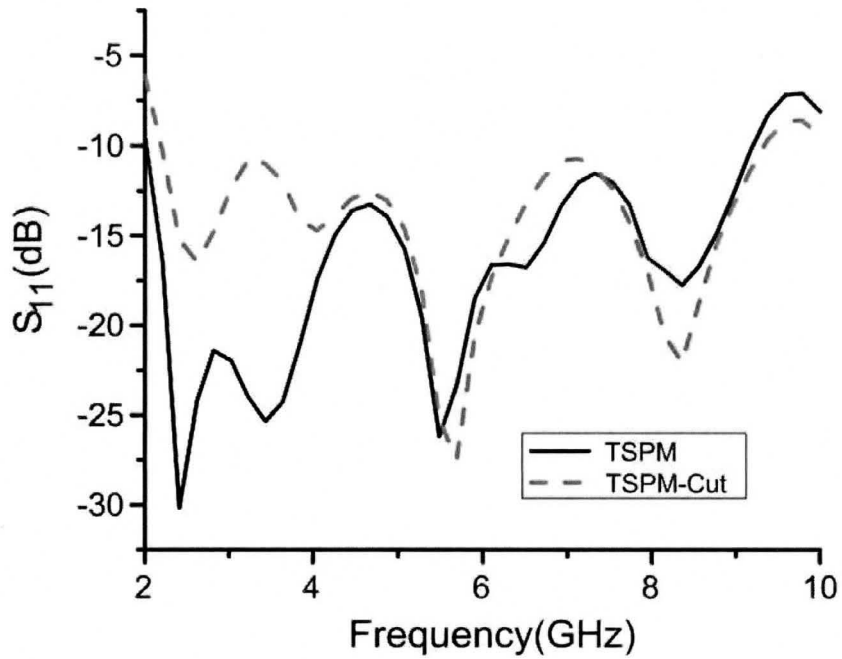


(c)

Figure 4.16. Surface current distribution at (a) 8 GHz, (b) 9 GHz, and (c) 10 GHz.



(a)



(b)

Figure 4.17. (a) Geometry of the antenna with removed metallization, and (b) simulated reflection coefficient of the antenna with full metallization (TSPM) and partial metallization (TSPM-Cut).

4.6 TSPM Antenna For Near Field Imaging

A. Antenna Design

A major challenge in the design of an antenna for UWB imaging application is the strong reflection which arises due to the present of the air-skin interface. To reduce the reflection from the air-skin interface, the antenna should be placed in a coupling medium with the similar dielectric properties to those of the human body. As discussed in Chapter 2, in this work, pork fat is chosen as the coupling medium to reduce the reflection from the air-skin interface.

To design the TSPM antenna for the UWB biomedical imaging application, we should first notice that the permittivity of pork fat is frequency dependent. But in equation (4.3), the permittivity of the material surrounding the antenna is frequency independent. As a result, to simplify the problem, it can be assumed that the permittivity of the coupling medium (pork fat) is constant over the UWB operating band and it is equal to:

$$\epsilon_r \approx \frac{\epsilon_{r_3.0GHz} + \epsilon_{r_10.0GHz}}{2}. \quad (4-4)$$

This approximation is valid since the changes in ϵ_r of the pork fat is small over the UWB operating band, as shown in Figure 3.2. The conductivity of the coupling medium has been ignored in the equation (4.3) due to the fact that the lowest operating frequency of the antenna depends on the wavelength and the effective area of the antenna. The conductivity of the surrounding medium does not have a significant effect on the wavelength at the given operating frequency or the effective area of the antenna. On the other hand, a higher conductivity of the coupling medium will significantly increase the losses in the CPW and also reduce the antenna's overall radiation efficiency. Therefore, in the final prototype, it would be preferable to use coupling media with lower conductivity to increase the antenna's overall efficiency. One candidate for such materials is the Hi-K Cement from Emerson & Cuming Microwave Products [37] with variable dielectric constant of $\epsilon_r = 3, 4, 5, 6, 7, 8, 9, 10$ and 15 and low dissipation factor of $\tan\delta = 0.01$.

To quantify the importance of the conductivity of the coupling medium on the losses in the CPW and the antenna's overall efficiency, the CPW structure has been simulated in two coupling media. The first coupling medium is pork fat, and pork fat's permittivity and conductivity have been included in the simulation using a piecewise model available in the HFSS simulator. The second coupling medium is the Hi-K cement with constant $\epsilon_r = 8$ and $\tan\delta = 0.01$. The S_{21} , which is a measure of the losses/gain between two ports, has been plotted for both structures in Figure 4.18. At lower frequencies, the losses are similar for both coupling media, but as the frequency increases, the losses in the CPW increase as well, and at 10 GHz, the losses for the pork fat coupling medium are 3.5 dB higher than the CPW in the Hi-K cement coupling medium.

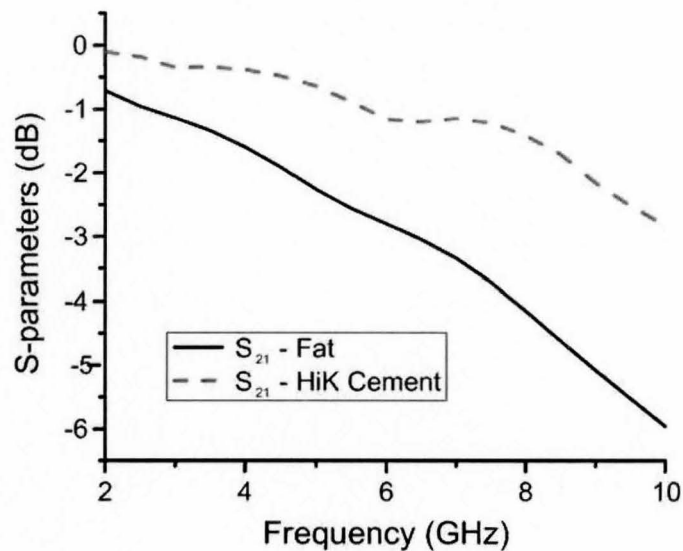


Figure 4.18. Simulated S_{21} of the CPW in pork fat and Hi-K cement.

The TSPM antenna has been redesigned to operate in the coupling medium (pork fat) and the antenna was simulated in HFSS ver.9.2 using a FR-4 substrate of thickness 1.6 mm, $\epsilon_r = 4.4$, and fed with a 50- Ω lumped gap source. The numerical domain is a $(62 \times 58 \times 33.6)$ mm³ box where the properties of the pork fat have been assigned to the box using the piecewise linear model available in HFSS. Finally, a radiation boundary was assigned to all faces of the box. The length of the antenna L_2 , in equation (4.3) has been set to 9 mm, which corresponds to the lowest cut-off frequency of 3.4 GHz. The HFSS optimization tool has been used to find the antenna's optimum parameters for

minimizing S_{11} over the operating band. The antenna's optimized parameters are given in Table 4.4.

Table 4.4
OPTIMIZED TSPM ANTENNA'S PARAMETERS FOR UWB IMAGING APPLICATIONS

Symbol	Size (mm)
W_1	30
W_2	14
L_1	25
L_2	9
L_3	10
L_4	3
G	0.6

B. Measurement and Simulation Results

The antenna was simulated in HFSS ver.9.2 using an FR-4 substrate of thickness 1.6 mm, $\epsilon_r = 4.4$, and a feed with two different feed models. The first feed model is an ideal 50- Ω lumped gap source. The second feed model is a Sub-Miniature version A (SMA) connector shown in Figure 4.19 with the geometrical parameters given in Table 4.5. As before, the numerical domain is a $(62 \times 58 \times 33.6)$ mm³ box. The properties of the pork fat have been assigned to the box using the piecewise linear model available in HFSS. Finally, a radiation boundary was assigned to all faces of the box filled with pork fat.

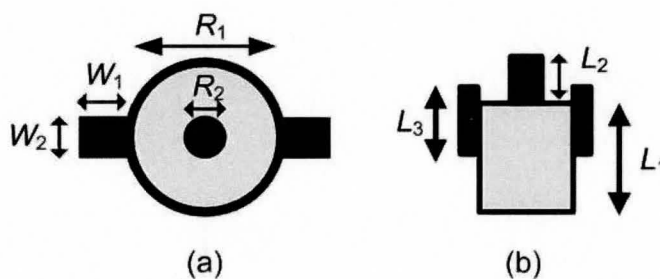


Figure 4.19. Geometry of the SMA connector feeding the antenna: (a) SMA cross section in the z-axis, (b) SMA cross section in the y-axis

TABLE 4.5

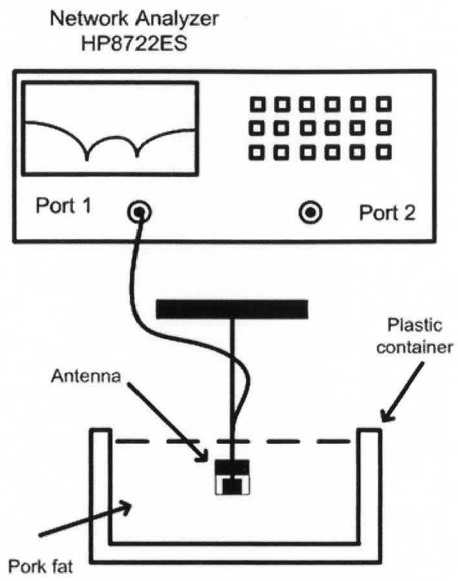
SMA CONNECTOR GEOMETRICAL PARAMETERS

<i>Symbol</i>	W_1	W_2	R_1	R_2	L_1	L_2	L_3
<i>Size (mm)</i>	1.2	3	5	1.38	4	2	3

For the measurements, a plastic container of dimensions (25×25×25) cm³ was filled with blended, congealed pork fat. Extra care was taken to ensure that the medium was free of air pockets and as homogeneous as possible to ensure the maximum possible antenna's impedance bandwidth. Before the measurement, the pork fat was stirred with a spoon to ensure mixture homogeneity and then it was patted down using a spoon in order to remove any air bubbles that were introduced by placing the pork fat inside the measurement container. For the measurement, the antenna is suspended from a stand facing downward, and the distance from the antenna to the stand is measured to be 20 cm. The antenna was then slowly submerged into the pork fat to minimize the formation of air bubbles. The distance from the surface of the pork fat to the antenna connector has been set to 5 cm.

The network analyser was calibrated to the end of the RF-cable feeding the antenna using an Agilent 85052D 3.5 mm calibration kit. The network analyser has been calibrated from 2-10 GHz, while providing 801 measurement points and averaging the result 16 times. The setup of the return loss experiment is shown in Figure 4.20.

The measured and simulated return losses of the antenna for different feed models are plotted in Figure 4.21. The measurement results indicate a return loss of less than -9.6 dB from 3.45 to 9.9 GHz. Good agreement with the simulation results was obtained. As shown in Figure 4.21, the simulation result in which the antenna is fed with the SMA connector agrees more closely with the measurement result, compared to the one with the ideal feed. On the other hand, the lowest operating frequency predicted in equation (4.3)(4-3), is closer to the simulation results with the ideal feed, due to the fact that the effect of the feed model is not included in the equation (4.3).



(a)



(b)

Figure 4.20. (a) Schematic of antenna measurement setup, and (b) the measurement environment.

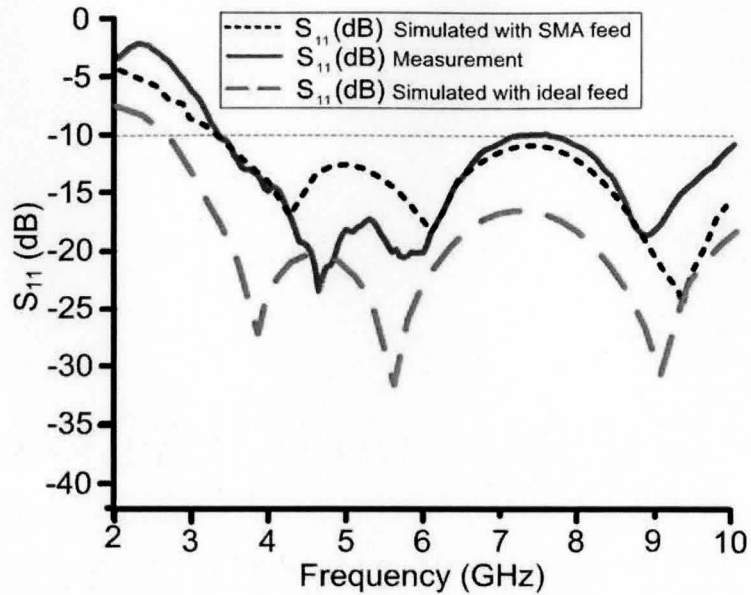


Figure 4.21. Measured and simulated return loss of the antenna in the coupling medium.

The transmission between two antennas at a separation of 6 cm was measured by placing two identical antennas facing each other, in a plastic container of dimensions of $(35 \times 35 \times 35)$ cm³, filled with blended congealed pork fat. An antenna was connected to each port of the network analyzer and S_{21} was measured. It is plotted in Figure 4.22. It is seen that the maximum transmission between the two antennas is -25 dB at 3.5 GHz. In general, the coupling between the antennas decreases with increase in the frequency, which is due to the increased loss in the coupling medium.

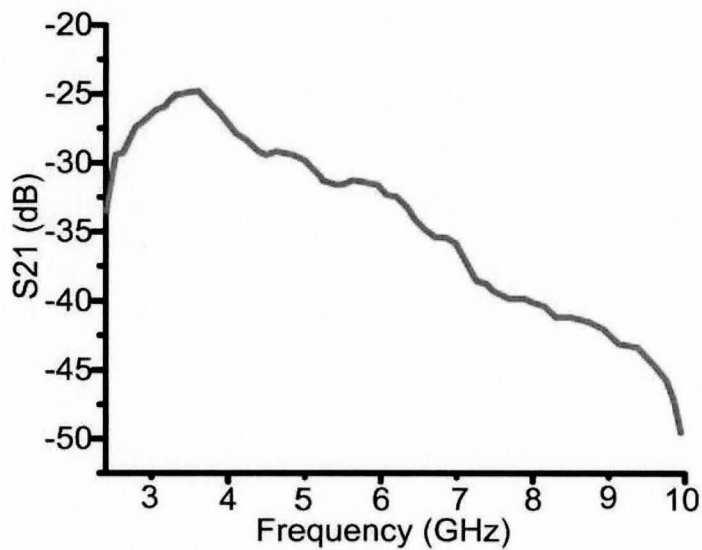


Figure 4.22. Coupling (S_{21}) between the antennas in the coupling medium.

C. Proximity Effect

Given that the antenna and the coupling medium are placed on the human body for imaging purposes, a study of the effects of the distance from the skin to the antenna has been conducted using HFSS. In this simulation, the distance D from the antenna to the skin interface has been changed from 0.5 mm to 20 mm, in increments of 5 mm. The result of the simulation is plotted in Figure 4.23. It shows that the impedance bandwidth of the antenna is not very sensitive to the separation between the antenna and the skin interface as D changes from 5 mm to 25 mm. This implies that the antenna can be placed very close to the skin interface ($D = 5$ mm), thus reducing the losses in the lossy coupling medium.

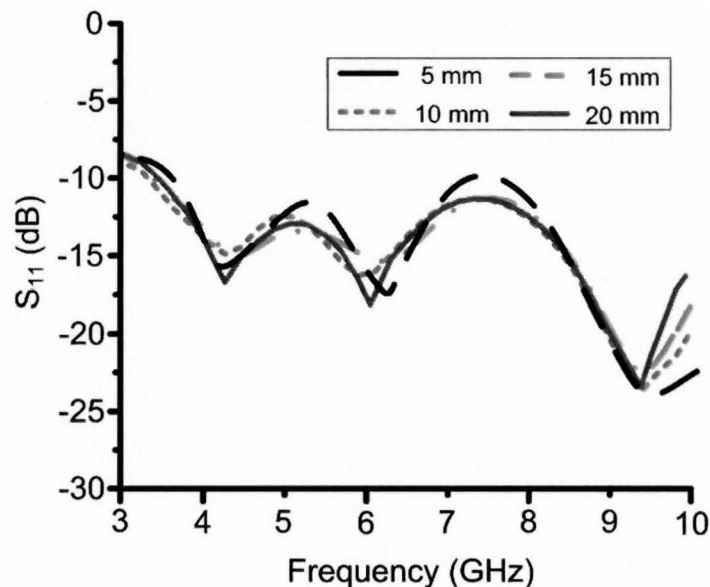


Figure 4.23. Antenna's reflection coefficient as function of distance to the skin interface.

D. Fidelity

In time domain, the performance of the antenna is evaluated by its fidelity. The fidelity is a measure of how accurately the voltage available at the antenna's terminals represents the field received by the antenna, or in the transmitting case, the fidelity shows how accurately the radiated field represents the ideal output of the antenna [38], [39].

To study the level of distortion in a radiated pulse as it propagates through the breast tissue, the antenna's fidelity is computed in a multilayer body model consisting of

the coupling medium, the skin and the breast tissue. The fidelity simulation has been performed using XFDTD [40]. For the simulation, the antenna has been placed in a box ($70 \times 60 \times 81.5$) mm³, which contains three compartments, as shown in Figure 4.24(a). The first compartment with height of 40 mm has been filled with fat. The fat material was modeled using Debye's approximation available in the XFDTD, using the parameters given in Table 4.6 [41],[42]. Next, the antenna was placed in the center of the fat-filled box. Then, a layer of skin with thickness of 1.0 mm was placed on top of the fat layer. Finally, a layer of breast tissue with the thickness of 40 mm was placed on top of the skin layer. The antenna was excited with Gaussian pulse and the derivative of the input signal was used to calculate the fidelity along a line located at the center of the radiating element and perpendicular to the antenna. The fidelity of the antenna is plotted in Figure 4.24(b). It is seen that the fidelity of the signal is maximum at a distance of 2 mm away from the antenna and it drops as the distance increases.

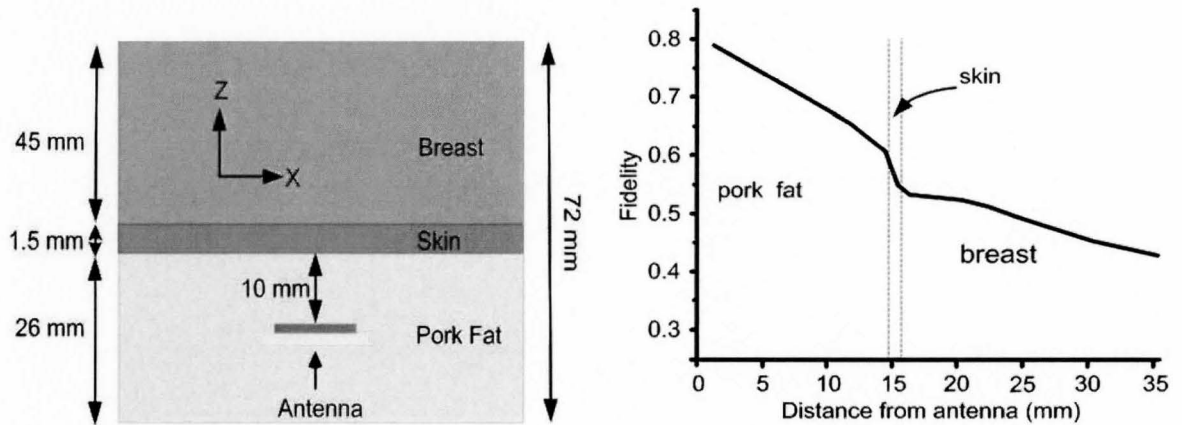


Figure 4.24. (a) Fidelity simulation setup, (b) Fidelity versus distance.

The reason for the drop in the fidelity is the frequency-dependent attenuation and the phase delay of the transmitted signal as it propagates through the biological tissue and the coupling medium. The low value of the fidelity in the breast tissue suggests that the general shape of the tumor response in time domain is not predictable. Therefore, it would be difficult to employ methods such as matched filtering to detect the presence of malignant tumors.

D. SAR Simulation

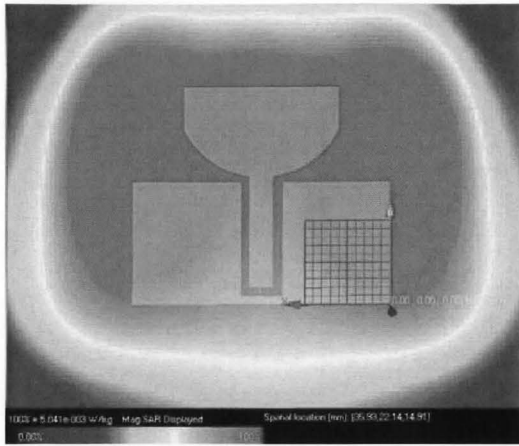
The SAR (specific absorption rate) was simulated with XFDTD, using the body model used to calculate the fidelity. Figure 4.25 plots the 1g averaged SAR distribution on the body model at the skin and breast interfaces at three frequencies of 3.5, 5.5 and 8.5 GHz for 1 mW input power. The maximum SAR values at 3.5, 5.5 and 8.5 GHz are given in Table 4.7. These values are well below the limit defined by the IEEE standard [43]. Also, the SAR distribution is fairly uniform around the radiating element, which implies that there is a small variation in the E -field at the skin and breast interfaces. The decrease in the maximum SAR is due to the increase of electromagnetic losses in the coupling medium as the frequency increases. Also, as it is seen from Figure 4.25, at higher frequencies (5.5 and 8.5 GHz), the SAR distribution is mainly concentrated around the radiating element. Therefore, for the imaging application, more power can be transmitted at higher frequencies to compensate for the losses in the coupling medium.

Table 4.6
DEBYE'S MODEL PARAMETERS

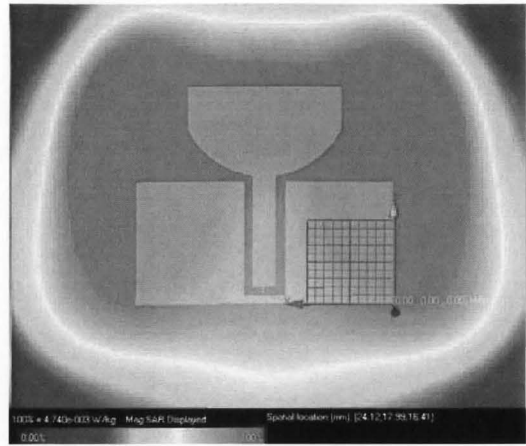
Tissue	ϵ_{∞}	ϵ_s	t_0 (ps)	σ
<i>Fat</i>	2.5	11.7	7.96	0.04
<i>Skin</i>	4	44.5	7.23	0.5
<i>Breast</i>	7	10	7	0.15

Table 4.7
TSPM Antenna's Maximum SAR

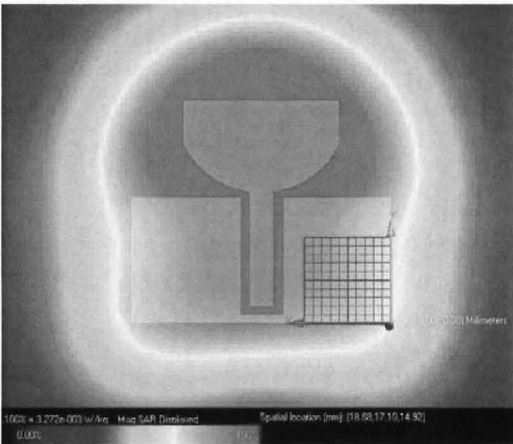
Interface	Max SAR (mW/Kg)		
	3.5GHz	5.5GHz	8.5GHz
<i>Skin</i>	5.04	3.27	2.34
<i>Breast</i>	4.74	2.37	1.43



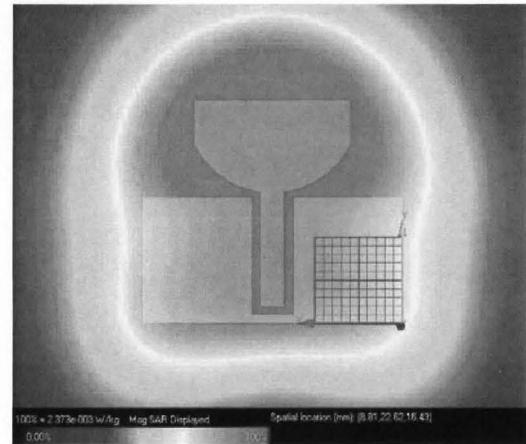
(a)



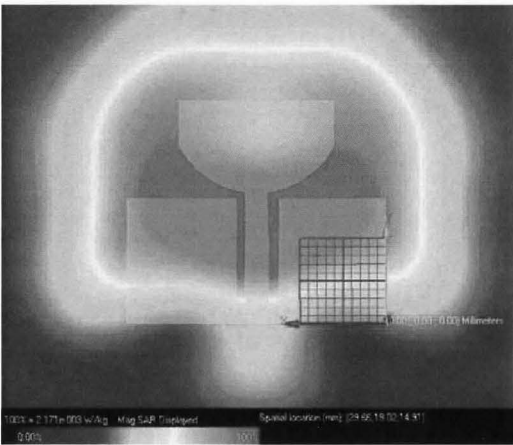
(b)



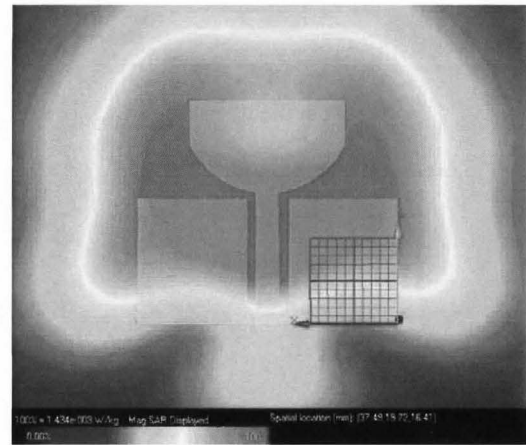
(c)



(d)



(e)



(f)

Figure 4.25. SAR distribution (a) 3.5 GHz @ skin interface, (b) 3.5 GHz @ breast interface, (c) 5.5 GHz @ skin interface, (d) 5.5 GHz @ breast interface, (e) 8.5 GHz @ skin interface, and (f) 8.5 GHz @ breast interface.

E. Near E-Field

Since the antenna is used for close range applications, the near-field radiation pattern of the antenna is an important parameter. The antenna's near-field radiation pattern has been studied at distances of $z = 2, 3$ and 4 cm from the antenna in a multilayer human body model through the HFSS simulation. For the radiation pattern simulation, the antenna has been placed in a box ($62 \times 66 \times 66.5$) mm³, similar to the one used for the fidelity simulation, but now the distance from the antenna to the skin layer is set to 10 mm. The electrical properties of breast and skin tissue have been included in the simulation using a piecewise linear model available in HFSS.

Figure 4.26 (a), (b) and (c) give the antenna's near E -field distribution inside the breast tissue at $z = 2, 3$, and 4 cm on the x -axis at three frequencies of 4.5, 6.5 and 8.5 GHz. The near E -field of the antenna at the $z = 2$ cm has a single lobe with full-width half-maximum (FWHM) beamwidths of 4.3, 4.0 and 3.7 cm at operating frequencies of 4.5, 6.5 and 8.5 GHz. The magnitude of the near E -field decreases with increasing operating frequency, which is due to the increased losses in the coupling medium and the breast tissue. At $z = 3$ cm, the near E -field pattern of the antenna maintains the same general shape as the near E -field pattern at $z = 2$ cm, with the FWHM beamwidths of 5.2, 3.75 and 3.1 cm at operating frequencies of 4.5, 6.5 and 8.5 GHz. At $z = 4$ cm, the near E -field of the antenna has two main lobe at the operating frequency of 4.5 GHz and a single lobe with FWHM of 3.68 and 2.7 cm at operating frequencies of 6.5 and 8.5 GHz.

Figure 4.26 (d), (e) and (f) plot the near E -field of the antenna along the y -axis at $z = 2, 3$, and 4 cm for operating frequencies of 4.5, 6.5 and 8.5 GHz. At 4.5 GHz, the near E -field of the antenna has two main lobes on the y -axis, which is due to the radiation from the antenna's radiating element and the SMA connector. At 6.5 GHz, the antenna's near E -field has a single lobe and it is mainly concentrated around the antenna's radiating elements. At the higher frequency band, the electrical length of the antenna increases, and, as a result, the E -field distribution is mainly concentrated around the feed of the antenna. The decrease in the magnitude of the E -field is due to the increase in the losses in the coupling medium as the operating frequency increases.

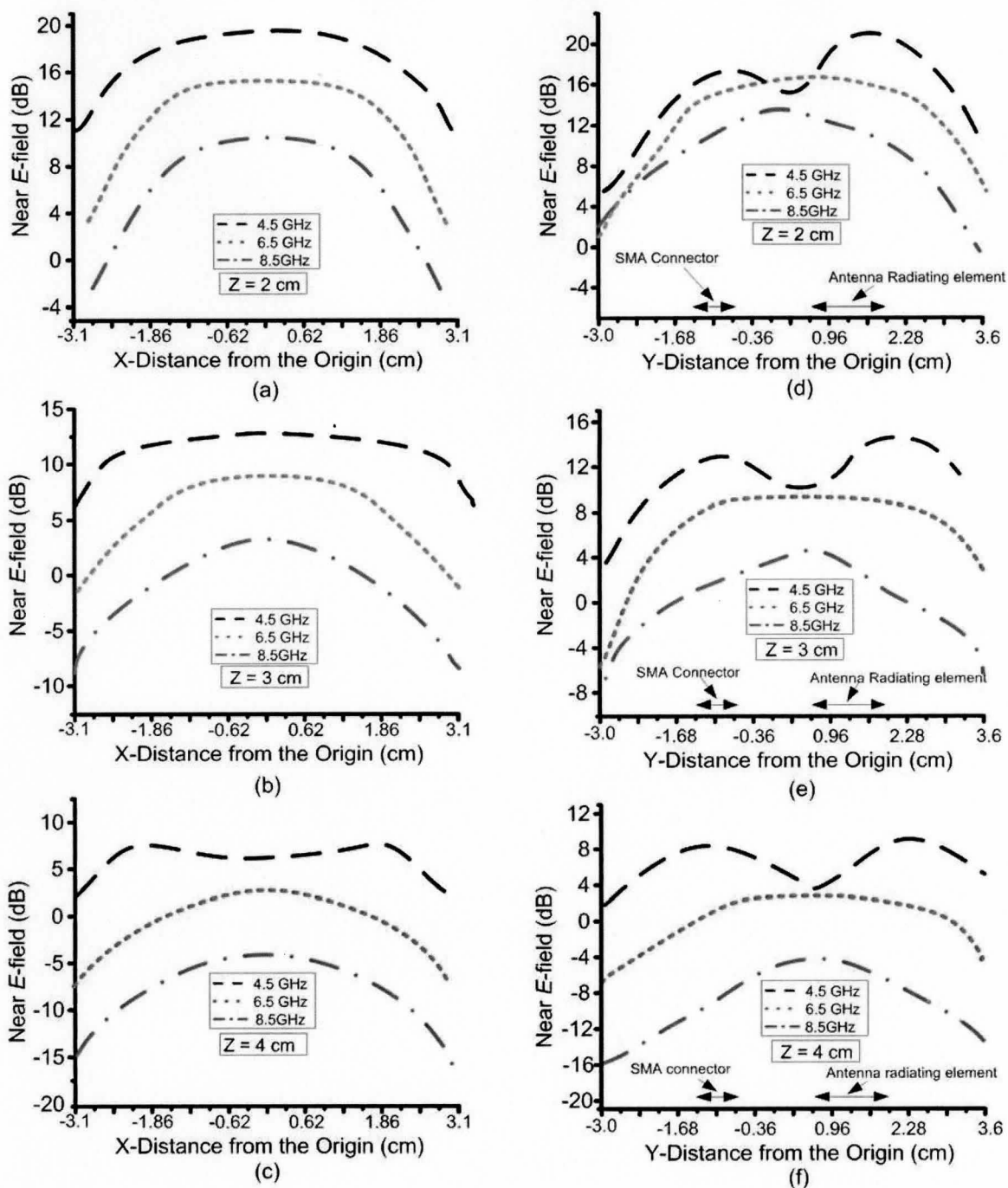


Figure 4.26. Antenna's near E -field in proximity of a multilayer body model on the x -axis at (a) $z = 2$ cm, (b) $z = 3$ cm, (c) $z = 4$ cm, and on the y -axis at (d) $z = 2$ cm, (e) $z = 3$ cm, and (f) $z = 4$ cm (refer to Figure 4.3 for the coordinate system).

4.6.1 UWB antenna array for biomedical imaging

There are two methods reported in the literature for implementing an UWB imaging system. The first method is based on frequency domain measurements [44], [53], [54] and [55]. In this method, an antenna is connected to one port of a network analyzer and a frequency sweep over the UWB band (3-10 GHz) is conducted with and without a tumor simulant in the measurement environment (phantom). Next, the changes in the reflection coefficient (S_{11}) due to the presence of the tumor are computed. Finally, the time domain reflection from the tumor is computed by taking the inverse Fourier transform of the frequency domain data. The results from this method are promising. However, due to the high cost and the high computational complexity, it is not practical to use a network analyzer to perform the frequency sweep in a commercial UWB imaging system. The second method is based on time domain measurements. In this method, two antennas are placed inside the phantom, and one antenna is connected to a wideband pulse generator and work as the transmitter, and the other antenna is connected to a wideband oscilloscope and work as the receiver. The transmitter antenna irradiates the tumor with a UWB pulse and the receiver antenna records the tumor response. The time domain method is widely used in ground penetrating radars and it has shown good potential in detecting objects buried underground [45], [56] and [57].

In this work, the time domain method is chosen for preliminary measurements, given that the UWB imaging system based on this method can be easily implemented using of-the-shelf components such as a UWB pulse generator as the transmitter and UWB LNA and high speed ADC as the receiver. To implement the UWB imaging system based on time domain measurements, a minimum of two antennas are required. Therefore, it is necessary to investigate the antenna's performance characteristic in the array formation. There are two options for the basic antennas array formation. The first is to use two antennas in a co-polarized formation, which is referring to the case when both transmitter and receiver antennas are using the same polarization. For example, if the transmitter antenna is horizontally polarized, then the receiver antenna is horizontally polarized as well. The second case of the basic antenna array element is to have two antennas in a cross-polarized formation, which refers to a configuration in which

antennas polarizations are orthogonal with respect to each other. For example, if one antenna is horizontally polarized, then the other antenna is vertically polarized.

In the next section, we will present the performance characteristics of the TSPM antenna in the coupling medium when it is operating in a co-polarized and cross-polarized array. The advantages and disadvantages of each array formation for the purpose of breast cancer detection will then be presented.

4.6.1.1 TSPM Antenna in co-polarized formation

A. Co-polarized array design

The co-polarized antenna array formation is shown in Figure 4.27. The co-polarized antenna array consists of two TSPM antennas placed side-by-side in the XY-plane. In this configuration, the direction of the E -field versus time is the same for both antennas. Therefore, we can conclude that both antennas have the same polarization which results in a co-polarized array element. In this design, the distance between the two radiating elements is set to 20 mm, to minimize the coupling between the two antennas while ensuring that sufficient scattered energy is received by the receiver antenna. Also, there is a 2 mm gap between the ground planes of the antenna to reduce the coupling between the two antennas.

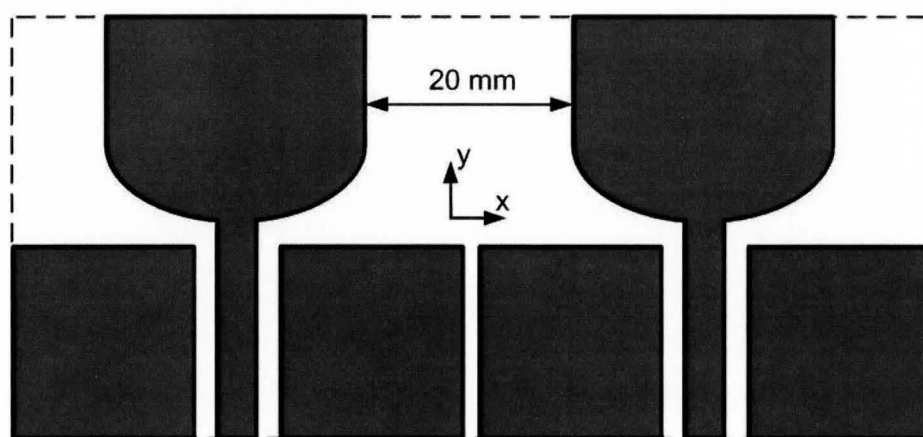


Figure 4.27. Geometry of co-polarized array element.

B. Measurement results

The S-parameters of the antenna array has been measured using a HP 8720ES network analyzer and a 85305B calibration kit has been used to calibrate the network

analyzer to the feed point of the CPW. The measured reflection coefficient of the antennas is plotted in Figure 4.28. Measurement results indicate a reflection coefficient of less than -10 dB from 3.45 to 10 GHz. The coupling between the two antennas (S_{21}) is plotted in Figure 4.29, and measurement results indicate a coupling of less than -15 dB from 2 to 10 GHz, which indicate that only 3% of the input power to the transmitter antenna is being received by the receiver antenna.

Given that the two antennas used in this array element are identical and the measurement environment is symmetrical, we would expect to have the same reflection coefficient for both antennas. But as it can be seen from Figure 4.28, S_{22} is shifted to right compared to the S_{11} . The reason for this shift can be attributed to the fact that in all calibration procedures, the position of the RF-cable is fixed and calibration is done to the open end of the RF-cables, and at the end of calibration procedure, the antenna is connected to the same end of the RF-cable without changing position of the RF-cable. But during a two-port calibration, it is required to perform a through calibration test, in which we need to connect the RF-cables together using a through test structure. Given that the RF-cables are semi-rigid, the only way to connect them together is to slightly change the position of the second RF cable. As a result of this change in the position, the final calibration result for the second cable is less accurate, so the return loss of the antennas does not match.

Another important parameter that must be taken into account is the group delay, which is the derivative of antenna's phase. If the antenna's phase is linear over the operating frequency band, then the group delay will be constant for the given band. A constant group delay implies that the delay experienced by each frequency component over the UWB operating band is a constant value, thus ensuring a low distortion in the received pulse. The phase and group delay of the antenna array element are plotted in Figure 4.30 and Figure 4.31. As it can be seen from Figure 4.30, the phase shift over the UWB frequency range is nearly linear, which resulted in near constant group delay over the UWB frequency range, as shown in Figure 4.31. The group delay between the antennas is approximately 0.5 ns, which is due to delay in the CPW, the radiating element and the path between the antennas.

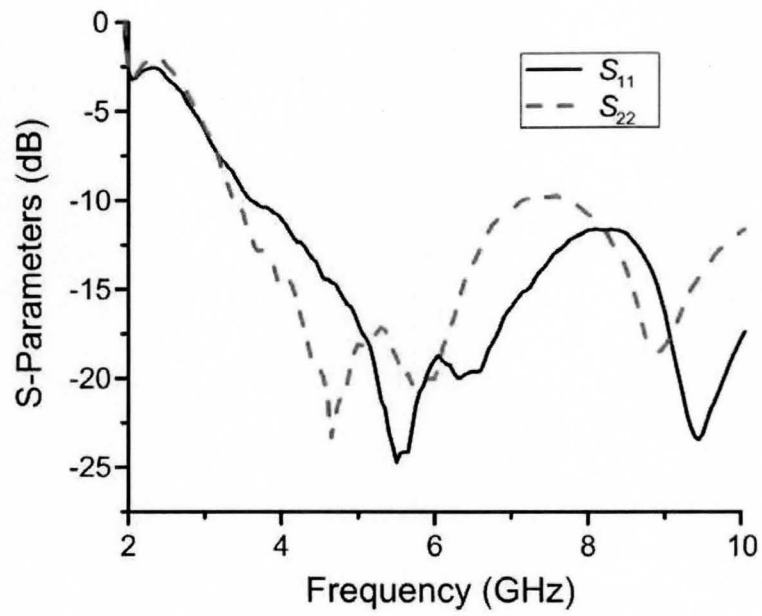


Figure 4.28. Measured reflection coefficient of the co-polarized array element.

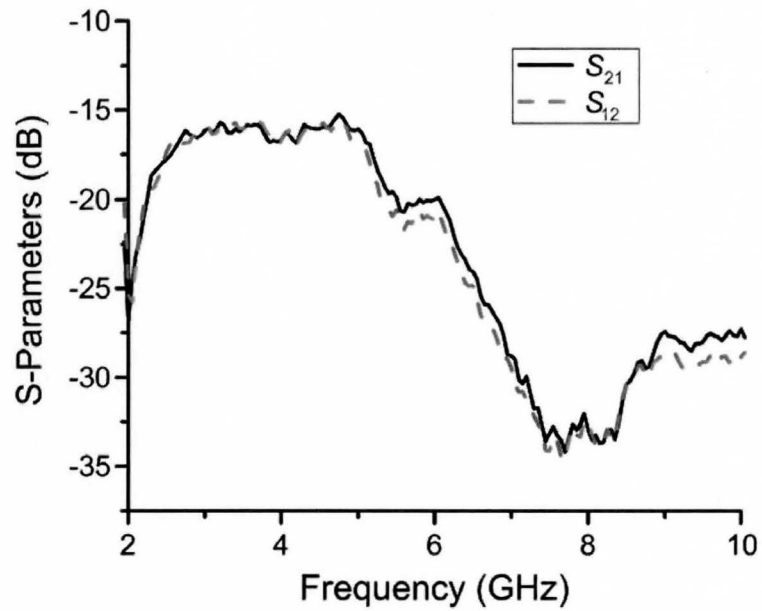


Figure 4.29. Measured coupling between two antennas of the co-polarized array element.

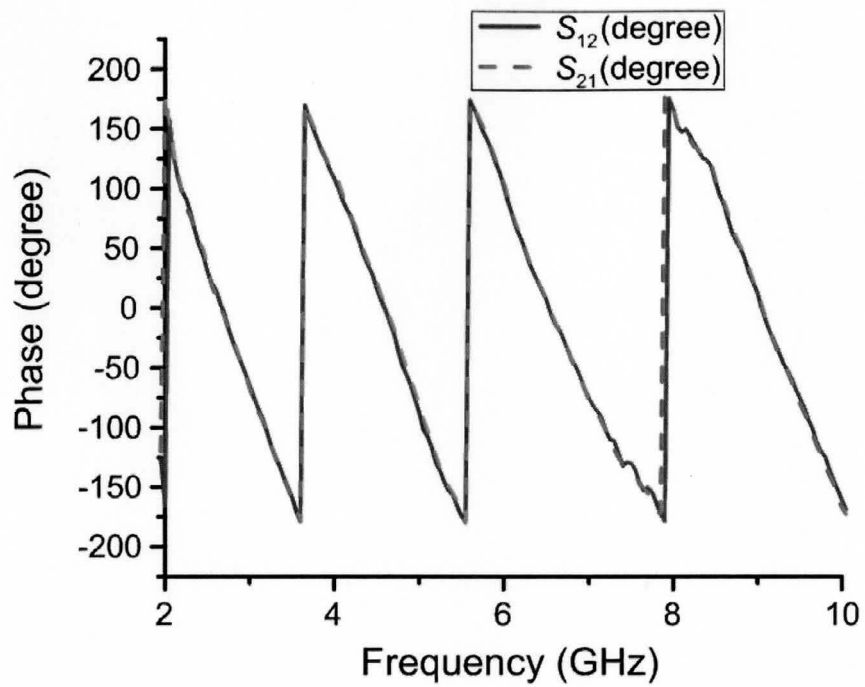


Figure 4.30. Measured phase of the co-polarized array element.

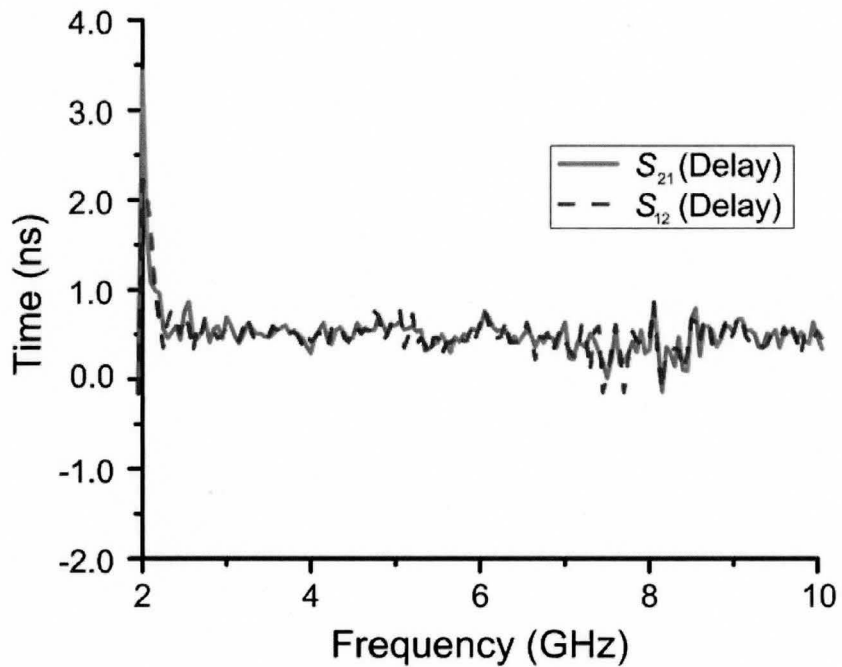


Figure 4.31. Measured group delay between two antennas of the co-polarized array element.

C. Tumor detection capabilities (simulation)

To investigate the tumor detection capabilities of the co-polarized array element for

the purpose of breast cancer detection, a set of XFDTD simulations was performed. Two sets of scenarios were investigated in this work. The first scenario is for the case when the tumor is close to the skin interface (1-4 cm) and away from the chest wall, and the second scenario is for the case when the tumor is close to the chest wall. Given that the attenuation in the E -field due to the skin interface is small, the skin layer is not included in the simulation. The schematic of the XFDTD simulation setup is shown in Figure 4.32. The procedure to find the tumor response in both scenarios is as follows:

1. The antenna array element was placed in the coupling medium, without the chest wall or the tumor. The transmitter antenna was excited with a 0.6 volt peak to peak, 200 ps Gaussian derivative pulse as shown in Figure 4.33(a). The received pulse on the receiver antenna was stored. The received pulse, plotted in Figure 4.33(b), is due to the coupling between the two antennas.
2. The cancerous tumor is mimicked by a water filled ($\epsilon_r = 81$, $\sigma = 0.01$) cylinder of radius 8 mm and height of 10 mm. The tumor is placed 3 cm from antenna. The transmitter antenna was excited with 0.6 volt peak to peak, 200 ps Gaussian derivative pulse. The received pulse on the receiver antenna was stored and it is plotted in Figure 4.33(b). The received pulse is due to the tumor response plus the coupling between the two antennas. Therefore, in order to find the tumor response, the received signal is subtracted from the response due to the coupling between two antennas. The tumor response is plotted in Figure 4.33(c).
3. Then, a 15 mm thick chest wall is added to the simulation environment. The transmitter antenna was excited with 0.6 volt peak to peak, 200 ps Gaussian derivative pulse. The received pulse on the receiver antenna was recorded and it is plotted in Figure 4.33(d). The received pulse is due to the chest wall response plus the coupling between the two antennas. Therefore, in order to find chest wall response, the received signal is subtracted from the response due to the coupling between the two antennas. The chest wall response is plotted in Figure 4.33(e).
4. Finally, a simulation with both chest wall and tumor was performed. The transmitter antenna was excited with 0.6 volt peak to peak, 200 ps Gaussian derivative pulse. The received pulse on the receiver antenna was recorded. The received pulse, plotted in

Figure 4.33(d), is due to the tumor response plus chest wall response and the coupling between the two antennas. Therefore, in order to find the tumor response we subtracted the received signal from the response only due to chest wall response plus coupling between two antennas. The tumor response is plotted in Figure 4.33(f).

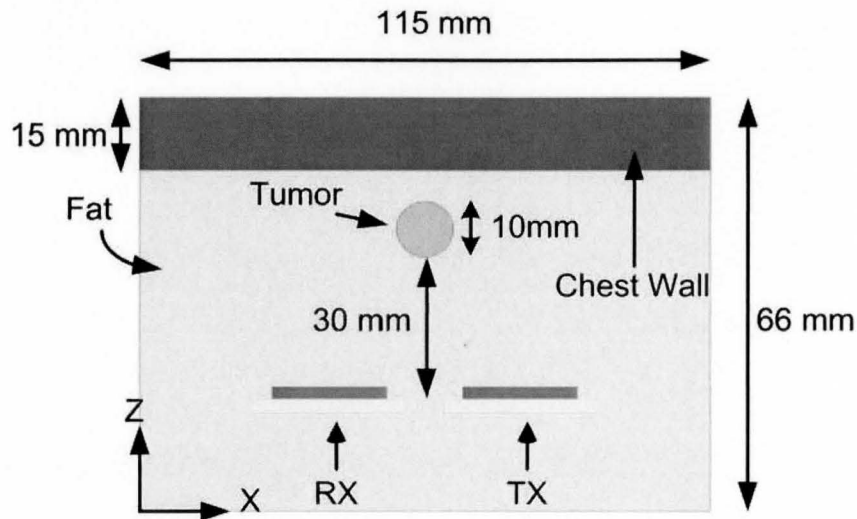


Figure 4.32. Schematic of the XFDTD simulation environment.

The energy of the received pulse from a $8 \text{ mm} \times 10 \text{ mm}$ tumor is -45 dB below the energy of the pulse that was placed at the feed of transmitter antenna. As a result, the UWB imaging system should achieve dynamic range of greater than 45 dB in order to detect tumors of this size at a depth of 3 cm . Also, it can be seen from Figure 4.33(b) that coupling between the two antennas cover the tumor response. Therefore, it can be concluded that the coupling between the two antennas should be removed from the received signal before any signal processing is done to detect the presence of malignant tumors. Given that the coupling between the two antennas is deterministic, it can be removed by subtracting the coupling between two antennas from all measured results. In the second simulation scenario, the energy of the muscle response is 12 dB higher than the energy of the tumor response. Therefore, the muscle response practically covers the tumor response. Given that the muscle response is not deterministic, we can not simply subtract it from the total response of the muscle and the tumor to determine the tumor response. Therefore, we can conclude that the co-polarized TSPM antenna array element will have limited capabilities in detecting tumors close to the chest wall.

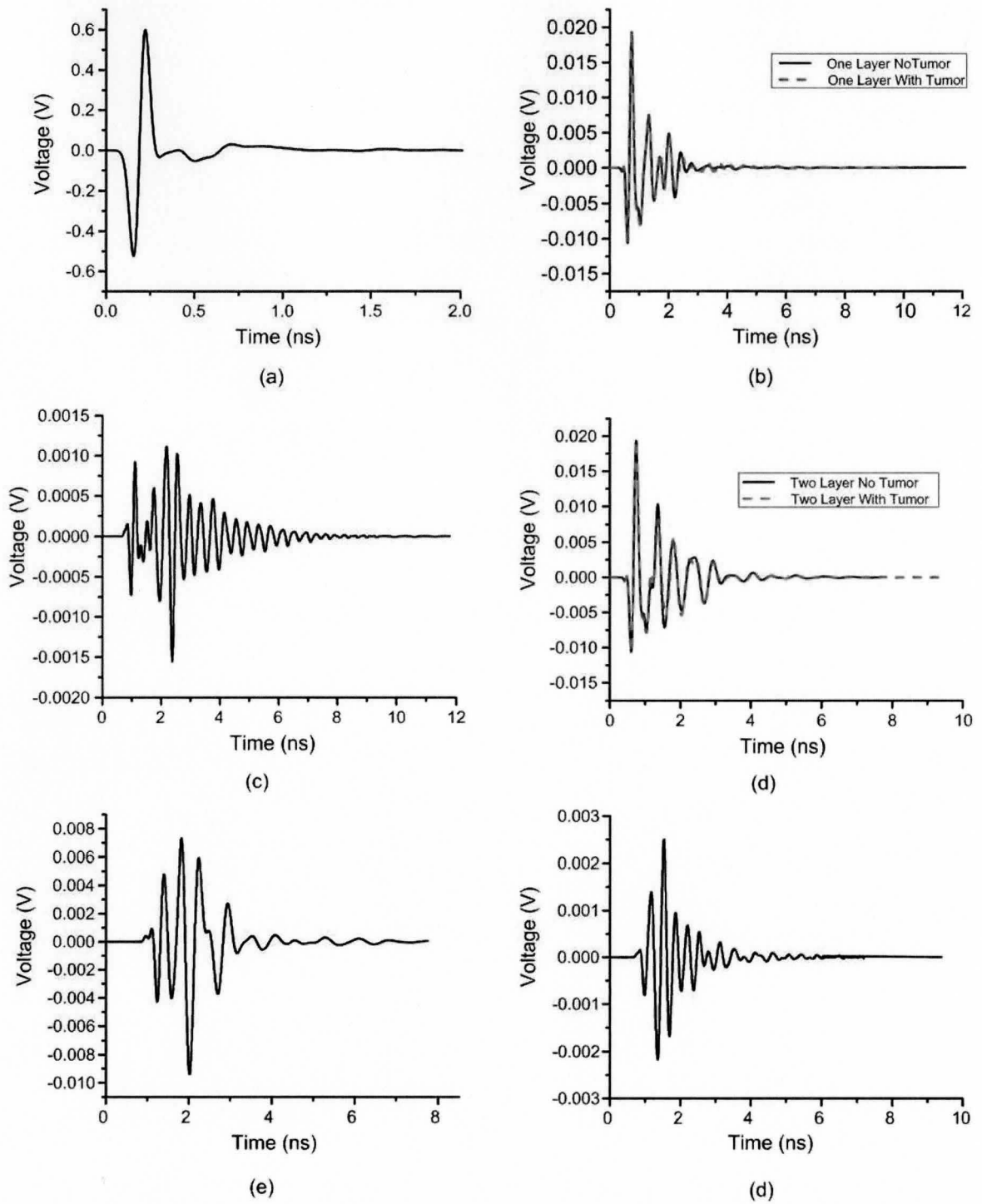


Figure 4.33, (a) Input signal to the transmitted antenna. (b) Received pulse at the receiver antenna, for one layer simulation scenario. (c) Tumor response from one layer simulation scenario. (d) Received pulse at the receiver antenna, for two layer simulation scenario. (e) received signal due to the mussel layer. (f) Tumor response from one layer simulation scenario.

4.6.1.2 TSPM Antenna in cross-polarized formation

A. Cross-polarized array design

The configuration of the cross-polarized antenna array is shown in Figure 4.34. The cross-polarized antenna array consists of two TSPM antenna placed in the XY-plane so that they are perpendicular to each other. In this configuration, the direction of the transmitter antenna's E -field is perpendicular to the direction of receiver antenna's E -field. Therefore, we can conclude that the antennas are operating with orthogonal polarization which results in cross-polarized antenna array. In this design, the distance between two radiating elements is set to 9 mm to minimize the coupling between the two antennas, while ensuring that sufficient backscattered energy is received by the receiver antenna. Also, in order to reduce the coupling between the two antennas, there is a 4 mm by 2 mm gap between ground planes of one antenna and the radiation element of the other antenna.

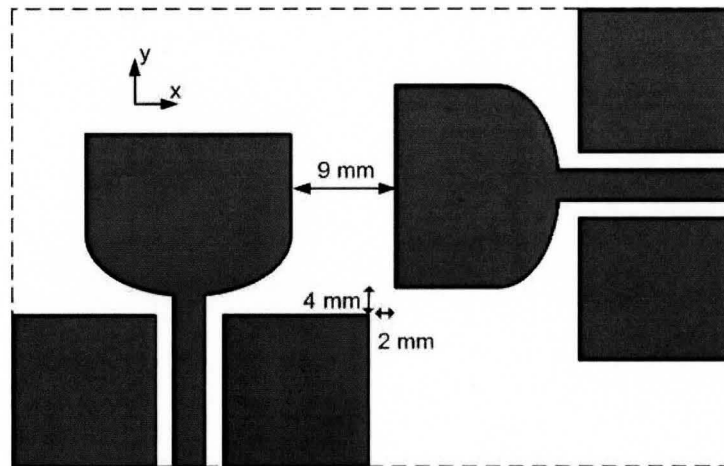


Figure 4.34. Geometry of co-polarized array element.

B. Measurement results

The measurement setup of the cross-polarized antenna array, is similar to the one used to measure the s-parameters of the co-polarized antenna array shown in Figure 4.20. The measured reflection coefficient of the antennas is plotted in Figure 4.35. The measured reflection coefficient of each array element is less than -10 dB from 3.45 to 10 GHz, and the measured coupling between the two antennas (S_{21}), plotted in Figure 4.36,

and is less than -20 dB from 2 to 10 GHz, indicating that only 0.1 % of the input power to the transmitter antenna is being received by the receiver antenna. The phase and the group delay of the antenna array element are plotted in Figure 4.37 and Figure 4.38. As shown in the Figure 4.37, the phase shift over the UWB frequency range is linear, which resulted in a near constant group delay over the UWB frequency range as shown in Figure 4.38. The group delay between the antennas is approximately 0.5 ns, which is due to the delay in the CPW, radiation element and the path between the antennas.

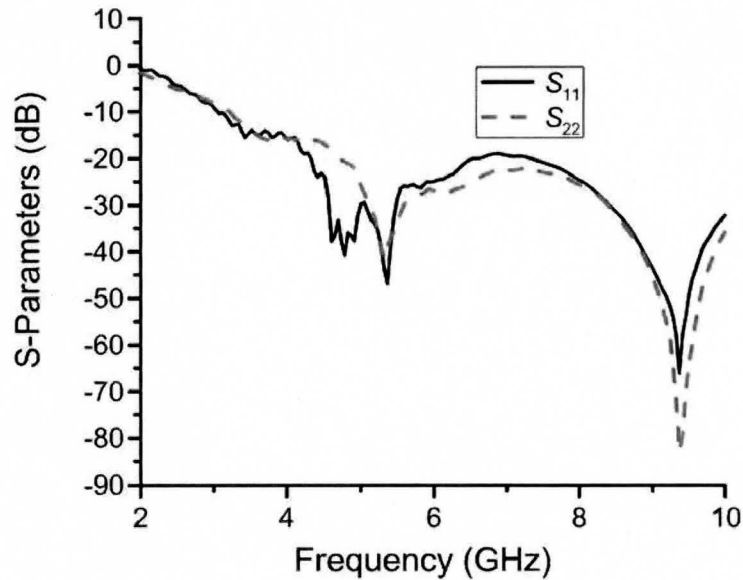


Figure 4.35. Measured reflection coefficient of the cross-polarized array element.

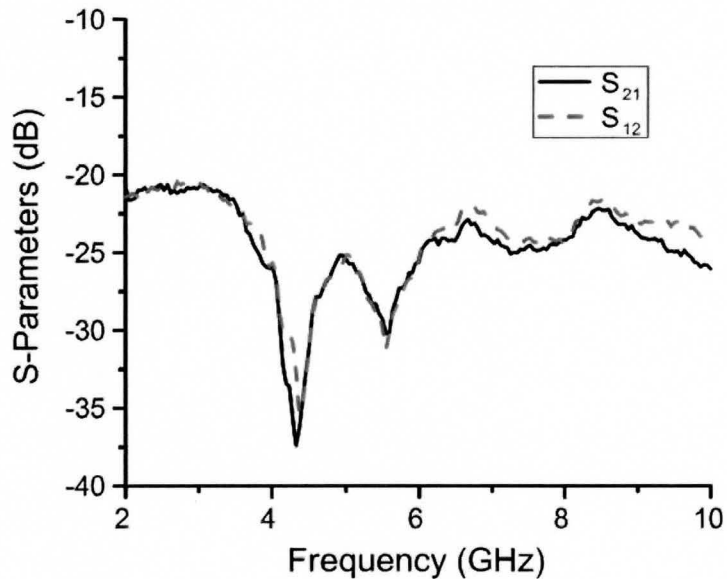


Figure 4.36. Measured coupling between the cross-polarized array elements.

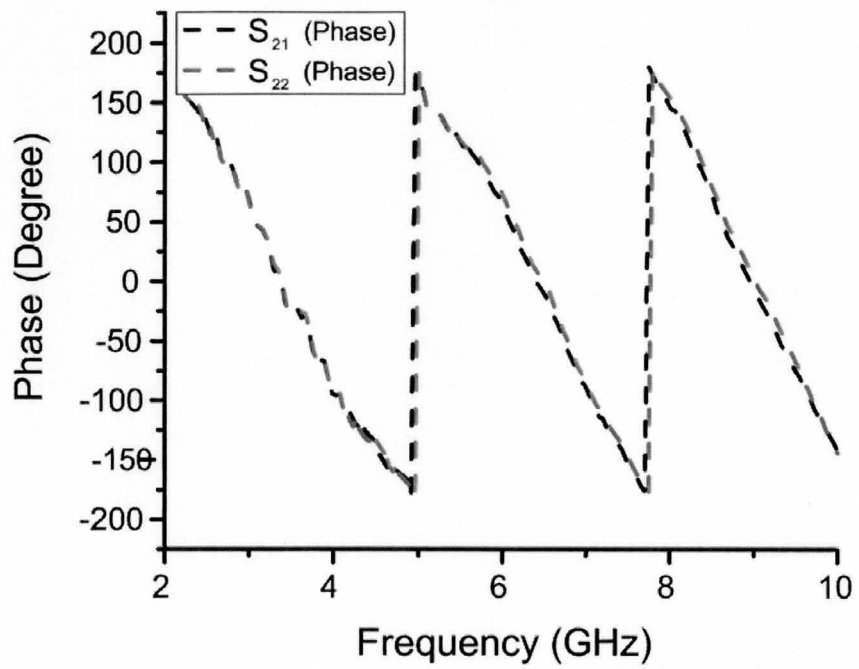


Figure 4.37. Measured phase of the cross-polarized array element.

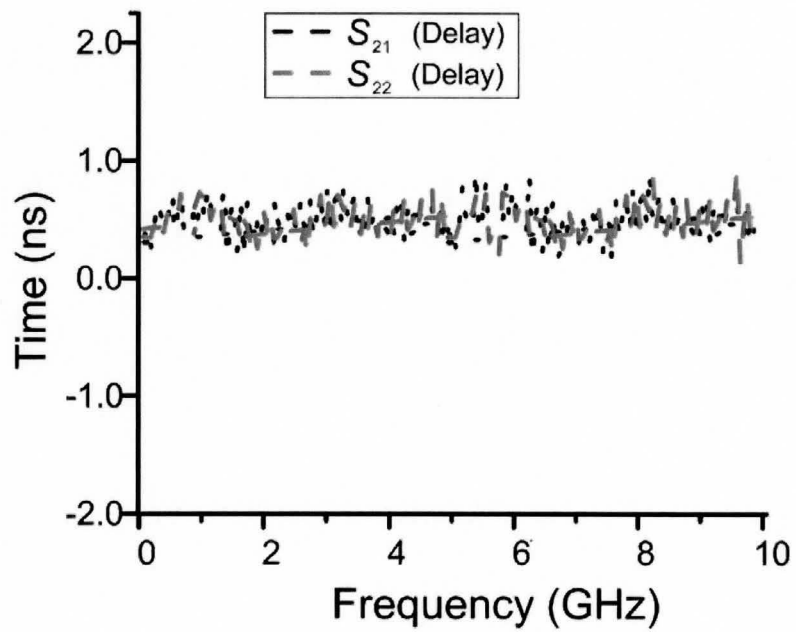
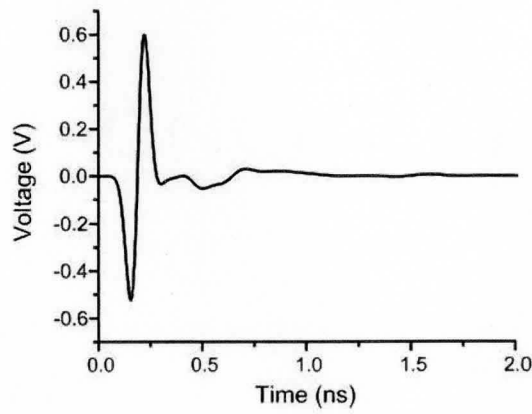


Figure 4.38. Measured group delay between two antennas of the cross-polarized array element.

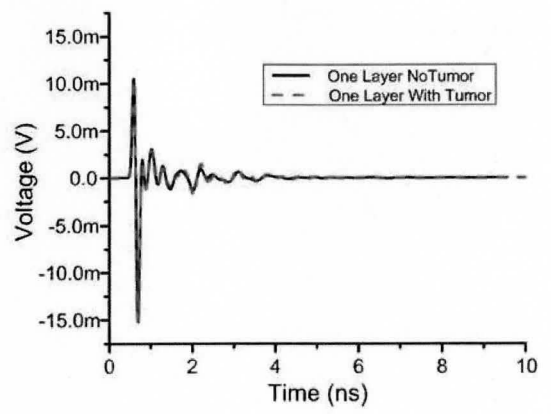
C. Tumor detection capabilities (simulation)

To investigate the imaging capabilities of the cross-polarized array element for the purpose of breast cancer detection, a set of XFDTD simulations, similar to the case of the co-polarized array element has been performed. Results of this set of simulations are plotted in Figure 4.39.

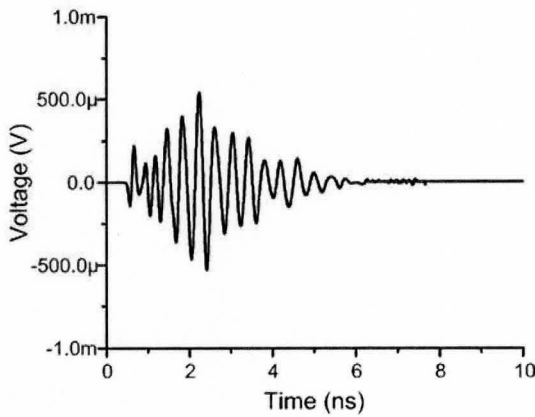
The energy of the received pulse from an $8 \text{ mm} \times 10 \text{ mm}$ tumor is -51 dB below energy of the pulse that was placed at the feed of transmitter antenna. As a result, it can be concluded that the UWB imaging system employing cross-polarized antenna array should achieve dynamic range of greater than 51 dB in order to detect a tumor of this size at the depth of 3 cm . Also, as it can be seen from Figure 4.39(b), although the coupling between two antennas is smaller than the coupling between the antennas in the co-polarized configuration, it is still large enough to mask the tumor response. Therefore, it should be removed from the received signal before any signal processing is done to detect presence of tumor. In the second simulation scenario, the energy of the muscle response is 15 dB higher than the energy of tumor response. Therefore, the muscle response practically covers tumor response. Given that muscle response is not deterministic, we cannot simply subtract it from the total response of the muscle and tumor to determine the tumor response. Also, the received energy from the one layer tumor response, muscle response and the two layer tumor response is respectively -7 dB , -11 dB and -8 dB smaller than the energy received with co-polarized antenna array. From these discussions, it can be concluded that the co-polarized antenna array will outperform the cross-polarized antenna array, but both array configurations will have limited capabilities in detecting tumors close to the chest wall.



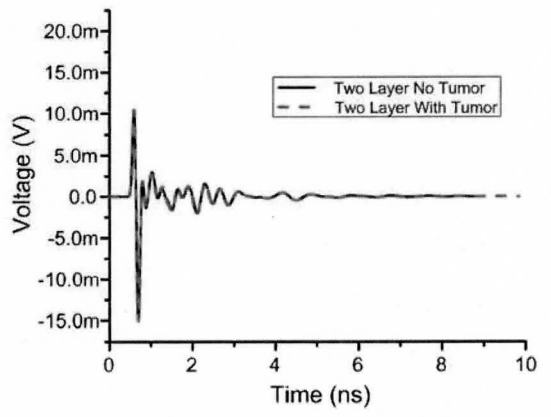
(a)



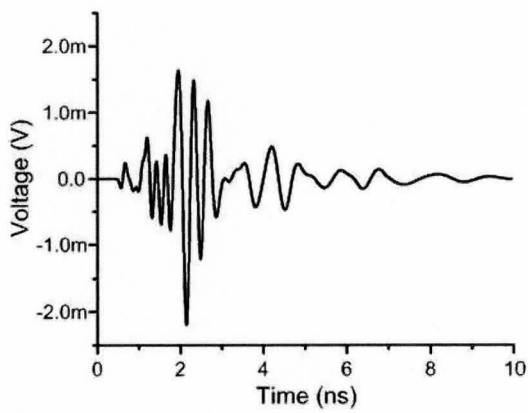
(b)



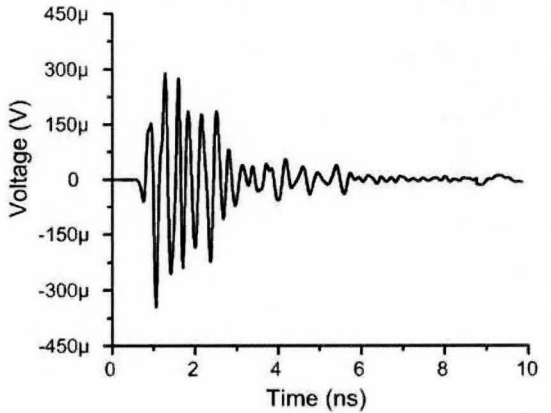
(c)



(d)



(e)



(f)

Figure 4.39. (a) Input signal to the transmitted antenna. (b) Received pulse at the receiver antenna, for one layer simulation scenario. (c) Tumor response from one layer simulation scenario. (d) Received pulse at the receiver antenna, for two layer simulation scenario. (e) received signal due to the mussel layer. (f) Tumor response from one layer simulation scenario.

4.6.1.3 Measured Tumor Detection Capabilities (co-polarized array)

A set of experiments were conducted to investigate the tumor detection capabilities of the co-polarized arrays in the breast cancer detection systems. The tumor detection capabilities of the cross-polarized antenna array are not studied. This is because from the XFDTD simulations, it did not provide any advantage over the co-polarized array formation.

The experiment was conducted to study the detection of tumors that are not close to a planar chest wall. The measurement environment for the first experiment is similar to the one used to measure the S -parameters. The antenna arrays are placed in the coupling medium where one antenna is used as the transmitter and the other as the receiver. The transmitting antenna is connected to an Anritsu-MP1763B Pulse Pattern Generator, which generates a 1 V (peak-to-peak), 200 ps duration pulse, as shown in Figure 4.40. This pulse is recorded by directly connecting the pulse pattern generator to an Agilent 86100A wide-bandwidth oscilloscope with a sampling rate of 135 GHz. We note that this pulse generator cannot generate a pulse of zero-DC component. The pulse shown in Figure 4.40 is close to a Gaussian pulse, which we feed directly to the transmitter antenna. The receiver antenna is connected to the wide-bandwidth oscilloscope, which records the backscattered. The experiment of setup is shown in Figure 4.41.

To simplify the experimental setup, the malignant tumor is mimicked by a plastic tube of diameter 0.8 cm and length of 1 cm, containing distilled water. It is placed in front of the antenna array. The distance from the tumor to the antenna array is varied from 0 to 6 cm in steps of 1 cm and the received backscattered signal is recorded. This signal is due to the reflection from the tumor as well as the coupling between the array elements and the reflections from the walls of the plastic container holding the coupling medium. To obtain the response of the tumor alone, the reflected signal from the wall of the plastic container and the coupling between the array elements is first acquired and is then subtracted from the overall backscattered signal.

The tumor response for different tumor depths is plotted in Figure 4.42 (a), (b) and (c). The general shape of the tumor response is similar to the second derivative of a Gaussian pulse. This is due to the fact that radiated E -field by the transmitter antenna is

the first order derivative of the input pulse and the received pulse is the derivative of the E -field collected by the receiver antenna. Also due to the frequency-dependent attenuation and phase delay in the biological medium, the general shape of the tumor response degraded as the tumor is placed further from the transmitter antenna.

The energy of the tumor response, normalized to the energy of the transmitted pulse (the system gain) for different depths, is plotted in Figure 4.42 (d). The normalized energy of the tumor response at 0 cm is -38.8 dB for the co-polarized array. The received energy of the antenna arrays decreases by approximately 4 dB for every centimeter increase in the depth of the tumor.

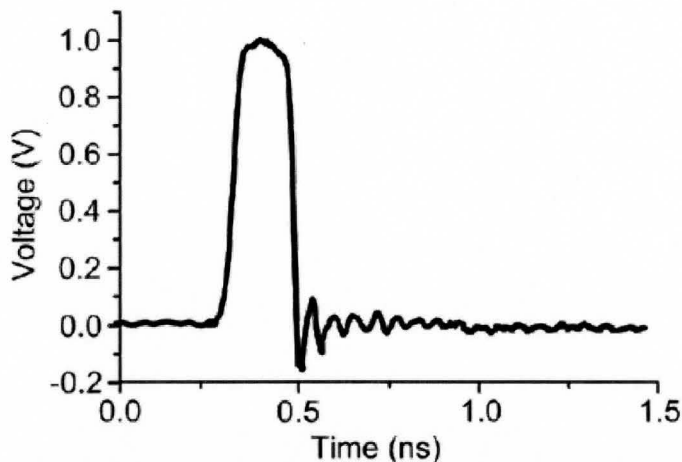


Figure 4.40. Voltage waveform used to excite the transmitter antenna.

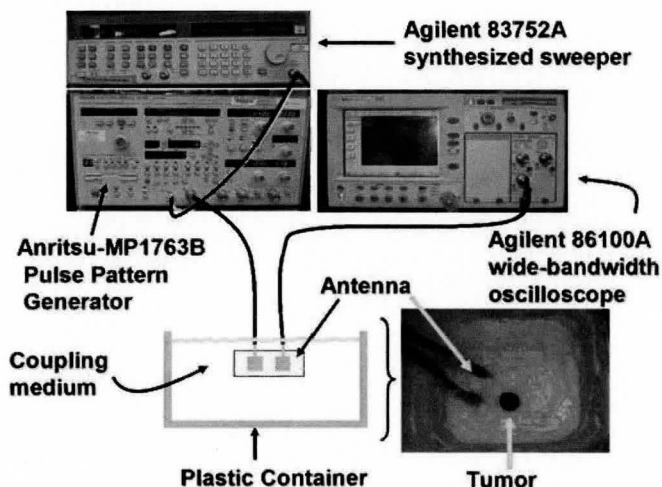


Figure 4.41. Measurement setup

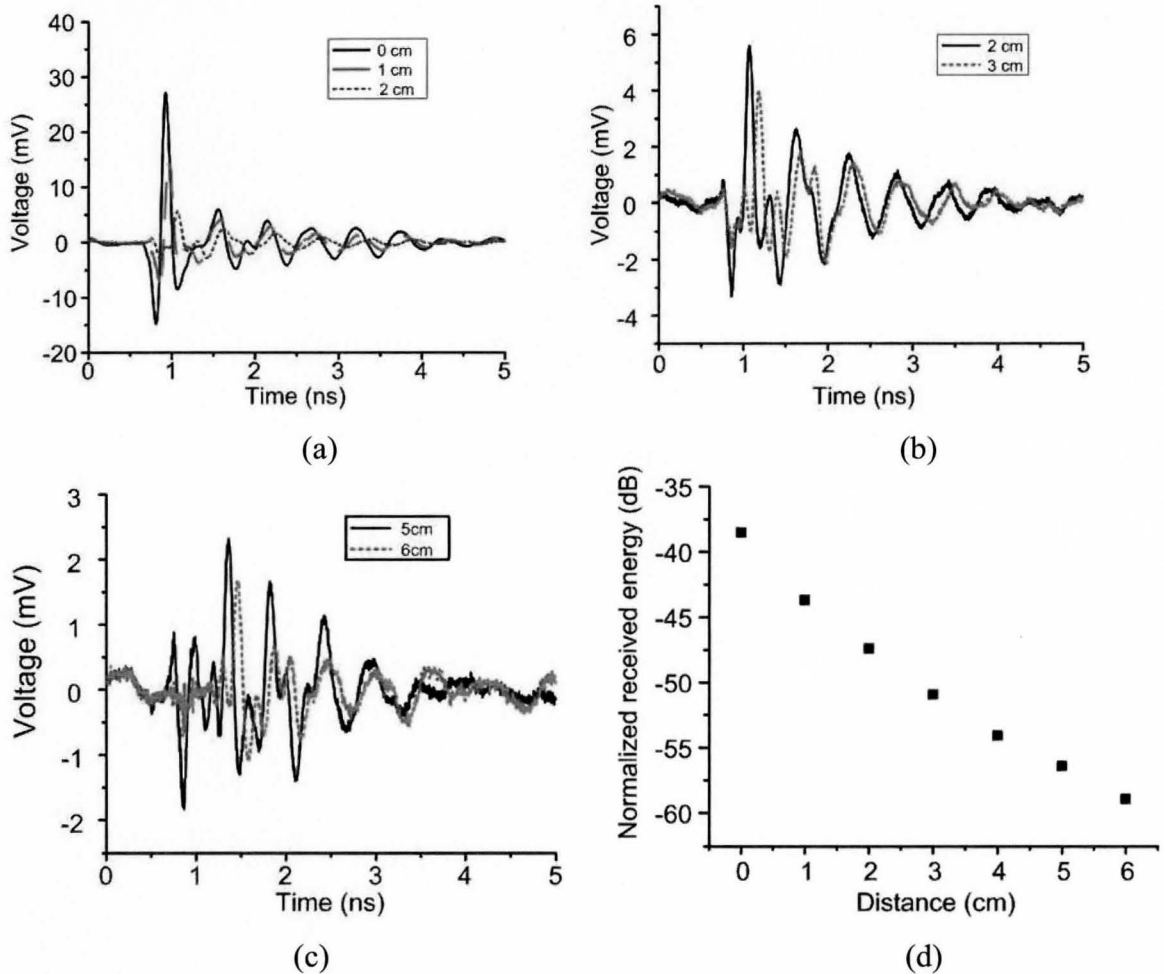


Figure 4.42. (a) received pulse from tumor at depth of 0, 1 and 2 cm, (b) received pulse from tumor at depth of 3, 4 cm (c) received pulse from tumor at depth of 5, 6 cm, (d) normalized received energy from tumor at different depth.

4.7 Summary

The design procedure, simulation and measurement results of the TSPM UWB antennas for communication and imaging applications were presented. The detail design procedure of the TSPM antenna fed with CPW waveguide is discussed and the first resonant frequency of the antenna is approximated. The antenna is fabricated on commercially available PCB (FR-4), which can significantly reduce cost of the UWB imaging and communication systems.

The parameters that affect the antenna performance are investigated using the HFSS optimization tool. It was found that contrary to the square monopole antenna on a large ground plane, reducing the width of the antenna does not improve the impedance bandwidth and the optimum width of the antenna is slightly larger than the length of the antenna. It is shown experimentally that the TSPM antenna achieves ultra-wide bandwidth from 2.2 to 8.75 GHz, while providing an acceptable radiation pattern.

The same antenna is redesigned and fabricated to operate in a lossy coupling medium for applications in UWB breast cancer detection systems. The characteristics of the antenna operating in this medium and in proximity to the human body were investigated. The SAR distribution in the human body was presented and it has been found that the maximum SAR occurs close to the radiating element over the whole UWB operating band. Also, it was found that the antenna has an omni-directional near-field pattern over the entire band of operation. It is shown experimentally that the TSPM antenna can achieve ultra-wide bandwidth from 3.4 to 9.9 GHz while operating in the biological coupling medium. This enables the antenna to efficiently couple energy into the human body.

The performance characteristics of a TSPM antenna in a co-polarized and a cross-polarized array formation in a breast cancer detection system were investigated. The antenna measurement results indicate input matching of better than -10 dB from 3.4 to 10 GHz and the coupling between the antennas is below -15 dB and -20 dB for the co- and cross-polarized array formation. Detection capabilities of the antenna arrays for tumors close to the chest wall and away from the chest wall were studied. It was found through simulation and measurements that for the TSPM antenna array, the co-polarized energy of the tumor response is in general 7 dB higher than the cross-polarized response. Therefore, we concluded that the co-polarized antenna array element will outperform the cross-polarized antenna array element. Also, it is found through simulation that the ratio of the tumor response to the muscle response is -7 and -8 dB for the co- and cross-polarized antenna array elements. From these results, we can conclude that both array configurations will have limited capabilities in detecting tumors close to the chest wall.

Chapter 5: WIDEBAND SLOT ANTENNA

In this chapter, the design and performance characteristics of an ultra-wideband (UWB) slot antenna for communication and medical imaging applications are presented. The wideband slot antenna achieves similar performance to the TSPM antenna in Chapter 4, but with smaller physical sizes. The antenna is fed with a 50 Ω coplanar waveguide and provides impedance bandwidth in excess of 7.5 GHz in both air and a coupling medium. The effect of varying in the antenna's geometrical parameters on its impedance bandwidth is studied using the HFSS optimization tool [32]. It is found through simulation and measurement that for wideband slot antennas, the first resonant frequency occurs when the length of the slot is equal to one guided wavelength at the operating frequency.

To meet the UWB system compatibility requirements, a wideband slot antenna with narrow band rejection capabilities has also been designed. The antenna successfully rejects 5-6 GHz bandwidth occupied by IEE802.11a, making the UWB system immune to this narrowband interference.

The wideband slot antenna has been redesigned for use in a UWB cancer detection system. To reduce the reflections from the air-skin interface, the antenna has been placed in a coupling medium with dielectric properties similar to those of human tissue. The antenna has been characterized while operating in the coupling medium and in proximity to a human body model. Measurement results indicate that the wideband slot antenna can achieve an ultra-wide bandwidth in excess of 7.5 GHz while operating in a lossy coupling medium.

Finally, a two element antenna array in a co- and a cross-polarized formation has been designed for breast cancer detection system, and the array's tumour detection capabilities have been investigated. It is shown through simulations and measurements that the cross-polarized antenna array improves the signal to-clutter ratio for tumors close to a planar chest wall.

ensuring wideband operation of the antenna. Also, it minimizes the physical dimensions of the antenna, since tapering results in a higher slot length of smaller area. The tuning stub controls level of electromagnetic energy coupled to the radiating slot. That is why the general shape of the tuning stub is chosen similar to the radiating slot, thus enhancing the coupling. The base of the tuning stub has been linearly tapered to ensure good impedance match and electromagnetic radiation in a broad frequency range [24].

The first resonance of the antenna occurs when the shortest current path around the inner boundary of the slot ($2 \times L_1 + 2 \times L_2 + 2 \times L_3 + L_4$) is equal to one guided wavelength at that frequency. As a result, the lowest operating frequency of the slot antenna is approximately equal to:

$$f_l = \frac{c}{\sqrt{\epsilon_{eff}} \times L_l}, \quad (5-1)$$

where c is speed of light, L_l is the longest current path around the inner boundary of the slot antenna and ϵ_{eff} is effective dielectric constant which is given by:

$$\epsilon_{eff} = \frac{\epsilon_r + 1}{2}. \quad (5-2)$$

In the proposed design, L_l is set to 90 mm, which corresponds to the lowest operating frequency of 2.02 GHz. The upper cut-off frequency is determined by the height of the gap between the point A_y and point I_y as shown in Figure 5.1 and the tapering profile of the radiating slot and the distance from the tuning stub to the radiation slot. The optimum value of these parameters is found through HFSS parametric simulation, as described in the following section.

B. Antenna Optimization

The geometrical parameters of the antenna has been optimized for the lowest overall reflection coefficient (S_{11}), using HFSS optimization tool. The first parameter of the antenna that is investigated is the radius of the tuning stub F . The HFSS software has been used for this purpose and the antenna is simulated for radii of $F = 10, 11, 12, 13$ and 14 mm. A variation in the radii of the tuning stub changes the overall performance of the antenna over the UWB operating band (3-10 GHz). This is due to the fact that the tuning

stub controls the level of the electromagnetic coupling into the radiating slot, and changes in the level of coupled electromagnetic energy affect the input impedance of the antenna. It can be seen from Figure 5.2 that as the radius of the tuning stub increases from 10 mm to 14 mm, the reflection coefficient improves in the 3.0-5.0 GHz and 7.0-9.0 GHz band, but on the other hand, it degrades in the mid band (5.0-7.0 GHz). The widest bandwidth is achieved with the radius of 12 mm. Also, as expected from equation (5-1), the lower cut-off frequency of the slot antenna is fairly insensitive to variations in the radii of the tuning stub.

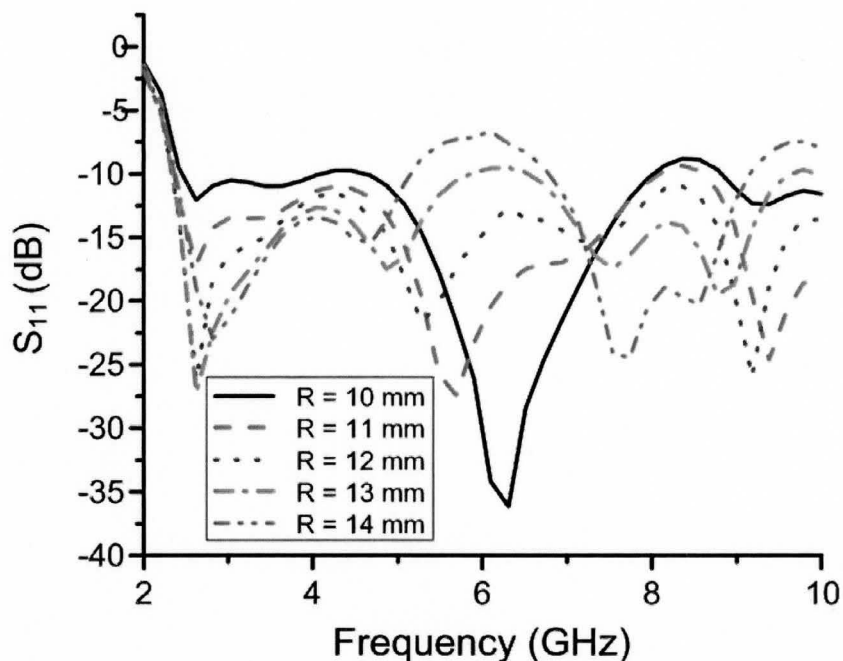


Figure 5.2. Simulated return loss for different radius of the tuning stub.

To investigate effects of variation in the tapering profile of the radiating slot on the antenna's reflection coefficient, first, the parameter D_X which controls the tapering profile of the radiating slot was simulated for values of $D_X = 14, 16, 18, 20$ and 22 mm. The simulation results are plotted in Figure 5.3. A variation in D_X does not significantly affect the reflection coefficient over the UWB operating band, but on the other hand it changes the shortest current path along the radiating slot and as a result, it significantly affects the lower cut-off frequency of the antenna.

Next, the parameter C_X which controls the tapering profile of the radiating slot and the ground plane with respect to the tuning stub, was simulated for values of $C_X = 12,$

14, 16, 18 and 20 mm. The simulation results are plotted in Figure 5.4. A variation in C_x significantly affects the reflection coefficient over the entire UWB operating band. The variation in C_x affects the distance from the ground plane to the lower edges of the tuning stub, and changes in the tapering between the ground plane and the tuning stub affects the impedance of higher order modes which controls the antenna's reflection coefficient over the UWB operating band. A variation in C_x also changes the shortest current path around the radiating slot, and as a result, it significantly affects the lower cut-off frequency of the antenna.

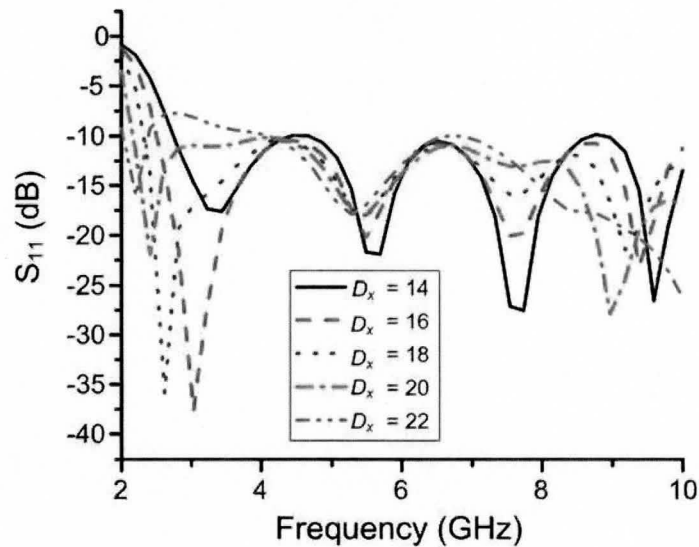


Figure 5.3. Simulated return loss for different values of D_x .

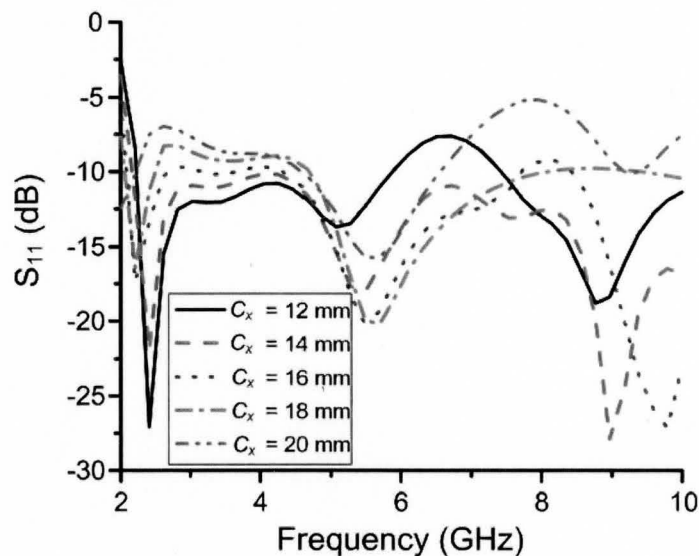


Figure 5.4. Simulated return loss for different values of C_x .

C. Antenna Measurement and Simulation Results

A prototype antenna was fabricated on a FR-4 PCB with $\epsilon_r = 4.4$ and $\tan\delta = 0.016$. The optimized antenna physical parameters are given in Table 5.1. The antenna's VSWR (voltage standing wave ratio) is measured using a HP 8720ES network analyzer. Open, short and through calibration procedure was conducted using the economy 83050B calibration kit, and the network analyzer was calibrated up to the feed of the antennas. The measured and simulated VSWR are shown in Figure 5.5. The measured antenna's VSWR is below 2 from 2.3 to 10 GHz and it is in a good agreement with the simulation results.

Table 5.1

ANTENNA'S PARAMETERS

Symbol	[X,Y] (mm)
<i>A</i>	-1.6, 0.1
<i>B</i>	-2.2, 0.1
<i>C</i>	-14, -0.8
<i>D</i>	-18, -10
<i>E</i>	0, 23
<i>F</i>	-11.5, 3.2
<i>G</i>	-4.3, 11.2
<i>H</i>	0, 4
<i>L</i>	0, 36
<i>W</i>	48, 0

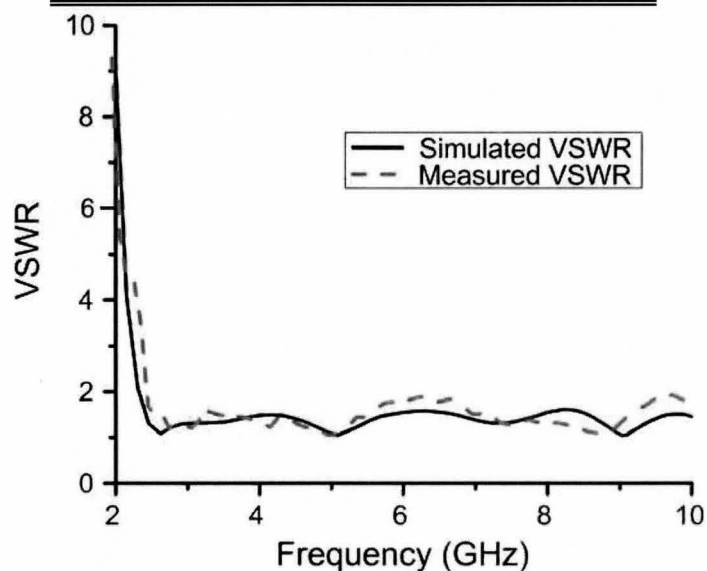


Figure 5.5. Simulated and measured VSWR of CTS Antenna.

5.2 CTS Antenna's Radiation Characteristic

The HFSS software has been used to simulate the far-field radiation pattern of the CTS antenna. The radiation patterns of the antenna at 2.5, 3, 4, 5, 6, 7, 8, 9 and 10 GHz, in three planes of XY, ZX and ZY are plotted in Figure 5.6 and Figure 5.7. As it can be seen from the plots, the radiation pattern from 2 to 4 GHz is nearly omnidirectional in the H -plane, and it is monopole-like in the E -plane. At 5 GHz, the radiation pattern is similar to the lower frequency band, except for two notches that appear in the $+x$ and $-x$ axes. From 2 to 5 GHz, the maximum of the radiation pattern stay in the z -axis, but at higher frequencies (6-10 GHz), the maximum of the radiation pattern tilts toward the $+y$ -axis. Also, at these frequency bands, the radiation pattern of the antenna is distorted and multiple lobes can be seen. The distortion in the radiation pattern of the antenna is caused by an increase in the electrical length of the antenna at the higher frequencies and the radiation from the tuning stub and the CPW.

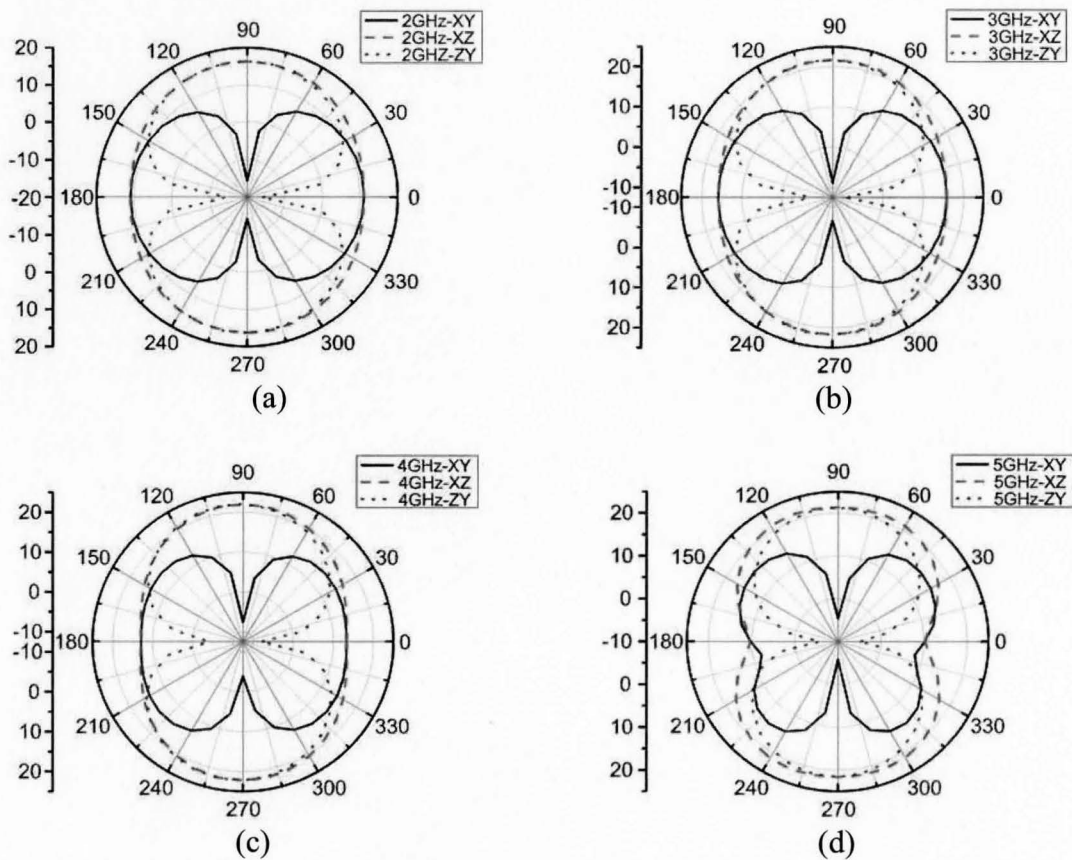


Figure 5.6 CTS antenna's radiation pattern at (a) 2.5 GHz, (b) 3 GHz, (c) 4 GHz, and (d) 5GHz

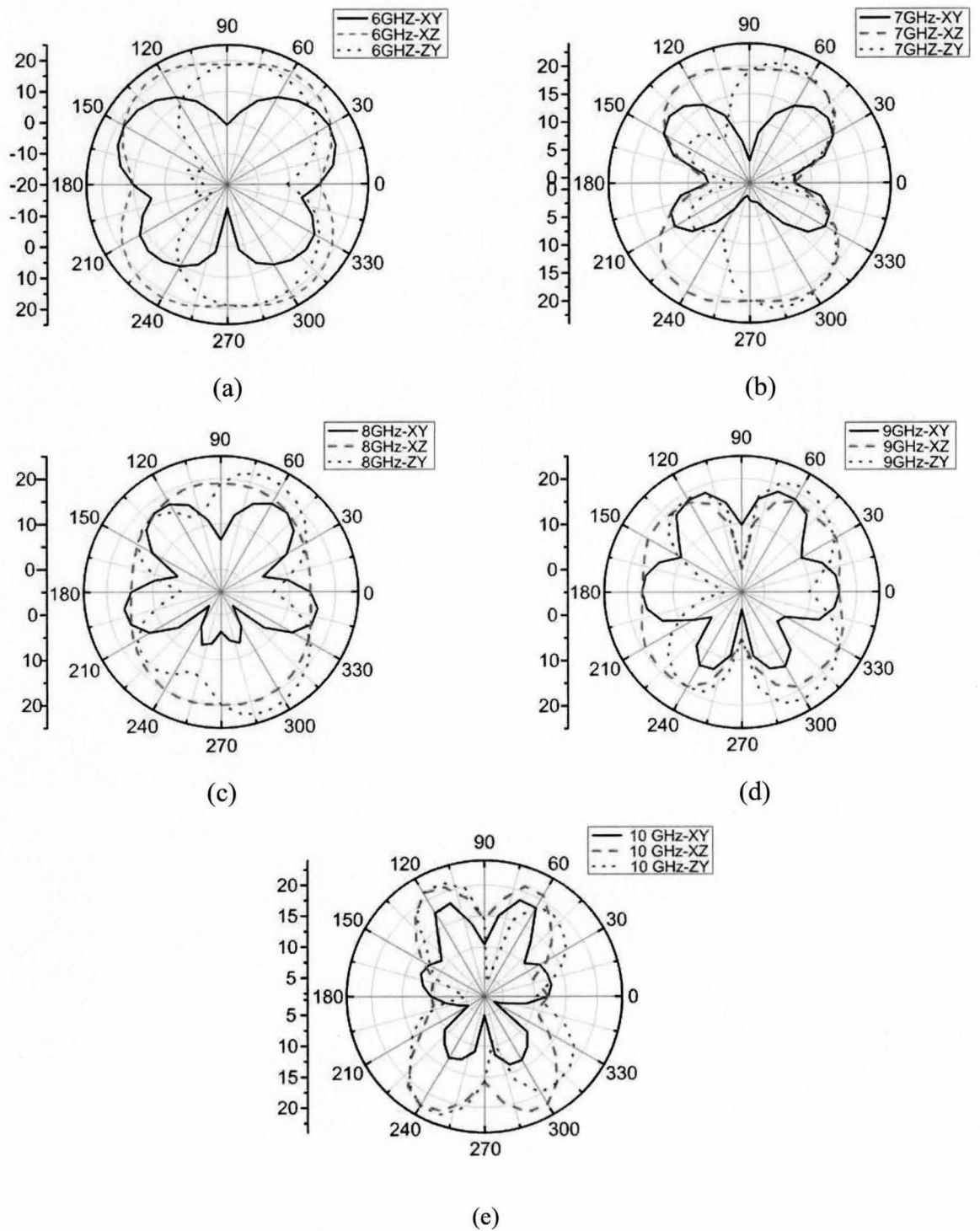


Figure 5.7 CTS antenna's radiation pattern at (a) 6 GHz, (b) 7 GHz, (c) 8 GHz, (d) 9 GHz, and (e) 10 GHz.

5.3 CTS Antenna Surface Current Distribution

The surface current distribution on the CTS antenna has been studied using the HFSS simulator. Figure 5.9, Figure 5.10 and Figure 5.11 show plots of the magnitude of simulated surface current distribution on the radiating slot and the tuning stub at frequencies of 2.5, 3, 4, 5, 6, 7, 8, 9 and 10 GHz. On the radiating slot, the current is mainly concentrated on the edges of the slot, and on the tuning stub, the current is mainly distributed on the lower edges of the stub and in the vicinity of the radiating slot. The surface current distribution on the radiating slot indicated the existence of multiple resonant modes, which proves that the tapered radiating slot can support multiple resonant modes. As it can be seen from Figure 5.9, the first resonating mode is at 2.5 GHz, and length of the radiating slot at this frequency is equal to one guided wavelength. There are two peaks in the magnitude of surface current density and they are symmetrically distributed on both sides of the radiating slot, which is what we expect if we assume a sinusoidal current distribution as shown in Figure 5.8. The second resonating harmonic is at 5 GHz and the length of the slot at this frequency is equal to two guided wavelengths. There are four peaks in the magnitude of surface current density and they are symmetrically distributed around the perimeter of the radiating slot. The third resonating harmonic is at 9 GHz and the length of the slot at this frequency is equal to three guided wavelengths. There are six peaks in the magnitude of surface current density and they are symmetrically distributed around the perimeter of the radiating slot. Since the magnitude of the surface current is distributed both on the radiating slot and the tuning stub, we can conclude that both the tuning stub and the radiating slot affect the input impedance of the antenna over the UWB operating band. This is the effect that was observed during optimization of the antenna.

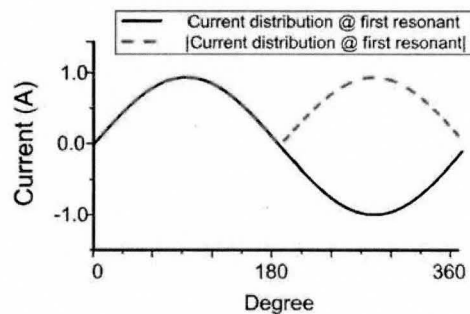
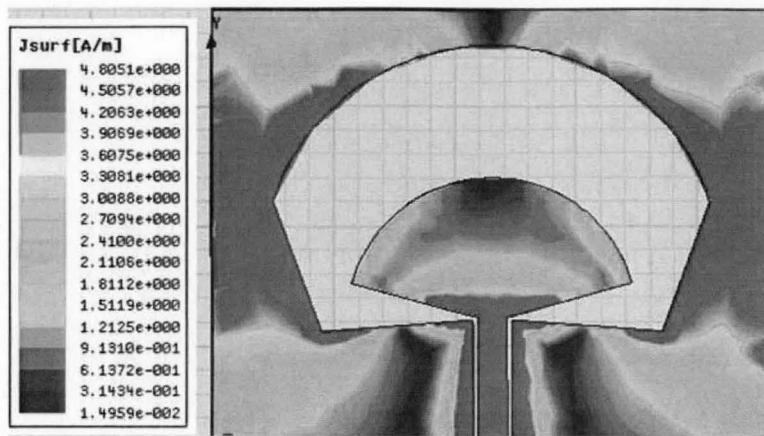
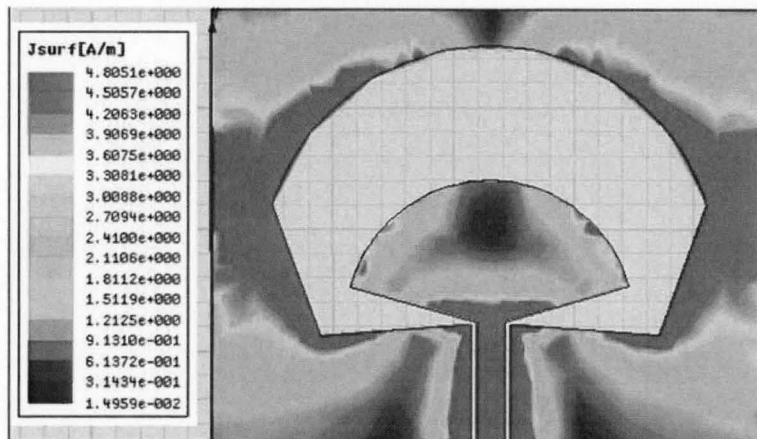


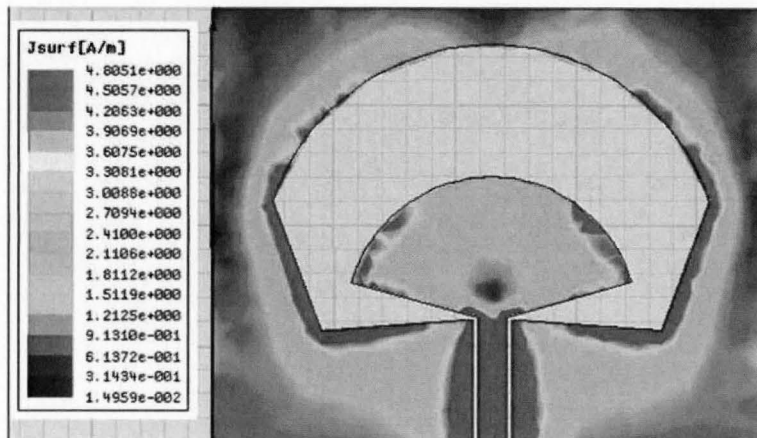
Figure 5.8. Sinusoidal current distribution at the first resonant frequency.



(a)

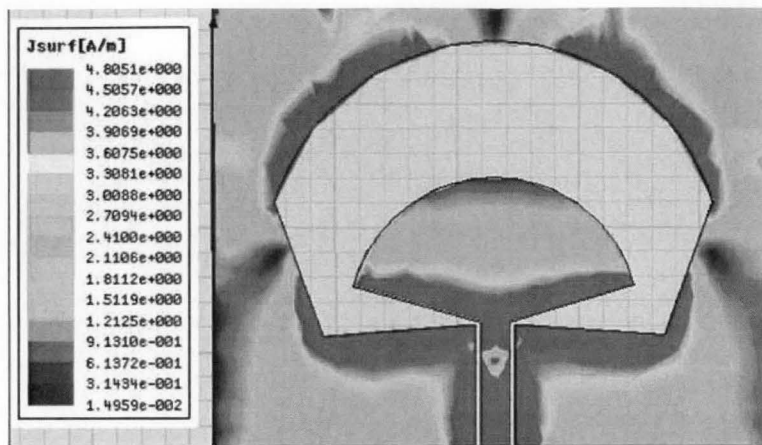


(b)

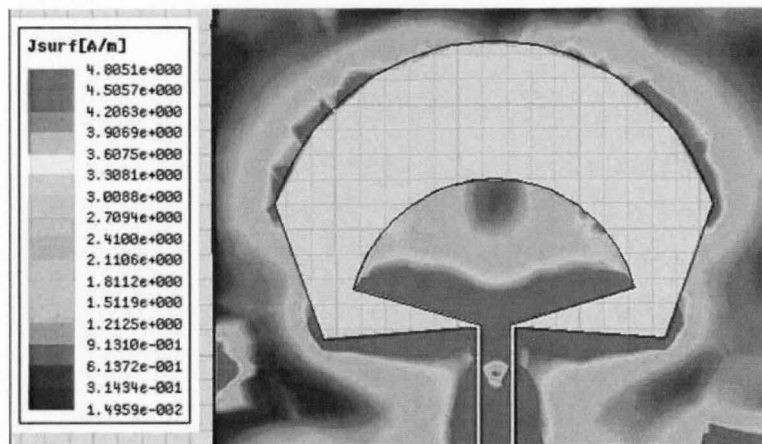


(c)

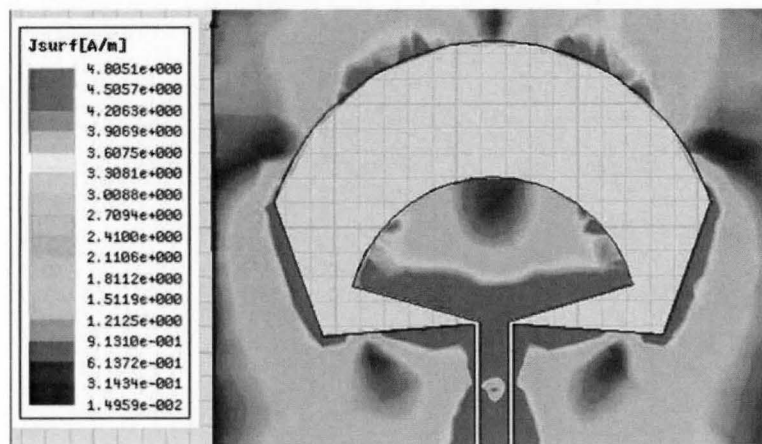
Figure 5.9. Surface current distribution at (a) 2.5 GHz, (b) 3 GHz, and (c) 4 GHz.



(a)

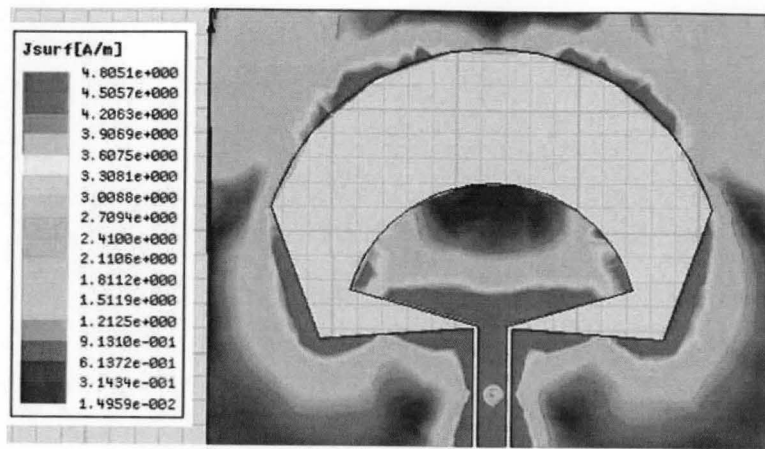


(b)

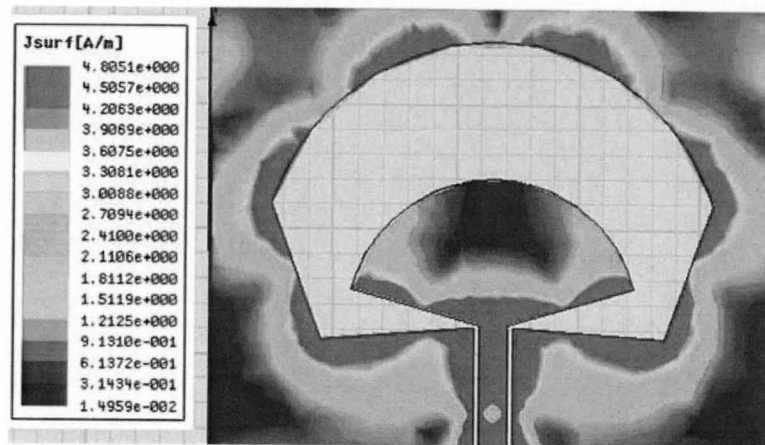


(c)

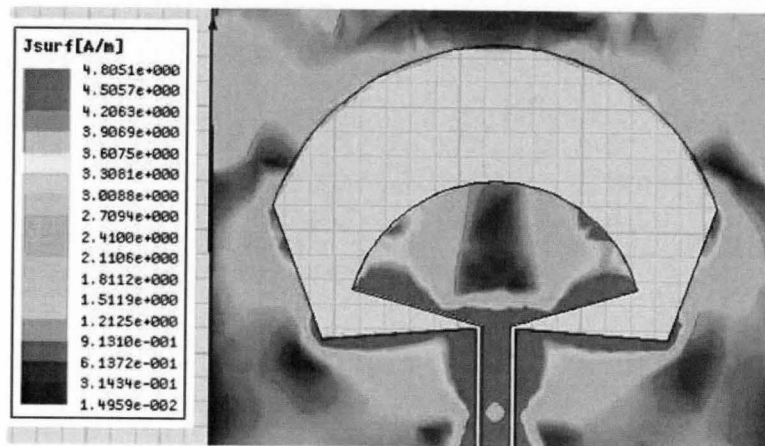
Figure 5.10. Surface current distribution at (a) 5 GHz, (b) 6 GHz, and (c) 7 GHz.



(a)



(b)



(c)

Figure 5.11. Surface current distribution at (a) 8 GHz, (b) 9 GHz, and (c) 10 GHz.

5.4 CTS Antenna with a Frequency Notched Characteristic

An ultra-wideband systems targeting communication applications can be required to operate in proximity of a narrowband system that occupy a frequency band within the UWB operating bandwidth. An example of such narrow band system is IEEE 802.11a which is centered at 5.6 GHz. Such a narrowband system can potentially interfere with an ultra-wideband system due to the high level of transmitted power. Therefore, it would be desirable to make the UWB system insensitive at the frequencies in which these narrowband systems operate.

A conventional method to implement a UWB system insensitive to the narrowband interference is to connect the UWB antenna to a band rejection filter which passes all the frequencies in the UWB operating band except for the frequency band occupied by the interfering narrowband system. This method will result in a UWB system that is sensitive to the entire UWB operating band with the exception of the band that is rejected by the filter. Although this solution will make the UWB system immune to the narrow band interference, it will also increase the cost, noise figure and the complexity of the UWB system due to the need for the extra passive/active components and the transmission lines required to implement the band notch filter.

An alternative to the above solution is to design the UWB antenna such that it is not matched at the frequency band of operation of the narrowband system. In this method, the UWB system would not be able to transmit or receive at the frequency band in which the antenna is not matched and as a result, the overall UWB system becomes insensitive to the interfering frequency band.

UWB antennas with a band rejection characteristic can be designed by inserting a narrow band resonating structure into the UWB antenna [46]. At the resonating frequency of the narrow band structure, a destructive interference takes place, causing the antenna to reject that frequency band. To provide the band notch characteristics for the wideband slot antenna, a V-shape resonating slot has been inserted in to the tuning stub as shown in Figure 5.12. The V-shape slot resonates at the frequency where L_2 is equal to $\lambda_g/4$. Figure 5.13 shows the current distribution at the notch frequency on the tuning stub with and without the resonating V-shaped slot. As shown in Figure 5.13, for the antenna without

the V-shape slot, there is a high surface current density at the feed point of antenna and the direction of the surface current is out of the CPW toward the edges of the tuning stub. On the other hand, for the antenna with the resonating V-shaped slot, the current is mostly concentrated around the upper edges of the resonating slot and it is oppositely directed on each sides of the slot. This current configuration transforms nearly zero impedance at top of slot to the high impedance at the antenna feed point. This high impedance at the feed point leads to the desired high attenuation and impedance mismatch at the notch frequency [47].

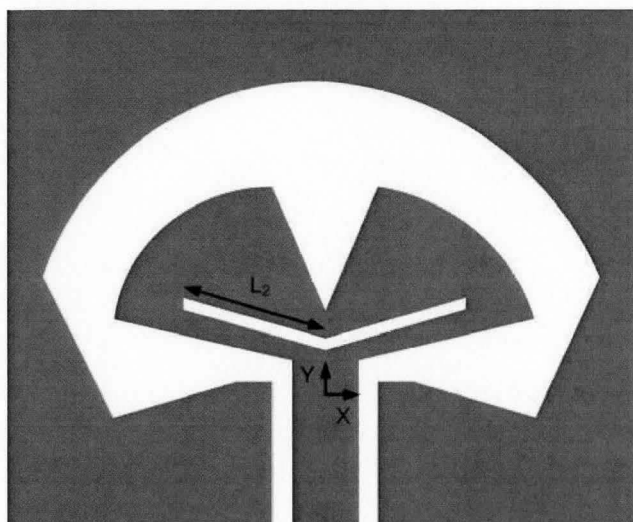
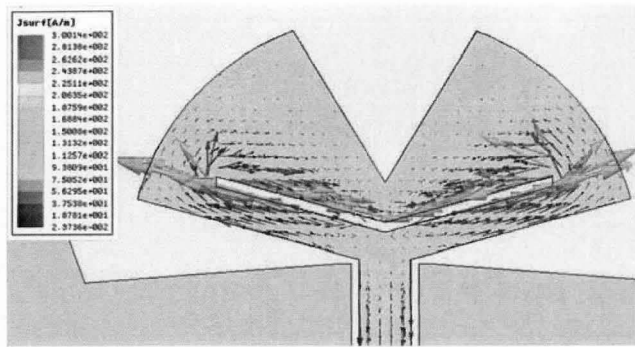
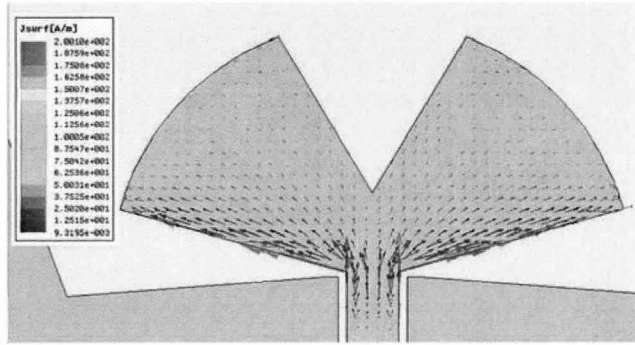


Figure 5.12. Geometry of the slot antenna with band notch characteristic.

A prototype antenna with the V-shaped resonating slot was fabricated on a FR-4 substrate with $\epsilon_r = 4.4$ and $\tan\delta = 0.016$. The antenna's physical parameters are the same as that given in Table 5.1. The antenna's return loss is measured using a HP 8720ES network analyzer. The measured and simulated VSWR are shown in Figure 5.14. The measured antenna's VSWR is below 2 from 2.5 to 9.3 GHz, except for the sharp frequency notch in the 5 to 6 GHz band, which is created by the V-shaped slot. Note also that the measurement results are in a good agreement with the simulation results.



(a)



(b)

Figure 5.13. Surface current distribution on the tuning stub (a) antenna with the V-shape slot, and (b) antenna without the V-shape slot.

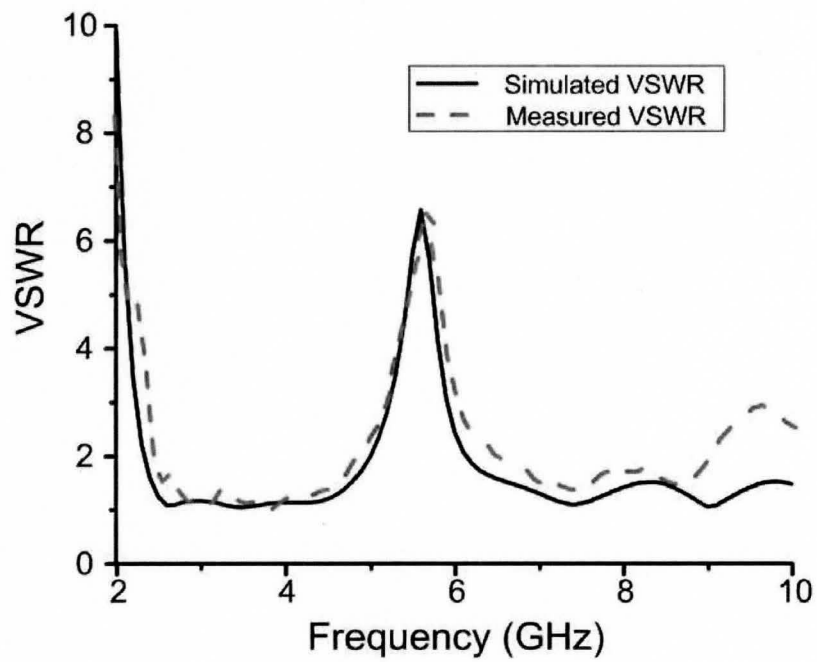


Figure 5.14. Measured and simulated antenna VSWR.

The far-field radiation pattern of the antenna has been simulated using the HFSS software. The gain at 5.6 GHz for the antenna with and without the resonating slot is plotted in Figure 5.15. The maximum gain of the antenna without the resonating slot is 4.5 dB, while the maximum gain of the antenna with the resonating slot is 1.5 dB.

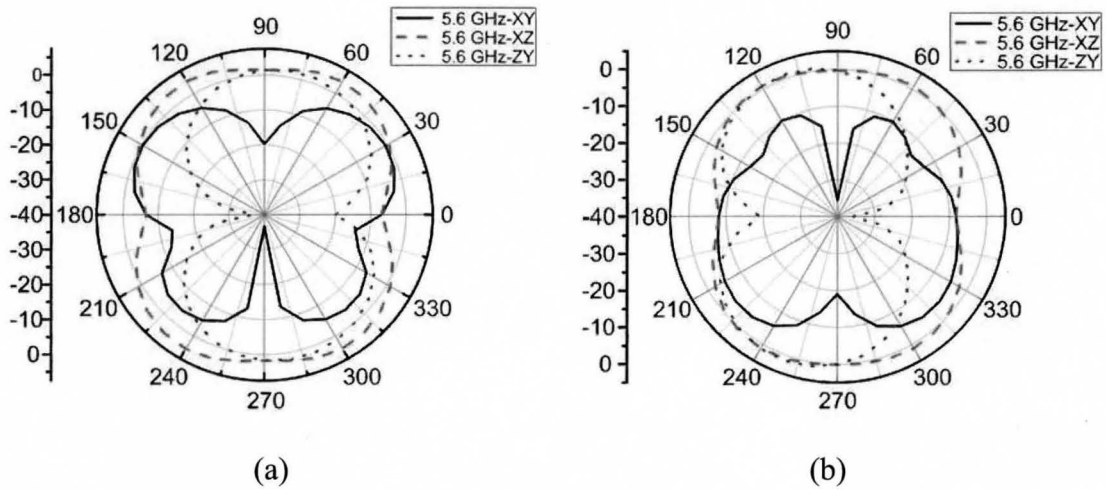


Figure 5.15. Antenna radiation pattern (a) without the V-shaped slot. and (b) with the V-shaped slot.

To investigate the effect of the V-shaped slot on the wideband planar monopole antenna, and to determine whether the gain of the antenna with the V-shaped slot is mainly due to the radiation from the wideband slot or the radiation from the V-shaped slot, we have removed the radiating slot around the tuning stub as shown in Figure 5.16.

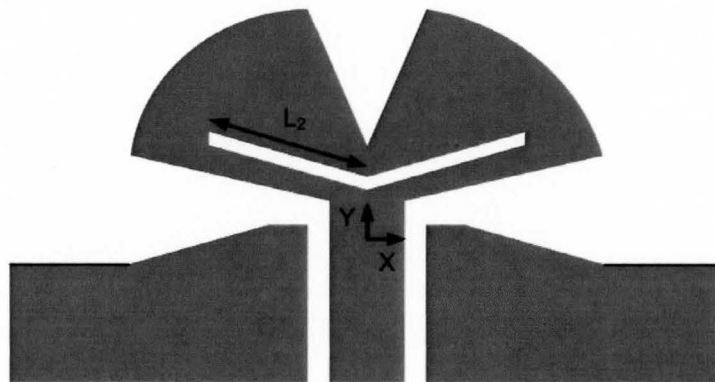


Figure 5.16. Geometry of the monopole antenna with band notch characteristic.

The geometrical parameters of the new antenna are the same as the one given in Table 5.1, and the radiating slot has been removed from point X_C . The new antennas have been simulated in HFSS, and the simulated VSWR's are plotted in Figure 5.17. For the antenna without the V-shaped slot, the VSWR is below 2 from 4 to 10 GHz, but for the antenna with the V-shaped slot, a frequency notch characteristic similar to the case of the wideband slot antenna is achieved.

From the simulated VSWR, it can be seen that the V-shaped slot provides similar band rejection characteristics for both the wideband slot and the printed monopole antennas. Also, it can be noticed that the first resonant frequency of the printed monopole antenna is at 4 GHz. Therefore, it can be concluded that for the slot antenna, it is the length of the slot that defines the first resonant frequency and not the tuning stub.

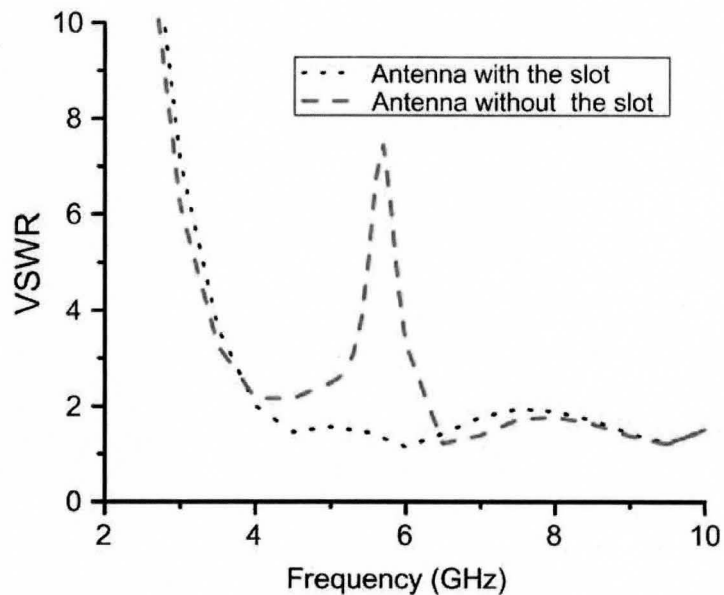
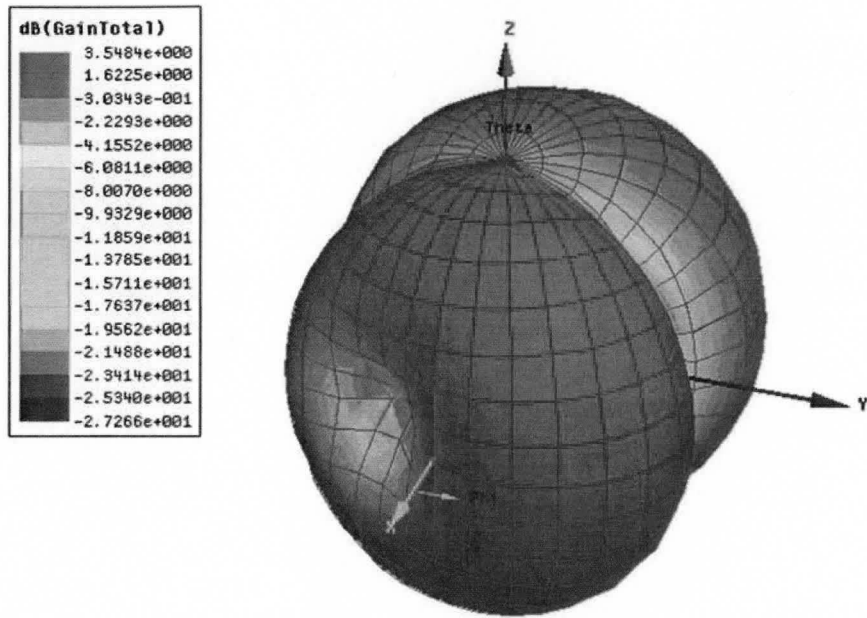
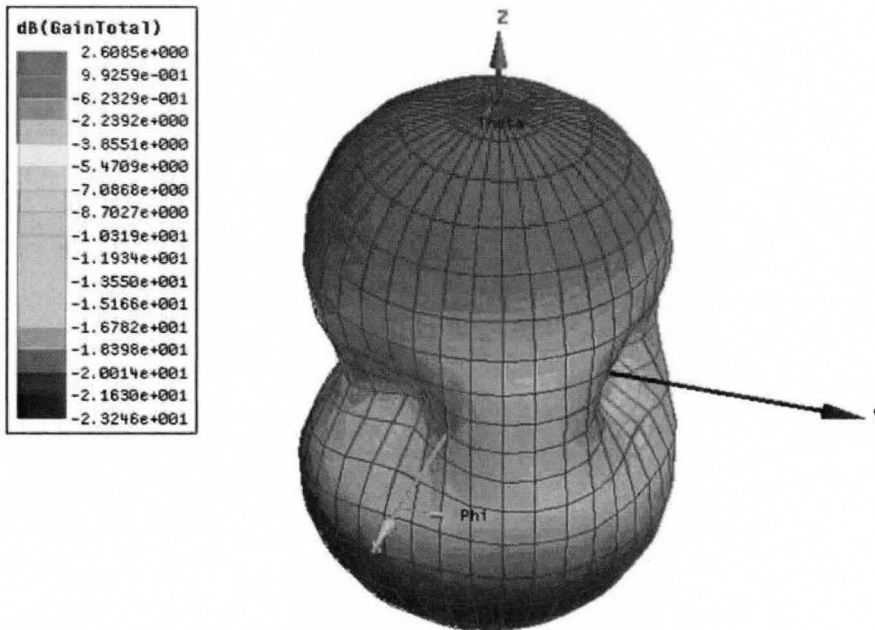


Figure 5.17. Simulated antenna VSWR with and without the V-shaped slot.

The far-field radiation patterns of both antennas have been simulated using the HFSS software. A 3D plot of the antenna gain at of 5.6 GHz for the antennas with and without the resonating slot is plotted in Figure 5.18. The maximum gain of the antenna without the resonating slot is 3.5 dB, and the maximum gain of the antenna with the resonating slot is 2.6 dB.



(a)



(b)

Figure 5.18. Antenna's radiation pattern (a) without the V-shaped slot, and (b) with the V-shaped slot.

It can be seen from Figure 5.18 that the drop in the maximum gain of the planar monopole antenna due to the V-shaped slot is only 0.9 dB, but for the same V-shaped slot, the gain of the wideband slot antenna drops by nearly 3 dB. Also, it can be noted that the radiation pattern of a planar monopole antenna with the V-shaped slot resembles that of the narrowband slot antenna on an infinite ground plane. Therefore, we can conclude that for the planar monopole antenna, at the notch frequency, the V-shaped slot is the main contributor to the radiation pattern. Although for the wideband slot antenna, the radiation pattern is different when a V-shaped slot is present, but this radiation pattern does not resemble the radiation pattern of narrowband slot antenna on an infinite ground plane. Therefore, it can be concluded that for the wideband slot antenna at the notch frequency, the tapered slot is the main contributor to the radiation pattern.

5.5 Wideband Slot Antenna for Biomedical Imaging

A. Antenna Design

As discussed in Chapter 2, antennas targeting UWB imaging applications should be placed in a coupling medium with dielectric properties close to that of human tissue to reduce the electromagnetic reflections from the air-skin interface. In this work, the wideband slot antenna has been redesigned to operate in the coupling medium (pork fat), thus making it suitable for UWB imaging applications.

The antenna was simulated in HFSS ver.9.2 using a 16 mm thick FR-4 substrate of $\epsilon_r = 4.4$, and fed with a 50- Ω lumped gap source. The simulation environment is a $(62 \times 62 \times 33.6)$ mm³ box where the radiation boundary was assigned to all faces of the box. Finally, the properties of the pork fat have been assigned to the box using the piecewise linear model available in HFSS to model the pork fat in the simulation environment. The circumference of the slot is set to 47.16 mm, which corresponds to the lowest operating frequency of 3.08 GHz. The HFSS optimization tool has been used to find the antenna's optimum parameters to achieve minimum S_{11} over the operating band. The optimized antenna's parameters are given in Table 5.2.

Table 5.2

CTS ANTENNA'S PARAMETERS FOR UWB IMAGING

Symbol	[X,Y] (mm)
<i>A</i>	-2.3, 0.1
<i>B</i>	-2.8, 0.1
<i>C</i>	-8.5, -1.1
<i>D</i>	-9.2, 5
<i>E</i>	0, 11
<i>F</i>	-6.0, 2.2
<i>G</i>	-0.8, 6.4
<i>H</i>	0, 6
<i>L</i>	0, 20
<i>W</i>	22, 0

A. Measurement and Simulation Results

The measurement environment and the setup of the return loss experiment are similar to the measurement setup of the TSPM antenna was shown in Figure 4.20 (a) and Figure 4.20 (b). An Agilent 85052D 3.5 mm calibration kit was used to calibrate the network analyzer to the end of the RF-cable feeding the antenna from 2 to 10 GHz. For the experiment 801 measurement, points and averaging the result 16 times were used.

The measured and simulated return loss of the antenna is plotted in Figure 5.19. The measurement results indicate a return loss of less than -10.0 dB from 3.1 to 10 GHz, and the measurement results is in a relatively a good agreements with the simulation results.

B. Proximity Effect

In the UWB imaging system, the UWB antenna and the coupling medium should be placed on the human body for imaging purposes. To investigate the effect of the human body on the input matching of the antenna, a study of the effects of the distance from the antenna to the skin interface has been conducted using HFSS. In this simulation, the distance *D* from the antenna to the skin interface has been changed from 1 mm to 20 mm, in increments of 5 mm. The simulation results plotted in Figure 5.20 show that the impedance bandwidth of the antenna is very sensitive to the separation between the

antenna and the skin interface as D changes from 1 mm to 20 mm. This implies that the antenna has a strong near E -field which is coupled into the skin interface and as a result of this coupling, the input impedance of the antenna is significantly affected. The reason for this strong coupling can be attributed to the fact that in the slot antennas, the energy is first transferred to the tuning stub, and from the tuning stub, the energy is coupled into the radiating slot through the near E -field which is defined both in the medium surrounding the antenna and in the PCB substrate.

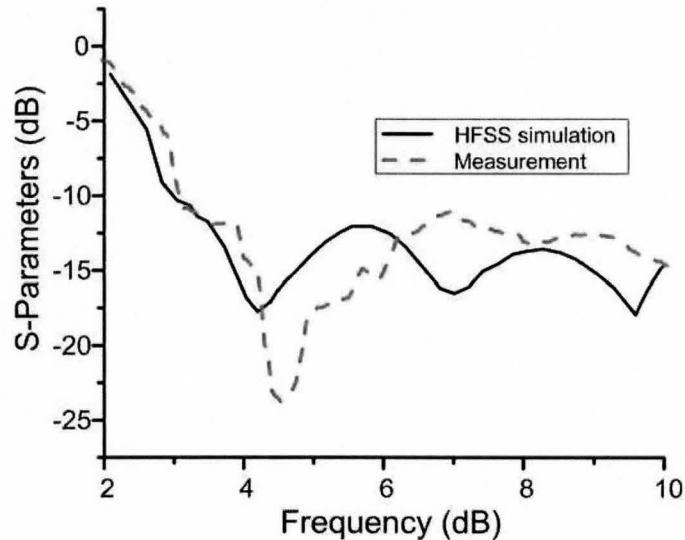


Figure 5.19. Measured and simulated return loss of the antenna in the coupling medium.

The presence of a body in proximity of the antenna affects the near E -field of the antenna, which in turn alters the level of the electromagnetic energy coupled into the radiating slot and the surface current distribution of the radiating slot. As seen from the antenna's optimization, by changing the level of the electromagnetic energy coupled into the radiating slot, the input impedance of the antenna changes over the operating frequency band. Figure 5.20 suggest that although the input impedance of the antenna is sensitive to the distance from the antenna to the skin interface, the return loss of the antenna remain below -10 dB over the UWB frequency band, if the distance from the antenna to the skin interface is greater than 5mm. Therefore, it can be concluded that the antenna should be placed as close as 10 mm to the skin interface to reduce the losses in the coupling medium.

Another way to view the changes in the reflection coefficient is that the degradation in the return loss is due to the received backscattered energy from the body

layers in proximity of the antenna. Therefore, it can be concluded that slot antenna is more sensitive to its surrounding medium. As a result, it would have better performance in detection of possible tumors in the body, compared to the TSPM antenna.

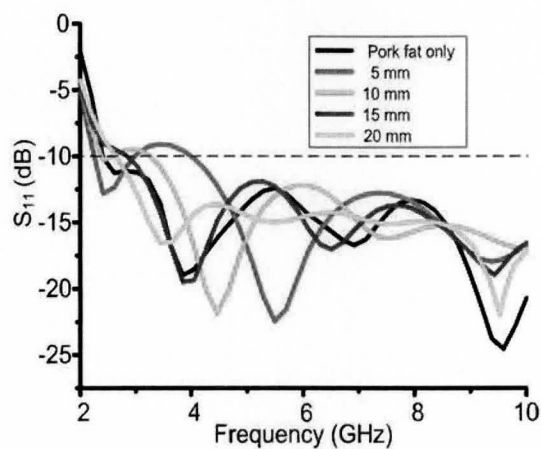


Figure 5.20. Antenna's reflection coefficient as function of distance to the skin interface.

B. Antenna Fidelity

The fidelity's simulation setup is similar to that discussed in Section 4.6. The antenna's fidelity is plotted in Figure 5.21. It is seen that the fidelity is maximum at a distance of 12 mm away from the antenna and it drops as the distance increases. The drop in the antenna's fidelity is due to the frequency-dependent attenuation and the phase delay of the transmitted signal as it propagates through the coupling medium and the body tissue. The low value of the fidelity suggests that it would be a challenging task to predict the general shape of the tumor response in a realistic tumor detection system.

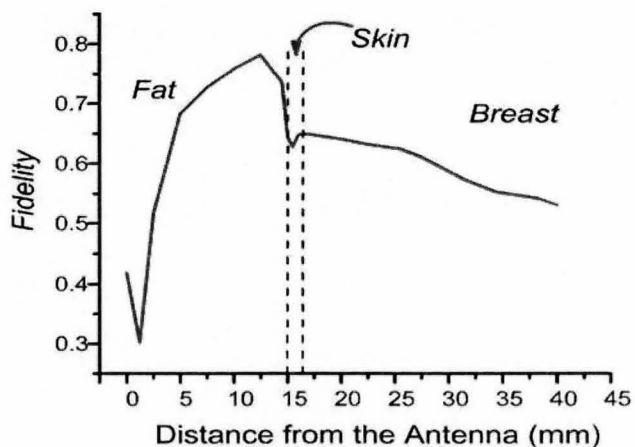


Figure 5.21. Fidelity of the slot antenna vs. distance.

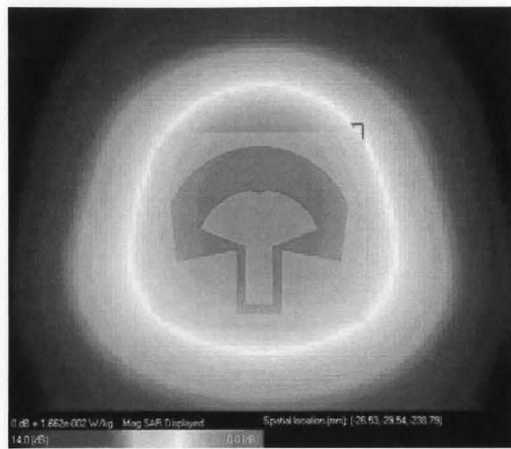
C. Antenna SAR

The SAR (specific absorption rate) was simulated with XFDTD using the body model described in Section 4.6. In the XFDTD simulation, the input power to the antenna is set to 1 mW and the 1g averaged SAR distribution is computed on the body model at the skin and breast interfaces at three frequencies of 3.5, 5.5 and 8.5 GHz. The 1g SAR distribution on the skin and breast tissue is plotted in Figure 5.22, and the maximum SAR values at 3.5, 5.5 and 8.5 GHz are given in Table 5.3. The SAR simulations demonstrates that the slot antenna meets the electromagnetic safety requirement for 1 mW input power and the maximum SAR values are well below the limit defined by the IEEE standard [43]. Also, the SAR distribution is fairly uniform around the radiating element, which implies that there is a small variation in the E -field at the skin and breast interfaces. In general, as the operating frequency increases, the maximum SAR value decreases due to the increase of electromagnetic losses in the coupling medium. However, as shown in Table 5.3, the maximum value of SAR at the skin interface at 5.5 GHz is higher than the SAR at 3.5 GHz. The increase in the SAR value might be due to the increase in the gain of the antenna at this frequency. Also, from Figure 5.22, at higher frequencies (8.5 GHz), the SAR distribution is mainly concentrated around the feed of the antenna. This is due to the fact that at higher frequencies, the electrical length of the antenna increases, resulting in high radiation from the feed of the antenna.

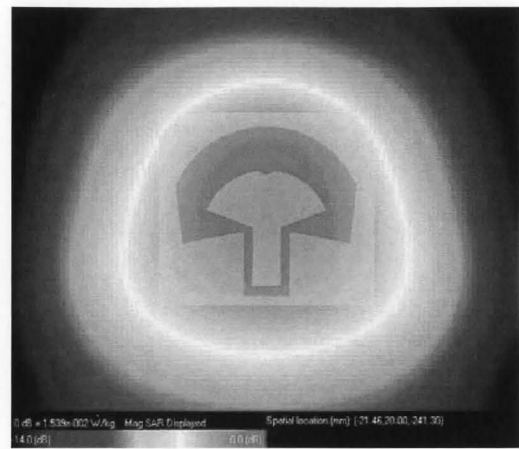
Table 5.3

CTS ANTENNA'S MAXIMUM SAR

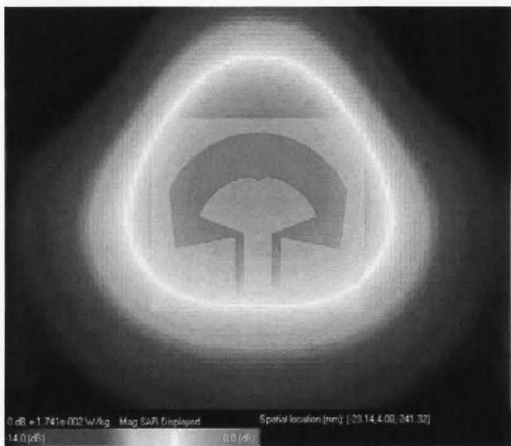
Interface	Max SAR (mW/Kg)		
	3.5GHz	5.5GHz	8.5GHz
<i>Skin</i>	16.6	17.4	12.8
<i>Breast</i>	15.3	13.8	8.6



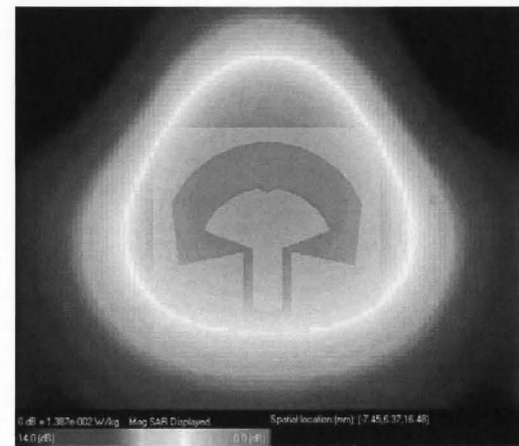
(a)



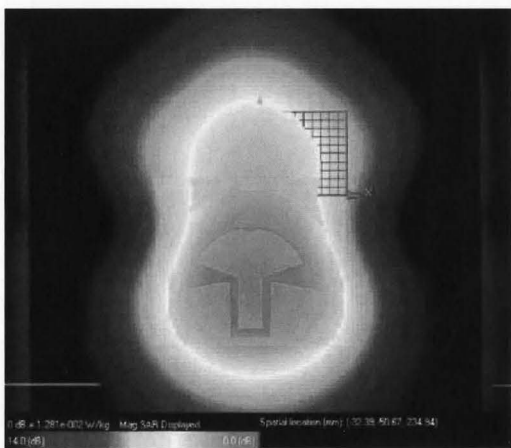
(b)



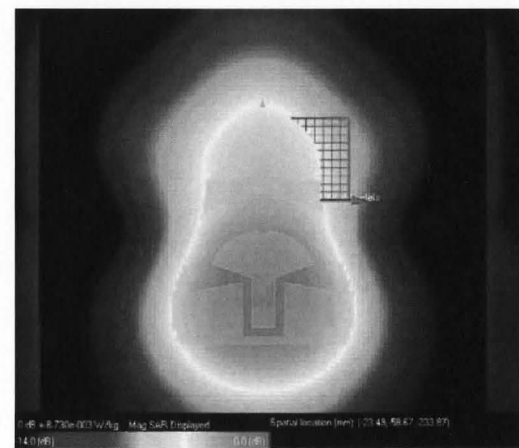
(c)



(d)



(e)



(f)

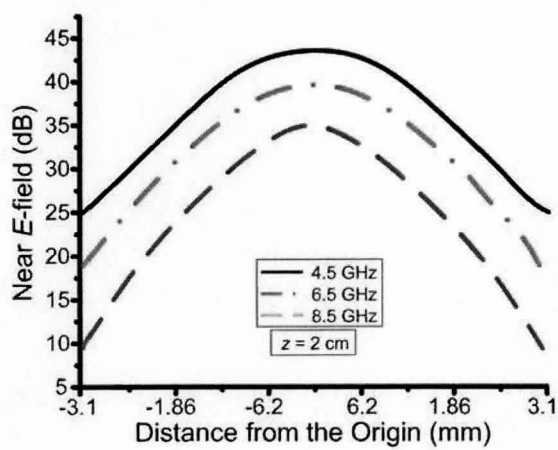
Figure 5.22 SAR distribution(a) 3.5 GHz @ skin interface, (b) 3.5 GHz @ breast interface,(c) 5.5 GHz @ skin interface, (d) 5.5 GHz @ breast interface, (e) 8.5 GHz @ skin interface, and (f) 8.5 GHz @ breast interface.

D. Near E-field

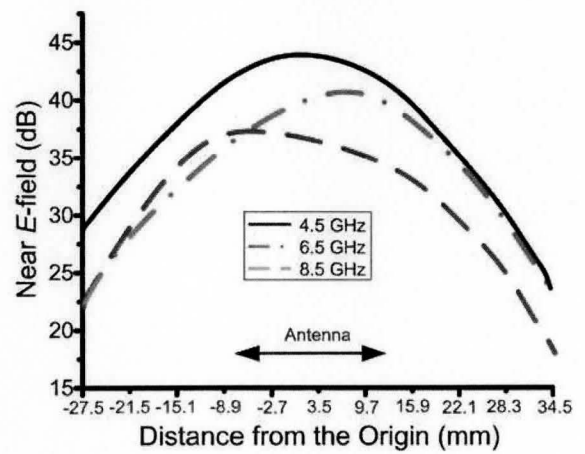
Given that the CTS antenna is used for a close range imaging application, the near E -field radiation pattern of the antenna has a major effect on the performance of the UWB imaging system. The HFSS simulator has been used to study the antenna near E -field radiation pattern in proximity of a multilayer body model at distances of $z = 2, 3$ and 4 cm from the antenna. For the radiation pattern simulation, the antenna's simulation environment is similar to the one used to study the near-field radiation pattern of the TSPM antenna, as shown in Figure 4.24.

The antenna's near E -field distributions at distances of $z = 2, 3$, and 4 cm from the antenna, inside the breast tissue, on the x -axis and at three frequencies of $4.5, 6.5$ and 8.5 GHz, are shown in Figure 5.23 (a), (b) and (c). At $z = 2$ cm, the near E -field of the antenna has a single lobe with full-width half-maximum (FWHM) beamwidth of $3.46, 3.10$ and 1.86 cm at $4.5, 6.5$ and 8.5 GHz respectively. Due to the increased losses in the coupling medium and the breast tissue, the magnitude of the near E -field decreases with increasing operating frequency. The near E -field pattern of the antenna at the $z = 3$ cm maintains the same general shape as the near E -field pattern at $z = 2$ cm with the FWHM beamwidth of $3.05, 3.0$ and 2.20 cm at operating frequencies of $4.5, 6.5$ and 8.5 GHz. At $z = 4$ cm, the near E -field of the antenna has a single lobe with a FWHM beamwidth of $2.19, 1.9$ and 1.74 cm at $4.5, 6.5$ and 8.5 GHz, respectively.

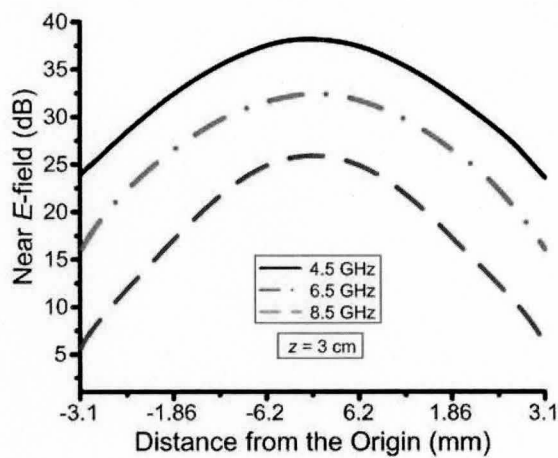
Figure 5.23 (d), (e) and (f) shows the near E -field of the antenna along the y -axis at $z = 2, 3$, and 4 cm for operating frequencies of $4.5, 6.5$ and 8.5 GHz, respectively. The near E -field of the antenna has a single lobe at $z = 2, 3$ and 4 cm, over the entire operating frequency band. At the lower frequency band, the near E -field of the antenna is mainly concentrated around the antenna's radiating element, and at the higher frequency band, the electrical length of the antenna increases and as a result, the E -field distribution is mainly concentrated around the feed of the antenna. The decrease in the magnitude of the E -field is due to the increase in the losses in the coupling medium and the biological tissues as the operating frequency increases.



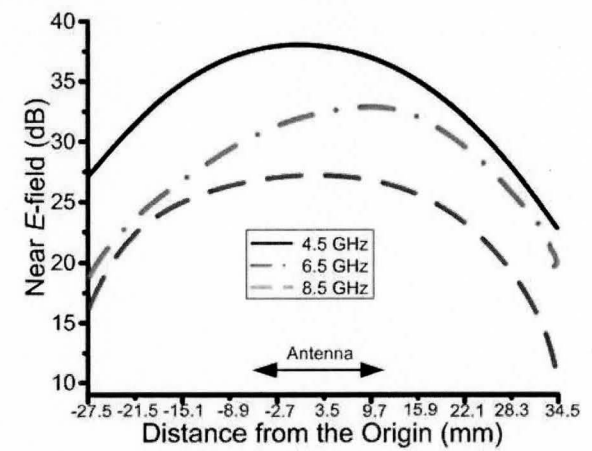
(a)



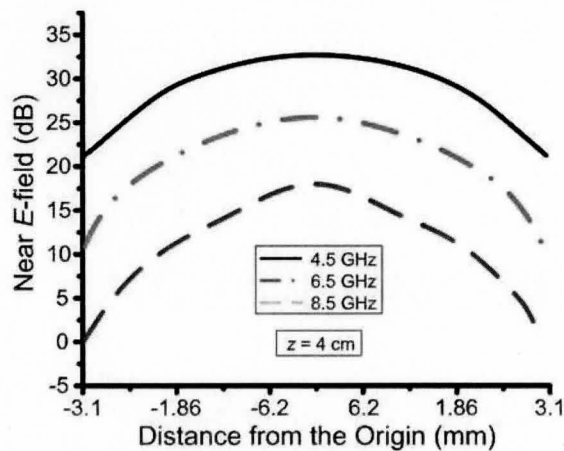
(b)



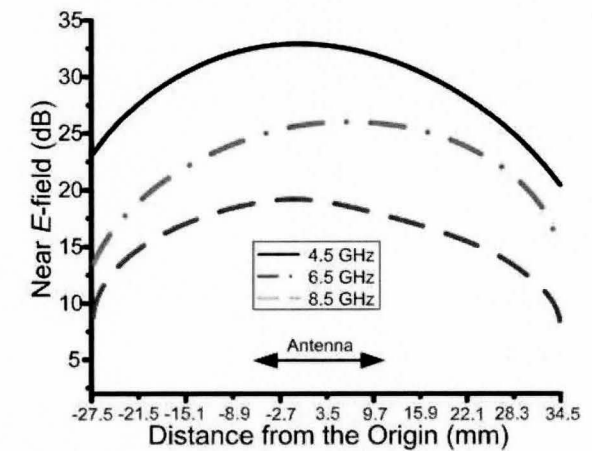
(c)



(d)



(e)



(f)

Figure 5.23 Antenna near E -field in proximity of a multilayer body model on the x -axis at (a) $z = 2$ cm, (b) $z = 3$ cm, and (c) $z = 4$ cm; and on the y -axis at (d) $z = 2$ cm, (e) $z = 3$ cm, and (f) $z = 4$ cm (refer to Figure 5.1 for the coordinate system).

5.5.1 CTS Antenna in Co-polarized and Cross-polarized Formation

A. Antenna Array Design

The configuration of the co-polarized and the cross-polarized antenna array elements are shown in Figure 5.24 and Figure 5.25. The co-polarized antenna array formation consists of two CTS antennas placed side by side in the XY-plane. The direction of the E -field and the H -field versus time is the same for both antennas in this configuration. Therefore, it can be concluded that both antennas have the same polarization, which results in a co-polarized antenna array. The distance between the two ground planes of the antennas is set to 5 mm to reduce the coupling between the two antennas, while ensuring that a sufficient level of scattered energy is received by the receiver antenna.

In the cross-polarized configuration, two CTS antennas are placed in the XY-plane and one of the antennas is perpendicular to the other. In this configuration, the direction of E -field and H -field vs. time of one antenna is perpendicular to the direction of E -field and H -field of the other antenna. Therefore, the antennas will have opposite polarization, which results in a cross-polarized antenna array. The distance between the two ground planes of the antennas is set to 3 mm to reduce coupling between the two antennas.

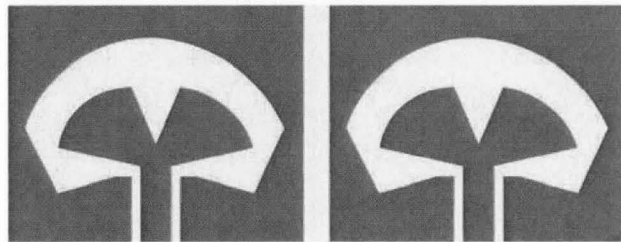


Figure 5.24. Geometry of the co-polarized CTS antenna array.



Figure 5.25. Geometry of the cross-polarized CTS antenna array.

A. Measurement Results

The S -parameters of the array elements have been measured using a HP 8720ES network analyzer and a 85305B economy calibration kit has been used to calibrate the network analyzer to the feed point of the CPW. The measured reflection coefficient of the antennas is plotted in Figure 5.26. Measurement results show a reflection coefficient (S_{11}) less than -10 dB from 3.1 to 10 GHz. The coupling between two antennas (S_{21}) for co-polarized and cross-polarized array elements is plotted in Figure 5.26. The measurement results indicate a coupling of less than -20 dB and -25 dB from 2 to 10 GHz, which means that only 0.1% and 0.05% of the input power to the transmitter antenna is being received by the receiver antenna.

The phase of the S_{12} and S_{21} parameters of antenna array elements are plotted in Figure 5.27 and Figure 5.28. As can be seen from the both figures, the phase shift over the UWB frequency range is nearly linear, which resulted in near nearly constant group delay over the UWB frequency range. The group delay between the antennas is due to the delay in the CPW, the radiation element and the path between the antennas.

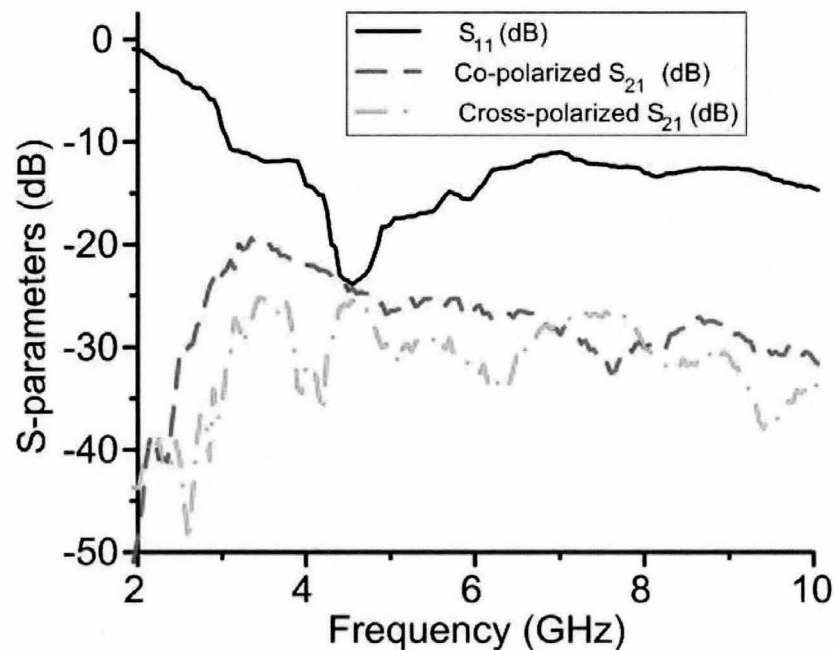


Figure 5.26. Measured antenna return loss and the coupling between the array elements in the co-polarized and cross-polarized formation.

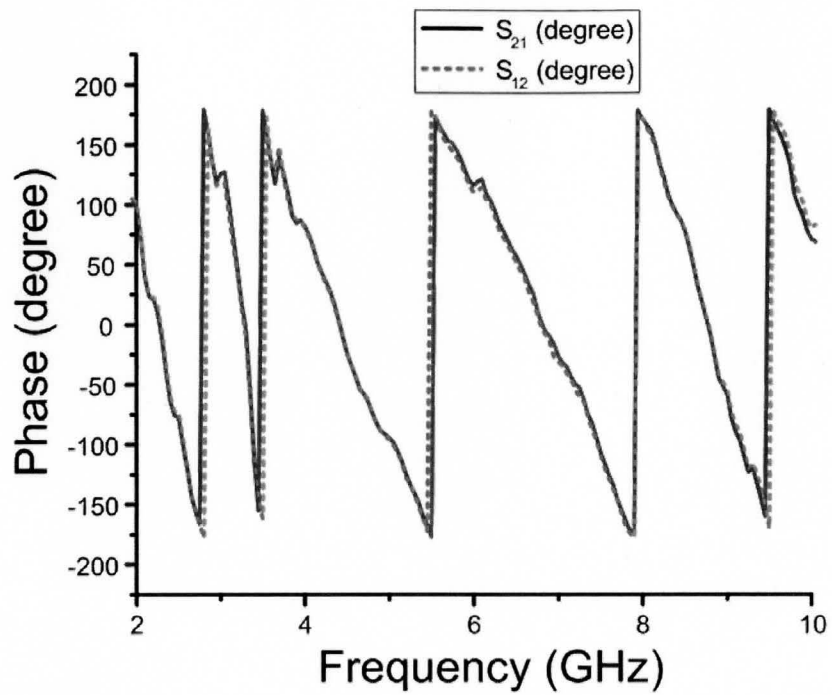


Figure 5.27. Measured phase of the co-polarized array element.

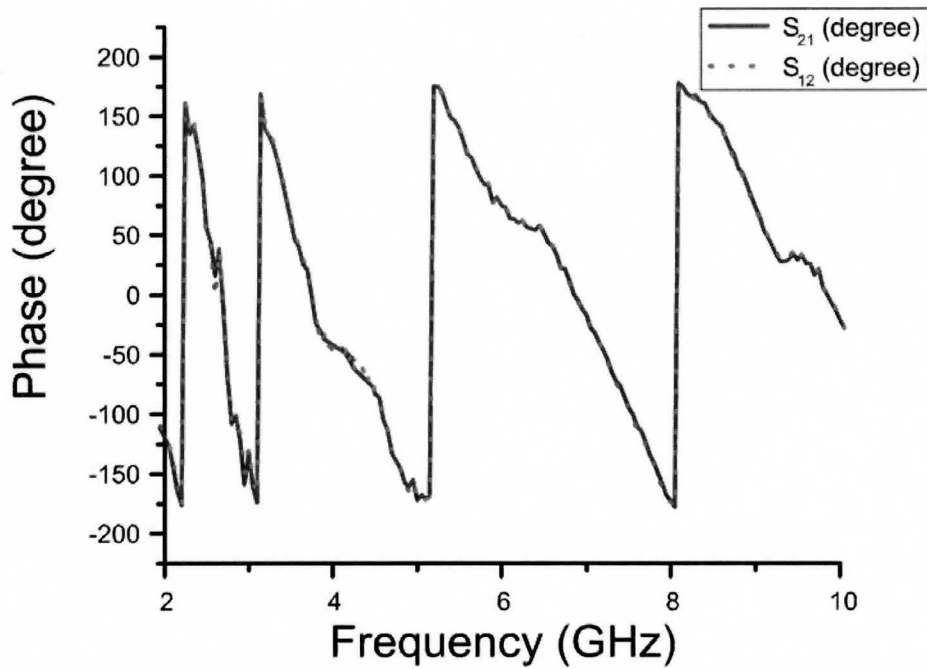


Figure 5.28. Measured phase of the cross-polarized array element.

C. Tumor Detection Capabilities (Simulation)

A set of XFDTD simulations similar to the ones performed for the TSPM antenna was conducted to investigate imaging capabilities of the co-polarized and cross-polarized antenna array for the purpose of breast cancer detection for tumors close and away from the chest wall. The XFDTD simulation results for the co-polarized and cross-polarized antenna array are plotted in Figure 5.29 and Figure 5.30. For the case of tumors away from a planar chest wall, the co-polarized and cross polarized tumor response from a $8 \text{ mm} \times 10 \text{ mm}$ tumor is 38.7 and 51.7 dB below the energy of the pulse that was used to excite the transmitter antenna. As a result, it can be concluded that a UWB imaging system employing co-polarized/cross-polarized antenna array should achieve a dynamic range in excess of 40 dB/55 dB in order to detect a tumor of this size at a depth of 3 cm. Also, as it can be seen from Figure 5.29 and Figure 5.30, the coupling between two antennas is an order of magnitude larger than the tumor response; so it should be removed from the received signal before any signal processing is done to detect the presence of the tumor. The coupling between the two array elements can be removed by subtracting it from all measured results, given that it is deterministic. The co-polarized and cross-polarized tumor and muscle responses for the case of tumors close to a planar chest wall are plotted in Figure 5.29 (e) and (f), and Figure 5.30. (e) and (f). The comparison of the scales of the plots in these Figures shows that the tumor response of the cross-polarized array is an order of magnitude smaller than that of the co-polarized array. However, the ratio of the received energy from the tumor to the received energy from the muscle layer is -6.5 dB for the co-polarized array and it is 1.2 dB for the cross-polarized array, which shows that the cross-polarized array improves the ratio of the tumor-to-clutter ratio by 7.7 dB. The tumor-to-clutter ratio is defined by the ratio of the energy of the tumor response to the energy of the muscle response. The energy of the tumor and the muscle responses is calculated by summing the squared magnitudes of the received signals, which are digitized samples of the time-domain voltage signals shown in Figure 5.29 (e) and (f), and Figure 5.30 (e) and (f).

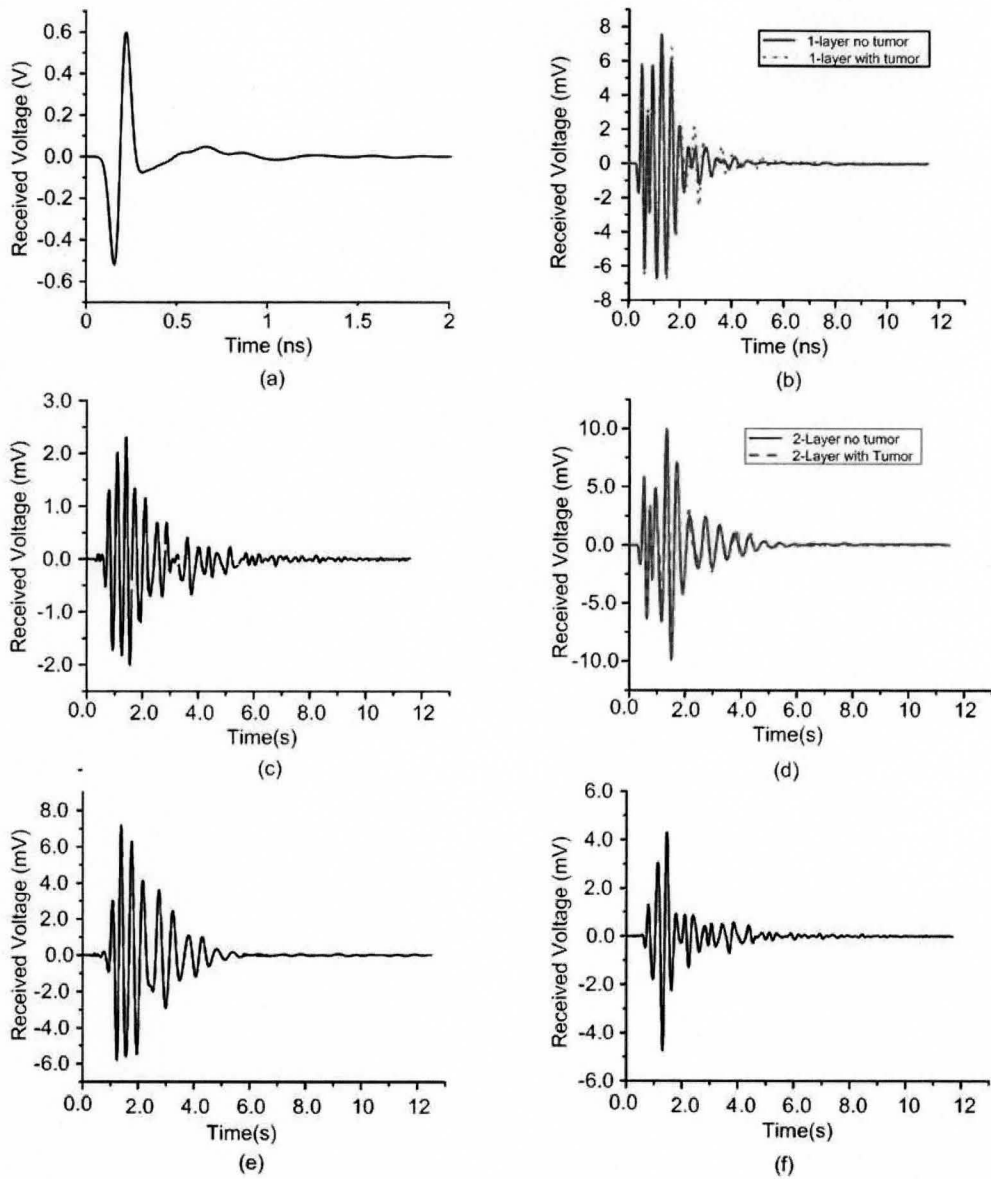


Figure 5.29. (a) Input signal to the transmitter's antenna, (b) received pulse at the receiver's antenna, for one layer simulation scenario, (c) tumor response from one layer simulation scenario, (d) received pulse at the receiver antenna, for two layer simulation scenario, (e) received signal due to the muscle layer, and (f) tumor response from one layer simulation scenario.

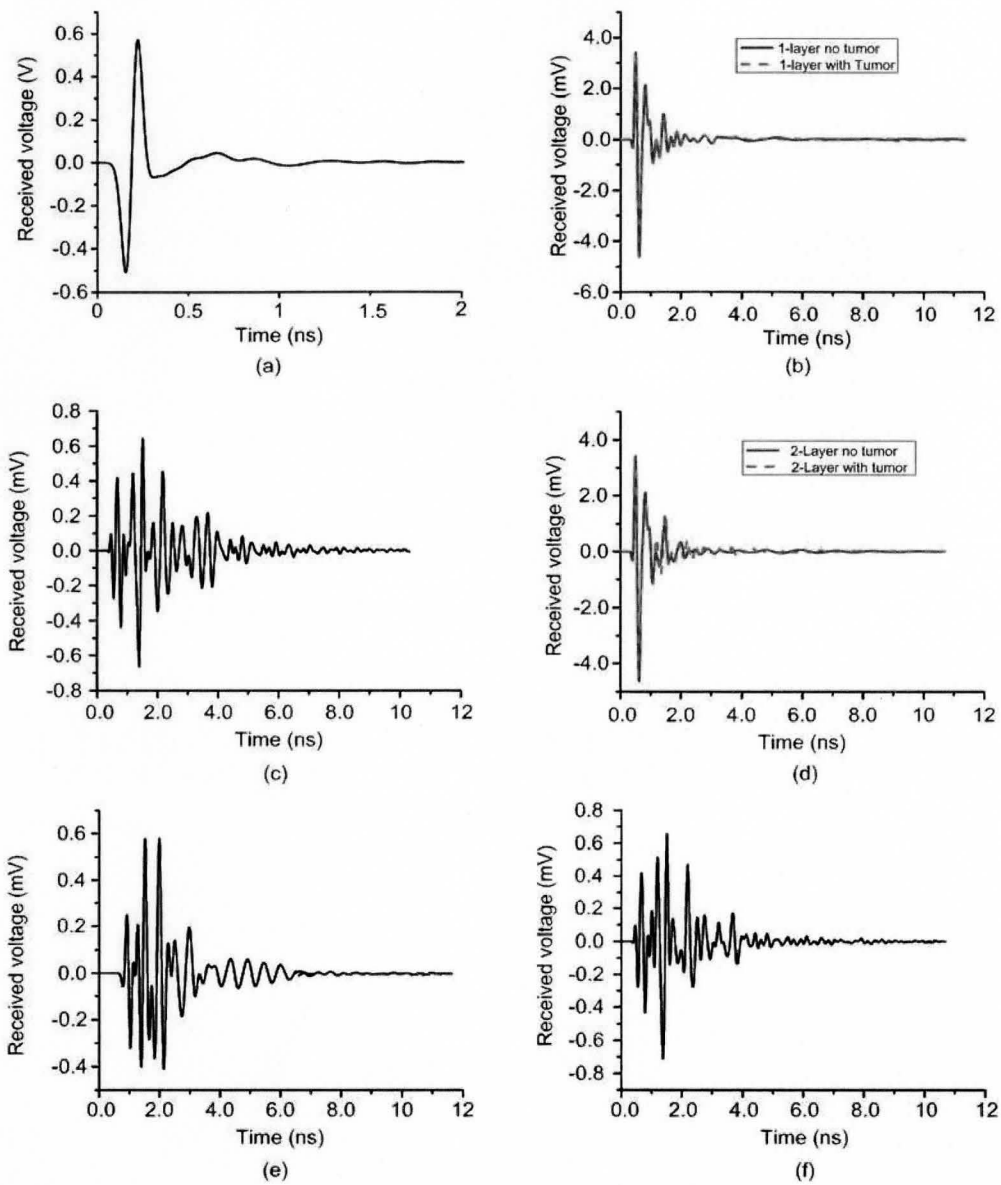


Figure 5.30. (a) Input signal to the transmitter’s antenna, (b) received pulse at the receiver’s antenna, for one layer simulation scenario, (c) tumor response from one layer simulation scenario, (d) received pulse at the receiver antenna, for two layer simulation scenario, (e) received signal due to the muscle layer, and (f) tumor response from one layer simulation scenario.

C. Tumor Detection Capabilities (Measurement)

A set of measurements was conducted to verify the simulation results and to investigate the tumor detection capability of the fabricated antenna arrays. The first set of measurement was conducted to investigate the tumor detection capabilities of the antenna

arrays in the absence of the muscle layer. The measurement setup and procedure to find the tumor response is similar to the one described for the TSPM antenna in Section 4.6.1.3 . The co-polarized and cross-polarized tumor responses for different tumor depths are plotted in Figure 5.31. The general shape of the tumor response is similar to the second derivative of a Gaussian pulse. The general shape of the tumor response is distorted as the depth of the tumor increases, which is due to the frequency-dependent attenuation and phase delay of the pulse in the coupling medium. The co-polarized and cross-polarized energy of the tumor response, normalized to the energy of the transmitted pulse for different tumor depths, is plotted in Figure 5.32. The co-polarized and cross-polarized received energy from the tumor at 0 cm is -38 and -46 dB, and the received energy drops approximately 3 dB for every centimeter increase in the depth of the tumor from the antenna.

The second set of measurements was conducted to investigate tumor detection capabilities of the antenna arrays when a planar chest wall is present. The measurement setup is similar to the first experiment, but now a $(25 \times 25 \times 8)$ cm³ layer of pork muscle is placed at a distance of 4 mm from the antenna array. The tumor was placed at a distance of 3 cm from the antenna array and the separation between the tumor and the muscle layer was 2 mm, as shown in Figure 4.32. The tumor and muscle response was acquired using the same method described in the XFDTD simulations. The co-and cross-polarized tumor response, in the presence of the muscle layer, and the muscle response, in the absence of the tumor, for the co-polarized and the cross-polarized arrays, are plotted in Figure 5.33.

The ratio of the received energy from the tumor to the received energy from the muscle layer is -12 dB for the co-polarized antenna array, and -5 dB for the cross-polarized antenna array, which shows that the cross-polarized array element improves ratio of the tumor-to-clutter response by 7.0 dB. Although the received energy from the cross-polarized array is 13 dB smaller than the co-polarized array, in a realistic cancer detection system, the muscle response is not deterministic. Therefore, it is not possible to subtract it from the received signal to find the tumor's response. As a result, it would be preferable to use the cross-polarized array element to detect a cancerous tumor close to the chest wall.

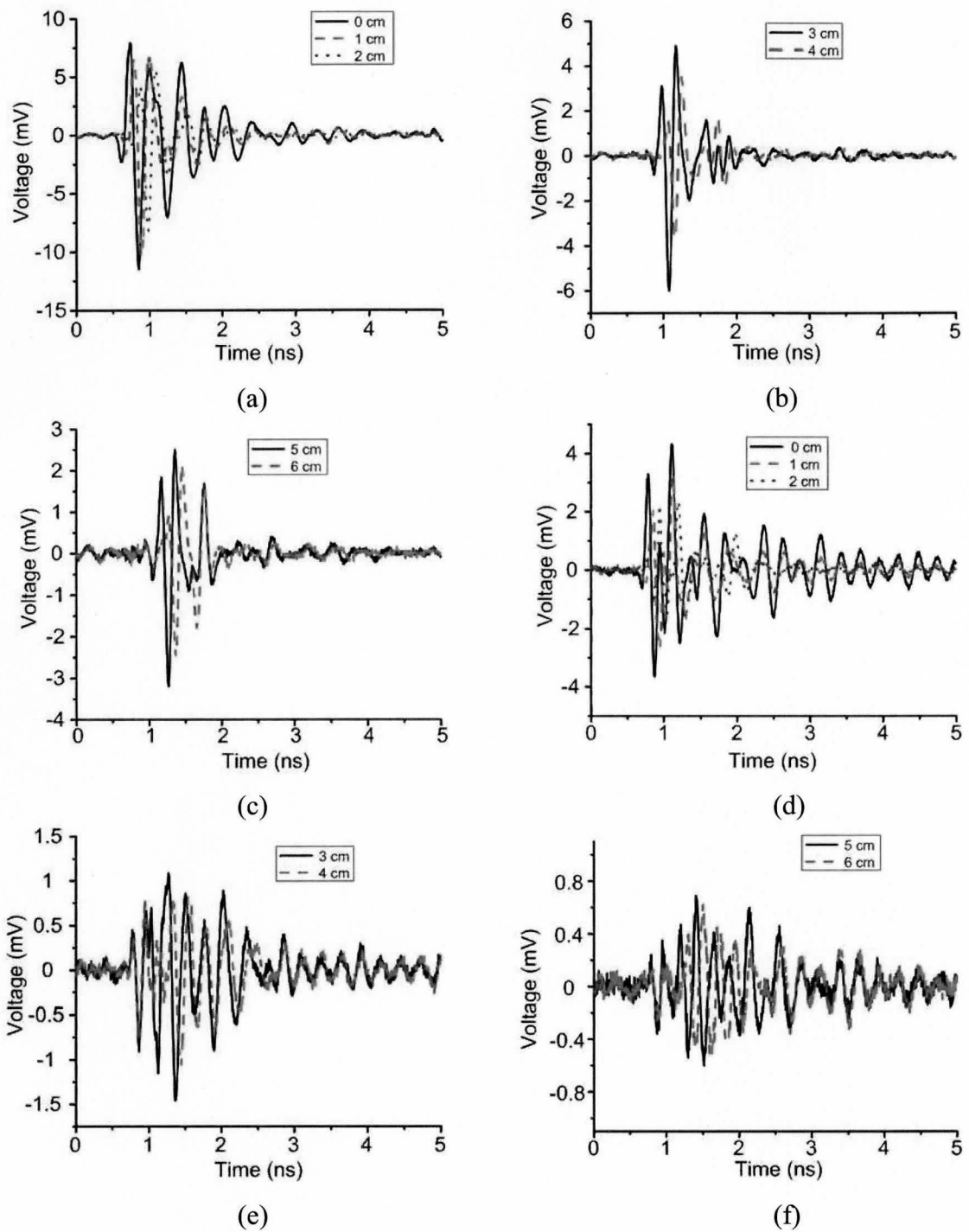


Figure 5.31. (a) Co-polarized tumor response at depth of 0, 1 and 2 cm; (b) co-polarized tumor response at depth of 3 and 4 cm; (c) co-polarized tumor response at depth of 5 and 6 cm; (d) cross-polarized tumor response at depth of 0, 1 and 2 cm; (e) cross-polarized tumor response at depth of 3 and 4 cm, and (f) cross-polarized tumor response at depth of 5 and 6 cm.

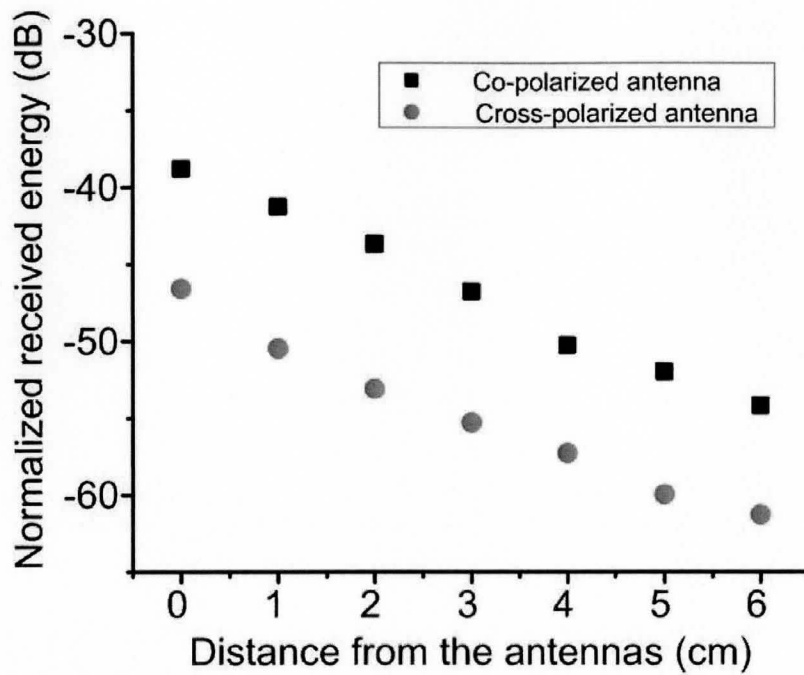


Figure 5.32. Received energy by the co-polarized and cross-polarized array elements for different tumor depth.

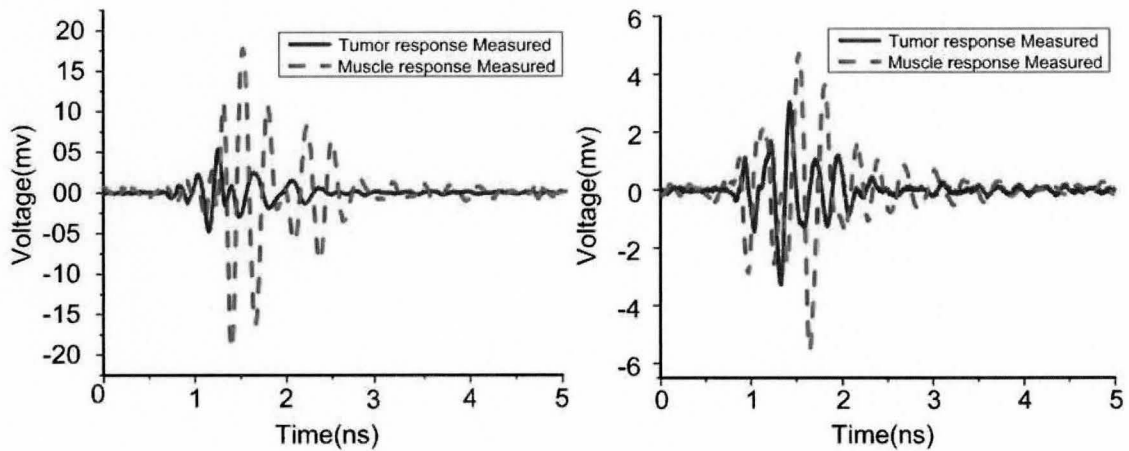


Figure 5.33. (a) Co-polarized tumor and muscle response, and (b) cross-polarized tumor and muscle response.

Comparing simulated tumour and muscle response to the measured tumour and muscle responses in Figure 5.29(e),(f) and Figure 5.30(e),(f) it is evident that there is large mismatch between the absolute levels of the received energy. This discrepancy between the simulation and measurement results is mainly due to the uncertainty in the electrical

parameters of pork fat and pork muscle and also the use of different pulses in the simulation and measurement studies, as shown in Figure 4.40 and Figure 5.29(a). On the other hand it is important to notice that the ratio of the energy of the tumour response to the muscle response correspond closely in both simulation and measurement results.

5.6 Summary

The design procedure, simulation and measurement results of CTS antenna for communication and imaging applications were studied. The CTS antennas were fabricated on commercially available PCB (FR-4), which can significantly reduce the cost of the UWB imaging and communication systems.

Antenna measurements indicate that the VSWR is below 2 from 2.4 to 5 and 6.2 to 9.3 GHz, while successfully eliminating the 5-6 GHz band. The same antenna is redesigned to operate in a lossy biological medium. The characteristics of the antenna operating in this medium and in proximity to the human body were investigated. The SAR distributions at the skin interface and the fidelity of the antenna were investigated across the UWB band. It is shown experimentally that the slot antenna, operating in a biological medium, can achieve ultra-wide bandwidth from 3.1 to 10 GHz. This enables the antenna to efficiently couple energy into the human body.

The performance characteristics of the CTS antenna in a co-polarized and a cross-polarized antenna array element in a breast cancer detection system were also investigated. The CTS antenna's measurement results indicate that the input matching of the antennas are better than -10 dB from 3.1 to 10 GHz, and the coupling between the two antennas is below -20 dB and -25 dB for the co- and cross-polarized array elements respectively. The detection capabilities of the array elements for tumors close to the chest wall and away from the chest wall were studied. It was found through measurements that for the CTS antenna array elements, that the co-polarized energy of the tumor response is in general 8 dB higher than the cross-polarized tumor response. However, the cross-polarized array element improves the tumor-to-muscle response by 7 dB. As a result, we concluded that to detect tumor that is away from the chest wall, it is preferable to employ the co-polarized array elements. But for the tumors close to the chest wall, it is preferable to use the cross-polarized array elements.

Chapter 6: CONCLUSION

In this thesis, a detailed study of UWB antennas including their design, simulation, optimization and characterization was presented. A tapered monopole antenna and a tapered slot antenna were designed for the UWB applications, and their performance characteristic was studied for the UWB imaging and communication systems.

6.1 Summary

The first antenna that was designed in this work was a tapered square printed monopole (TSPM) antenna fed with a CPW and was fabricated on a FR-4 substrate. The effect on the antenna's performance due to variations in its geometrical parameters was studied. Through HFSS optimization, it was found that contrary to the square monopole antenna on a large ground plane, reducing the width of the antenna does not improve the antenna's return loss and the highest bandwidth can be achieved by setting the width slightly larger than the length of the antenna. Measurements indicated that the TSPM can achieve an ultra-wide bandwidth from 2.2 to 8.75 GHz. The radiation pattern of the antenna was studied across the UWB band through HFSS simulation. It was found that the antenna maintains a nearly omnidirectional radiation pattern in the H -plane and a monopole-like radiation pattern in the E -plane, from 3 to 5 GHz. At the higher frequency band, from 6 to 10 GHz, the antenna's radiation pattern is distorted, and there are multiple lobes in the radiation pattern.

The TSPM antenna fed with a CPW was re-designed to operate in a coupling medium for the purpose of UWB breast cancer detection. The antenna was characterized while operating in the coupling medium and the antenna near-field pattern in a multilayer body model was studied through HFSS simulation. It was shown experimentally that a TSPM antenna can achieve ultra-wide bandwidth from 3.4 to 9.9 GHz while operating in the coupling medium, enabling the antenna to fully utilize the potential of the UWB pulses and efficiently couple energy into the human body. Also, a two element antenna array in the co- and cross-polarized formation is designed for the breast cancer detection systems. Experimental and simulation results indicated that the co-polarized antenna

array outperformed the cross-polarized antenna array in the breast cancer detection system, due to the fact that the co-polarized energy of the tumor response was in general 9 dB higher than the cross-polarized energy of the tumor response.

Next, a slot antenna fed with a CPW is designed to operate in a lossy coupling medium for the UWB imaging applications. The antenna was characterized while operating in the coupling medium and in proximity to the human body. The SAR distributions at the skin interface and the fidelity of the antenna was studied across the UWB band. The measured antenna's return loss was below -10 dB from 3.1 to 10.6 GHz, which enabled the efficient coupling of energy into the human body. The near-field radiation pattern of the antenna in proximity of a multilayer body model was studied and it was found that the antenna maintained a stable radiation pattern over the entire UWB operating band. Also, the same antenna was re-designed to operate in air. The measurements indicated that the VSWR was below 2 from 2.4 to 5, and 6.2 to 9.3 GHz, while successfully eliminating the undesired 5 to 6 GHz band.

Finally, co-polarized and cross-polarized antenna arrays, based on the tapered slot antenna, were designed for a breast cancer detection system. The antenna array elements achieved a return loss of better than -10 dB from 3.1 to 10 GHz and the coupling between the elements was below -20 dB and -25 dB, respectively, for the co- and cross-polarized arrays. The tumor detection capabilities of both antenna arrays were studied. Measurement and simulation results indicated that the co-polarized energy of the tumor response was in general 7.8 dB higher than the cross-polarized response. On the other hand, it was found that for tumors close to a planar chest wall, the cross-polarized antenna array improved the tumor-to-chest wall response by 7 dB. The improvement in the tumor to chest wall response indicated that it would be preferable to use the cross-polarized antenna array for detection of the tumors close to a planar chest wall. However, for the tumors away from the chest wall, it would be preferable to use the co-polarized antenna array. In a realistic cancer detection system, both co- and cross-polarized arrays should be included and used with appropriate signal processing to explore their unique features and improve the tumor detection capabilities of the UWB imaging system.

Table 8.1 shows a performance comparison between the CTS and TSPM antennas that are designed for the UWB cancer detection systems. The CTS antenna achieves a

higher impedance bandwidth with smaller geometrical sizes. The near-field radiation pattern of the CTS antenna in proximity of a body model as described in Section 5.5 contains a single lobe at a distance of $z = 2, 3$ and 4 cm from the antenna, but on the other hand the near-field radiation pattern of the TSPM antenna has a single lobe at $z = 2$ and 3 cm and two lobes at $z = 4$ cm. The change in the near-field radiation pattern of the TSPM antenna will cause difficulties in the image reconstruction in a practical breast cancer detection system. Comparison of the antennas fidelity shows that the CTS antenna compared to the TSPM antenna, transmits pulses that are a more accurate representation of the ideal output of the antenna. Finally the measurement results indicate that energy of the tumor response, received by a co-polarized CTS antenna array is 6 dB higher than the one received by a co-polarized TSPM antenna array. As a result, the comparison of the received energy indicates that the CTS antenna array can improve the dynamic range of the breast cancer detection system by 6 dB.

Table 6.1

COMPARISON OF ANTENNAS FOR BREAST CANCER DETECTION					
Design	Geometrical size	Bandwidth (GHz)	Radiation pattern (x-axis)	Fidelity	Tumor detection (normalized received energy)
CTS	20×22 mm	3.1-11	Single lobe @ $z = 2, 3$ and 4 cm	$65 @ 25$ mm	-47 dB (Co-pol @ 4 cm)
TSPM	30×25 mm	3.4-9.9	Single lobe @ $z = 2$ and 3 cm	$50 @ 25$ mm	-53 dB (Co-pol @ 4 cm)

The comparison of the TSPM and CTS antenna indicates that the CTS antenna outperformed the TSPM antenna in terms of size, bandwidth, radiation pattern, fidelity and tumor detection capability. Therefore, it is suggested that the CTS antenna be used in future breast cancer detection systems.

6.2 Future Work

This work is a preliminary study of breast cancer detection capabilities of the UWB pulses, and several improvements can be made. The first step in improving this

work is to include a more detailed and realistic breast model in the XFDTD and HFSS simulations. One way to accomplish this goal is to import an MRI model of the breast into the XFDTD and the HFSS software and study the tumor detection capabilities of the antennas in such a simulation environment. In the same manner, the measurement setup used to investigate the tumor detection capabilities of the antennas can be further improved by using a container with a shape similar to that of the breast and filling it with a non-homogenous material with properties close to that of the glands and the fatty breast tissues. A more realistic model with properties close to that of malignant tumors is also required, compared to the presented model of a cylinder filled with distilled water. In addition, the skin layer should be included in the next generation of the measurement setup.

In this work, two-element antenna arrays were used to study the tumor detection capabilities of the antennas. However, in a realistic cancer detection system, several array elements combined with a beam-forming technique are required to produce sufficiently high resolution images with acceptable accuracy. Therefore, the next step in the design of breast cancer detection systems would be the design of a multi-element antenna array combined with the proper circuitries, such as low-noise amplifiers, delay units and correlators, to enable accurate investigation of the tumor detection capabilities of the antennas.

As mentioned in Chapter 3, a major problem facing antenna design for UWB imaging systems is the reflection from the air-skin interface due to the large difference in the dielectric properties of the two media. This backscattered energy may be orders of magnitude larger than the reflected tumor response. In this work, a coupling medium was used to reduce the electromagnetic reflection from the skin interface. Although the coupling medium largely reduces the reflection from the skin interface, it does not eliminate it. As a result, the reflected signal from the skin interface reduces the dynamic range and the tumor detection capabilities of the UWB imaging system. To solve this problem in a realistic breast cancer detection system, it would be required to estimate the shape and the location of the skin interface, compute its approximate response and then subtract it from the measurement result to fully eliminate the reflections from the skin

interface and improve the tumor detection capabilities and the dynamic range of the UWB imaging system.

The final step in the design of the UWB imaging system is the integration of the antenna array with the electronic systems and an inverse imaging algorithm which should be used to detect and localize possible breast cancer tumors. A clinical trial of the UWB imaging system should be conducted to evaluate the overall performance of such a system against the benchmark breast cancer screening modalities such as MRI and X-ray mammography.

References

- [1] FCC First Report and Order: In the matter of Revision of Part 15 of the Commission's Rules Regarding Ultra-Wideband Transmission Systems, FCC 02-48, April 2002.
- [2] Code of Federal Regulations Section 47, Part 15 (47CFR15 or FCC Part 15).
- [3] D. Porcino and W. Hin, "Ultra-wideband radio technology: Potential and challenges ahead," *IEEE Communications Magazine*, Vol. 41, No. 7, July 2003, pp. 6674.
- [4] S. Stroh, "Ultra-wideband: Multimedia unplugged," *IEEE Spectrum*, vol. 40, pp. 23–27, Sept. 2003.
- [5] G.R. Aiello and G.D. Rogerson, "Ultra-wideband wireless systems," *IEEE Microwave Magazine*, vol. 4, no. 2, pp. 36–47, 2003.
- [6] M. M. El-Desouki, "Design of Integrated Power Amplifier Circuits for Biotelemetry Applications," Masters Thesis, McMaster University, January 2006.
- [7] "Cancer Facts and Figures 2005," American Cancer Society, Atlanta, Tech. Rep., 2005.
- [8] "Breast Cancer Facts and Figures 2003-2004," American Cancer Society, Atlanta, Tech. Rep., 2003.
- [9] D. M. Pozar, *Microwave Engineering*, 2nd ed., New York, USA: John Wiley & Sons, Inc., 1999
- [10] IEEE Standard Definitions of Terms for Antennas, IEEE Std 145, 1983
- [11] C.A. Balanis, *Antenna Theory and Analysis*, 2nd ed., Wiley, New York, 1997.
- [12] N. K. Nikolova, *Modern antenna in wireless communications*, <http://www.ece.mcmaster.ca/faculty/nikolova/antennas.htm>, September 2006.
- [13] I. Oppermann, M. Hamalainen and J. Linatti, *UWB Theory and Applications*, 1st ed., Wiley, New York, 2004
- [14] H. Kanj and M. Popovic, "Miniaturized microstrip-fed "dark eyes" antenna for pulsed microwave probing: return loss, efficiency and fidelity" *Proc. IEEE Int. Symp. Antennas Propagat.*, vol. 2B , pp. 808 - 811, 3-8 July 2005.

- [15] H. Kanj and M. Popovic, "Miniaturized Microstrip-Fed "Dark Eyes" Antenna for Near-Field Microwave Sensing", *IEEE Antennas Wireless Propagat. Lett.*, vol. to appear, pp. 1–4, Sept. 2005.
- [16] H. Kanj and M. Popovic, "Microwave-range broadband "Dark Eyes" antenna: Detailed analysis and design," *IEEE Antennas Wireless Propagat. Lett.*, vol. to appear, pp. 1–4, Sept. 2005.
- [17] S. Hagness, A. Taflove, and J. E. Bridges, "Three-dimensional FDTD analysis of a pulsed microwave confocal system for breast cancer detection: Design of an antenna-array element," *IEEE Trans. Antennas Propagat.*, vol. 47, pp. 783–791, May 1999.
- [18] X. Yun, E.C. Fear, R.H. Johnston, "Compact antenna for radar-based breast cancer detection," *IEEE Trans. Ant. Propag.*, vol. 53, pp. 2374–2380, 2005.
- [19] J. M. Sill and E. C. Fear, "Tissue sensing adaptive radar for breast cancer detection—experimental investigation of simple tumor models," *IEEE Trans. Microwave Theory Tech.*, vol. 53, no. 11, pp. 3312–3319, Nov. 2005.
- [20] C. J. Shannon, E. C. Fear, and M. Okoniewski, "Dielectric-filled slotline bowtie antenna for breast cancer detection," *IEEE Trans. Antennas Propagat.*, vol. 41, pp. 388–390, 2005.
- [21] X. Li, S. C. Hagness, M. K. Choi, and D.W. van derWeide, "Numerical and experimental investigation of an ultrawide-band ridged pyramidal horn antenna with curved launching plane for pulse radiation," *IEEE Antennas Wireless Propagat. Lett.*, vol. 2, no. 18, pp. 259–262, 2003.
- [22] G. Kumar, K.P. Ray, *Broadband Microstrip Antennas*, Artech House, Inc., Boston, 2003.
- [23] C.A. Balanis, *Antenna Theory and Analysis*, 2nd ed., Wiley, New York, 1997
- [24] J. Powell, *Antenna Design for Ultra Wideband Radio*. M. Sc. Thesis, Massachusetts Institute of Technology, MA, 7 May 2004.
- [25] E. J. Bond, X. Li, S. C. Hagness and B. D. Van Veen, Microwave imaging via space-time beamforming for early detection of breast cancer, *IEEE Trans. Antennas Propagat.*, vol. 51(8), Aug. 2003, pp. 1690 – 1705
- [26] W. Liu, H. M. Jafari, S. Hranilovic and M. J. Deen, "Time domain analysis of UWB breast cancer detection," *23rd Biennial Symposium on Communications*, Dept. of Electrical and Computer Engineering, Queen's University, May 2006, Kingston, Ontario, Canada.

- [27] J. Kim, D. Oh, J. Park, J. Cho, Y. Kwon, C. Cheon and Y. Kim, "Permittivity measurements up to 30 GHz using micromachined probe ," *J. Micromech. Microeng.* vol. 15, 2005, pp. 543–550.
- [28] K. C. Gupta et al., *Microstrip Lines and Slotlines*, Norwood MA, USA: Artech House, Inc., 2nd ed., 1996
- [29] J. C. Ranuarez, "Broadband microwave amplifiers in deep sub-micron CMOS technology," Masters Thesis, McMaster University, August 2005
- [30] Agilent Technologies, USA, ADS Momentum, www.home.agilent.com/
- [31] E. Chen and S. Y. Chen, "Characteristic of coplanar transmission line on multilayer substrates: modeling and experiments," *IEEE Trans. Microwave Theory Tech*, vol. 45(6), June 1997.
- [32] Ansoft Corporation, USA, HFSS 9.2, www.ansoft.com.
- [33] N.P. Agrawal, G. Kumar and K.P. Ray, "Wide-band planar monopole antennas," *IEEE Trans. Antennas Propagat.*, vol. 46(2), Feb. 1998, pp.294–295.
- [34] E. Hallen, 1938, Theoretical investigations into the transmitting and receiving qualities of antennae, *Nova Acta Regiae SOC. Sci. Upsaliensis*, Sec. IV, 11, No. 4, 1-44.
- [35] H. M. Jafari, M. J. Deen, S. Hranilovic, and N.K. Nikolova , "Study of Ultra-Wideband Antennas Operating in a Biological Medium," *IEEE Transaction on Antenna Propagat.*, submitted, 5 pages, December 2005.
- [36] S. Y. Suh, "A Comprehensive Investigation of New Planar Wideband Antennas," Ph.D. Thesis, Virginia Tech, July 2002.
- [37] ECCOSTOCK® HiK Cement, USA, www.eccosorb.com.
- [38] O. E. Allen, D. A. Hill, and A. R. Ondrejka, "Time-domain antenna characterizations," *IEEE Trans. Electromagn. Compat.*, vol. 35, Aug. 1993, pp. 339–345.
- [39] D. Lamensdorf and L. Susman, "Baseband-pulse-antenna techniques," *IEEE Antennas Propag. Mag.*, vol. 36, no. 1, pp. 20–30, Feb. 1994.
- [40] Remcom Corporation, USA, XFDTD, www.remcom.com.
- [41] Essex J. Bond et al., "Microwave imaging via space-time beamforming for early detection of breast cancer," *IEEE Trans. Antennas Propagat.*, vol. 51(8), Aug. 2003, pp. 1690 - 1750.

- [42] S. Gabriel, R. W. Lau, C. Gabriel, "The dielectric properties of biological tissues: III. Parametric models for the dielectric spectrum of tissues," *Phys. Med. Biol.*, vol. 41, 1996, pp. 2271–2293.
- [43] IEEE Standard for Safety Levels with Respect to Human Exposure to radio Frequency Electromagnetic Fields, 3 kHz to 300 GHz, IEEE Standard C95.1, 1999.
- [44] S. K. Davis, E. J. Bond, X. Li, S. C. Hagness, and B. D. Van Veen, "Microwave imaging via space–time beamforming for early detection of breast cancer: beamformer design in the frequency domain," *J. Electromagn. Waves Applicat.*, vol. 17, no. 2, pp. 357–381, 2003.
- [45] S. Vitebskiy, K. Sturgess, and L. Carin, "Short-pulse plane-wave scattering from buried perfectly conducting bodies of revolution," *IEEE Trans. Antennas Propagat.*, vol. 44, pp. 143–151, Feb. 1996.
- [46] H.K Yoon, H. R Kim, K. H. Chang, Y. J. Yoon and Y. H. Kim, "A Study on the UWB Antenna with Band-rejection Characteristic", *IEEE Antennas and Propagation Society Symposium*, June 2004 Page(s):1784 - 1787 Vol.2
- [47] W.S. Lee, K.J. Kim, D.J. Kim, and J.W. Yu, "Compact frequency notched wideband planar monopole antenna with a L-shape ground plane," *Microwave Opt Technol Lett.*, 46 (2005), 563–566.
- [48] Z. N. Low, J. H. Cheong, C. L. Law, "Low-cost PCB antenna for UWB applications," *IEEE Trans. Antennas Propagat.*, vol. 4, pp. 237–239, Feb. 2005.
- [49] C.-Y. Huang and W.-C. Hsia, "Planar elliptical antenna for ultra wideband communications," *Electron. Lett.*, vol. 41(6), 17 March 2005, pp. 296 – 297.
- [50] J. Liang, C.C. Chiau, X. Chen and C.G. Parini, "Study of a printed circular disc monopole antenna for UWB systems", *IEEE Trans. Antennas Propagat.*, vol. 53(11), Nov. 2005, pp. 3500 – 3504.
- [51] W.C Liu and P.C. Kao, "CPW-fed triangular monopole antenna for ultra-wideband operation," *Microwave Opt. Tech. Lett.*, vol. 47, no. 6, 20 Dec. 2005, pp. 580 – 582.
- [52] S.H. Lee, J.K. Park, and J.N. Lee, "A novel CPW-fed ultra-wideband antenna design," *Microwave Opt. Tech. Lett.*, vol. 44, no. 5, 20 Jan. 2005, pp. 393 – 396.
- [53] E. J. Bond, X. Li, S. C. Hagness and B. D. Van Veen, "Microwave imaging via space-time beamforming for early detection of breast cancer," *IEEE Trans. Antennas Propagat.*, vol. 51(8), Aug. 2003, pp. 1690 – 1705.

- [54] X. Li, S.C. Hagness, M.K. Choi and D.W. van der Weide, “Numerical and experimental investigation of an ultrawideband ridged pyramidal horn antenna with curved launching plane for pulse radiation”, *IEEE Trans. Antennas Propag.*, vol. 2(1) , Aug. 2003, pp. 259 – 262.
- [55] J. M. Sill and E. C. Fear, “Tissue sensing adaptive radar for breast cancer detection: study of immersion liquids”, *Electron. Lett.*, vol. 41(3), 3 Feb. 2005, pp. 113 – 115.
- [56] K. H. Lee, C. C. Chen, F. L. Teixeira, et al., “Modeling and investigation of a geometrically complex UWB GPR antenna using FDTD”, *IEEE Trans. Antennas Propag.*, vol.52(8): 1983-1991, 2004
- [57] J. M. Bourgeois, and G. S. Smith, “A fully three-dimensional simulation of a ground-penetrating radar: FDTD theory compared with experiment,” *IEEE Trans. Geosci. Remote Sens.*, vol.34(1): 36-44, 1996.
- [58] H. M. Jafari, W. Liu, S. Hranilovic and M. J. Deen, Ultra-Wideband (UWB) Radar Imaging System for Biomedical Applications, *Journal of Vacuum Science and Technology A (Special Issue for CSTC 2005)*, Vol A24(3), pp.752–757, (May/June 2006).
- [59] W. Liu, H.M. Jafari, S. Hranilovic and M.J. Deen, “Ultra-wideband Radar Imaging System for Biomedical Applications, *Twelfth Canadian Semiconductor Technology Conference*, Ottawa, Canada, p. 52 (16-19 August2005).
- [60] H.M. Jafari, M.J. Deen, S. Hranilovic and N. Nikolova, A Slot Antenna for Ultra-Wideband Applications, *Proc. IEEE Int. Symp. Antennas Propag.*, Albuquerque, New Mexico, USA, July 9 - 15, 2006.
- [61] J. Kim, D. Oh, J. Park, J. Cho, Y. Kwon, C. Cheon and Y. Kim, “Permittivity measurements up to 30 GHz using micromachined probe ,” *J. Micromech. Microeng.* vol. 15, 2005, pp. 543 – 550.
- [62] K. Kwon, S. Lim, S. Cho, J. Yoon, J. Cho, C. Cheon and Y. Kwon, “Planar type probe with multiple-polarization response for in-vivo permittivity measurements of heterogeneous biological tissues,” *IEEE Microwave and Wireless Components Lett.*, vol. 16(1), Jan. 2006, pp.1-3.
- [63] H. Hwang, J. Yim, J. Cho, C. Cheon and Y. Kwon, “110 GHz broadband measurement of permittivity on human epidermis using 1mm coaxial probe,” 2003 *IEEE MTT-S Digest*, pp. 399 – 402

- [64] J. Kim, D. Oh, Y. Kwon, C. Baek, J. Cho, Y. Kwon, C. Cheon and Y. Kim, “In vitro measurement using MEMS probe array with five-strip lines for permittivity measurement ,” *J. Micromech. Microeng.* vol. 16, 2006, pp. 173–179.
- [65] S. Gabriel, R. W. Lau, C. Gabriel.“ The dielectric properties of biological tissues: III. Parametric models for the dielectric spectrum of tissues” *Phys. Med. Biol.*, vol. 41, 1996, pp. 2271–2293.
- [66] I. Pele, A. Chousseaud, S. Toutain, “Multi-band ultra wide band antennas” *2005 European Microwave Conference*”, vol.3, 2005, pp.4-7.
- [67] P. Li, J. Liang and X. Chen, “Study of Printed Elliptical/Circular Slot Antennas for Ultra-wideband Applications”, *IEEE Trans. Antennas Propag.*, vol. 54, no. 6, June 2006, pp.1670-1675.